Hydrothermal Transport in the Panama Basin and in Brothers Volcano using Heat Flow, Scientific Deep Sea Drilling and Mathematical Models

Kannikha Parameswari Kolandaivelu

Dissertation submitted to the Faculty of the Virginia Polytechnic Institute and State University in partial fulfillment of the requirements for the degree of

Doctor of Philosophy
In
Geosciences

Dr. Robert P. Lowell, Chair
Dr. John A. Hole
Dr. Scott D. King
Dr. Ryan M. Pollyea

November 16, 2018
Blacksburg, Virginia

Keywords: hydrothermal systems, hydrothermal circulation, mid-ocean ridges, submarine arc volcano, heat flow, permeability, mass flux, fracture zones, panama basin, costa rica rift, Ecuador fracture zone, brothers volcano

Hydrothermal Transport in the Panama Basin and in Brothers Volcano using Heat Flow, Scientific Deep Sea Drilling and Mathematical Models

Kannikha Parameswari Kolandaivelu

ABSTRACT

Two-thirds of submarine volcanism in the Earth's ocean basins is manifested along mid-ocean ridges and the remaining one-third is revealed along intraoceanic arcs and seamounts. Hydrothermal systems and the circulation patterns associated with these volcanic settings remove heat from the solid Earth into the deep ocean. Hydrothermal circulation continues to remove and redistribute heat in the crust as it ages. The heat and mass fluxes added to the deep ocean influence mixing in the abyssal ocean thereby affecting global thermohaline circulation. In addition to removing heat, hydrothermal processes extract chemical components from the oceanic and carry it to the surface of the ocean floor, while also removing certain elements from seawater. The resulting geochemical cycling has ramifications on the localized mineral deposits and also the biota that utilize these chemical fluxes as nutrients. In this dissertation, I analyze observed conductive heat flow measurements in the Panama Basin and borehole thermal measurements in Brothers Volcano and use mathematical models to estimate advective heat and mass fluxes, and crustal permeability. In the first manuscript, I use a well-mixed aquifer model to explain the heat transport in a sediment pond in the inactive part of the Ecuador Fracture Zone. This model yields mass fluxes and permeabilities similar to estimates at young upper oceanic crust suggesting vigorous convection beneath the sediment layer. In the second manuscript, I analyze the conductive heat flow measurements made in oceanic between 1.5 and 5.7 Ma on the southern flank of the Costa Rica Rift. These data show a mean conductive heat deficit of 70%, and this deficit is explained by various hydrothermal advective transport mechanisms, including outcrop to outcrop circulation, transport through faults, and redistribution of heat by flow of hydrothermal fluids in the basement. In the third manuscript, I analyze the borehole temperature logs for two sites representative of recharge and discharge areas of hydrothermal systems in the Brothers Volcano. I develop upflow and downflow models for fluids in the borehole and formation resulting in estimated of flow rates and permeabilities. All three independent research works are connected by the common thread of utilizing relatively simple mathematical concepts to get new insights into hydrothermal processes in oceanic crust.

GENERAL AUDIENCE ABSTRACT

Two-thirds of underwater volcanic activity in the Earth's ocean basins is exhibited in areas where new material for Earth's outer shell is created and the remaining one-third is displayed along areas where the outer shell is destroyed. In these areas, hot springs that are under water and their water movement patterns remove heat from the solid outer shell and puts it into the deepest parts of the ocean. Hot water circulation continues to remove and redistribute heat and various chemical elements in the shell as it grows old. This heat and chemical elements, which get added to the deep ocean water, influences the way water mixes and forms layers in the world oceans. This also affects the movement of ocean currents. The chemical elements removed from the shell by hot water gets deposited as minerals on the ocean floor in places where hot springs arise. This variety of minerals provides nutrients for different marine organisms. In this work done during my PhD studies, I examine the heat and temperature that was measured in the Panama Basin and Brothers Volcano. I utilize these examinations to build simple math models to find out how much heat and chemical components are being added to the deep ocean water. I also find out the methods in which the hot water springs appear on the ocean floor and the patterns in which the hot water circulates in the Earth's outer shell. All of these estimates will help the scientists who are studying the patterns and changes in ocean currents by giving them a number on how much heat is released from the inside of the Earth.

Acknowledgements

My PhD journey is filled with contributions from people of all different aspects of my life. First I would like to extend my sincere gratitude for the constant support, guidance and mentorship of Dr. Robert Lowell, my advisor, throughout my graduate school journey. His knowledge and expertise has immensely assisted in my growth as an early-career researcher and strengthened my research skills. I would like to thank Dr. Ryan Pollyea for consistently extending his strength, guidance and counsel during the tough times of graduate school and for sharing his knowledge and support on the Enhanced Geothermal Systems independent study.

A special thanks is in order for my distinguished committee members, Dr. John Hole, Dr. Scott King and Dr. Ryan Pollyea for their immaculate advise, scientific views, suggestions to enhance my research and for pushing my limits. I thank the Department of Geosciences and Virginia Tech for providing me with a variety of opportunities to explore and expand my scientific horizons. A huge thanks to Dr. Robert Harris who has immensely contributed to two-thirds of this dissertation with his heat flow expertise and providing the heat flow data analyzed in this thesis.

I thank the entire OSCAR team from all around the world for being a part of my "circle of influence" and for assisting in enhancing my multi-disciplinary thinking. I am also thankful for the scientific party, technicians and crew of IODP's Expedition 376 aboard the RV JOIDES Resolution for providing me with the best 60-day scientific experience and for exponentially helping me grow as a scientist.

I am very grateful for the undying love and support of my parents, Dr. V.M. Kolandaivelu and Dr. K. N. Thulasiammal, for showing me how important it is to keep exploring your inner curiosities. I thank my extended family back in India for looking after me. A lot of fellow graduate students and friends of mine form the framework of this journey and have extended their love, friendship and support. A huge thank you to: Didem Beskardes, Shadi Esmaily, Vanessa Frost, Roberto Marivela, Pavithra Sekhar, Eszter Sendula, Quimin Wu, Amir Zainali and other friends from VT. Virtual support does count too: Thank you dear friends, old and new, from all around the world, especially Australia, Brazil, Germany, India, Japan, New Zealand and UK for having my back.

This work was supported by NSF Grants OCE 1353114 and 1558797 to Dr. Robert P. Lowell and Grants NSF OCE 1353003 and 1558824 to Dr. Robert N. Harris. This work was also supported by the generosity of the Department of Geosciences with the following awards: Petroleum Industry Research Scholarship (2017) and David R. Wones Research Scholarship (2015). The third project stemmed from the US Science Support Program's 3-month salary support to sail as a Petrophysics/Geothermal Borehole Logging Specialist in the IODP's Expedition 376 to the Brothers Volcano.

Contents

List of Figures

List of Tables

Chapter 1

Introduction

Hydrothermal circulation in the oceanic crust occurs near areas of vigorous volcanic and magmatic activity and continues to occur as the crust ages. Hydrothermal circulation serves as a means to remove heat from the deep Earth and deposit it in the ocean. At active mid-ocean ridges (MOR) and volcanism along intraoceanic arcs, hydrothermal circulation manifests as mostly high temperature vents and away from the ridges and active volcanoes at arcs, hydrothermal circulation occurs as low temperature diffuse flow through faults, sediments, outcrops etc.. The surficial manifestation of heat flow due to hydrothermal circulation can be measured by using conductive heat flow probes in sediments in oceanic crust off-axis to MOR. Alternatively, hydrothermal circulation patterns can also be interpreted from thermal measurements in drilled boreholes. In this dissertation, I utilize both heat flow and and borehole temperature data, coupled with mathematical modeling, to investigate hydrothermal processes in the Panama Basin and Brothers Volcano.

The first manuscript titled "Analysis of a Conductive Heat Flow Profile in the Ecuador Fracture Zone" was published in *Earth and Planetary Science Letters* in 2017. Eighteen conductive heat flow measurements were made in a sediment pond of the inactive part of the Ecuador Fracture Zone in the Panama Basin. The heat flow increases linearly from west to east in the pond indicating a lateral advective heat transfer between exposed outcrops on the western and eastern margins of the sediment pond. A well-mixed aquifer model was employed to explain this eastwardly flow, and it yielded estimates of volumetric flow rates and basement permeabilities. These permeabilities are similar to other estimates in young oceanic upper crust and suggest that vigorous convection within the basement significantly modifies the thermal regime of fracture zones.

The second manuscript titled "Evolution of Heat Flow, Hydrothermal Circulation and Permeability on the Young Southern Flank of the Costa Rica Rift" was submitted to Geophysical Journal International in September, 2018 and is currently under revision based on reviewer comments. Sixty-seven new conductive heat flow measurements were made at five sites ranging in age between approximately 1.6 and 5.7 Ma from the southern flank of the Costa Rica Rift (CRR). The mean observed conductive heat flow show a 70% deficit indicating that hydrothermal processes account for about 70% of the heat loss. The advective heat loss fraction varies from site to site and is driven by a combination of highly vigorous convection in upper oceanic crust, outcrop to outcrop circulation, discharge through faults, and flow through thinly-sedimented basement highs. Advective heat loss becomes negligible at 5.7 Ma, though hydrothermal circulation in the basement acts to redistribute conductive heat flow through the

sediments. Various models such as 1-D conduction model, well-mixed aquifer models, model of heat flow through a fault and vertical flow of hydrothermal fluids in the basement were utilized to assess the flow rates, mass fluxes and permeabilities in the upper basement. The results indicate that crustal permeability does not decline monotonically as a function of lithospheric age. Sediment cover that approaches 200 m thick and buries the basement topography appears to be the main factor in inhibiting advective heat and mass transfer to the ocean. There are only two other heat flow measurement studies at young ridge flanks of < 10 Ma and their analysis portrays that sediment blanketing due to the local rapid sedimentation rates leads to cessation of advective heat transfer into the ocean. Hence the new dataset in this manuscript will serve as a substantial addition to the sparse heat flow observations present at young mid-ocean ridge flanks.

The third manuscript titled "Analysis of Thermal Profiles of Two Boreholes Drilled into Brothers Volcano During IODP Expedition 376" is under preparation for submission. This work assesses the borehole temperature data from two different boreholes that were drilled during the International Ocean Discovery Program's Expedition 376 to the Brothers Volcano. Downhole temperature logs from the two boreholes exhibit both recharge and discharge regimes of a hydrothermal system. Models for vertical flow through a borehole and upflow through formation assist in estimating the flow rates in the borehole and/or formation and result in permeability estimates of the formation.

Chapter 2

Analysis of a Conductive Heat Flow Profile in the Ecuador Fracture Zone

Kolandaivelu, K. P., Harris, R. N., Lowell, R. P., Alhamad, A., Gregory, E. P., & Hobbs, R. W. (2017). Analysis of a conductive heat flow profile in the Ecuador Fracture Zone. *Earth and Planetary Science Letters*, *467*, 120-127.

Abstract

We report 18 new conductive heat flow measurements collected from a sediment pond located in the inactive part of the Ecuador Fracture Zone in the Panama Basin. The data were collected along an east – west transect coincident with a multi-channel seismic reflection profile that extends from ODP Hole 504B to west of the sediment pond. Conductive models indicate that heat flow should decrease from ≈ 400 mWm^{-2} on the 1.5 Ma western plate to ≈ 200 mWm^{-2} on the 6 Ma eastern plate; however the observed heat flow increases nearly linearly toward the east from approximately 140 mWm^{-2} to 190 mWm^{-2}. The mean value of 160 mWm^{-2} represents an average heat flow deficit of ≈ 50%, which we attribute to lateral advective heat transfer between exposed outcrops on the western and eastern margins of the sediment pond. We apply the well-mixed aquifer model to explain this eastwardly flow, and estimate a volumetric flow rate per unit length in the north-south direction of ≈ 400 ± 250 $m^2\ yr^{-1}$ through the basement aquifer. Using a Darcy flow model with the mean flow rate, we estimate permeabilities of ~ 10^{-11} and 10^{-12} m^2 for aquifer thicknesses of 100 and 1000 m, respectively. The estimated

permeabilities are similar to other estimates in young oceanic upper crust and suggest that vigorous convection within the basement significantly modifies the thermal regime of fracture zones. Additional heat flow data are needed to determine the prevalence and importance of advective heat transfer in fracture zones on a global scale.

2.1. Introduction

Thermal and mechanical processes affect the tectonic evolution of active oceanic transforms and their fracture zone extensions [e.g., *Sandwell*, 1984; *Pockalny et al*., 1996]. In addition, these processes influence earthquake mechanics and rheology [e.g., *Behn et al*., 2007; *Roland et al*., 2010]; and, when combined with fluid circulation, they control the alteration of oceanic crust and serpentinization of the upper mantle [e.g., *Dziak et al*., 2000] in these regions. In the inactive fracture zone region beyond the active transform, half-space cooling models provide some constraints on the thermal regime of the adjacent plates and the differences in plate age across the fracture zone provide first-order controls on topography [e.g. *Menard and Atwater*, 1969]. The thermal and mechanical behavior of fracture zones is complicated, however, by lateral thermal conduction from the younger to the older plate [e.g., *Louden and Forsyth*, 1976] and by the development of an elastic layer that result in gravitational and topographical features not readily accounted for by simple models [e.g., *Sandwell and Schubert*, 1982; *Sandwell*, 1984; *Pockalny et al*., 1996].

Within and near transform faults and fracture zones heat flow data are sparse; and detailed knowledge of the thermal, mechanical, and possible hydrological regimes is limited. To our knowledge the only other heat flow data from within a fracture zone come from 23 measurements within the thickly sediment Vema transform and fracture zone [*Langseth and Hobart*, 1976]. After correcting for the effects of sedimentation, they find heat flow to be uniform and higher than expected. Other data come from the Ascension fracture zone but are mostly along the flanks of ridge segments [*Vacquier and Von Herzen*, 1964; *Langseth et al*., 1966; *Von Herzen and Simmons*, 1972].

Early thermal models of fracture zones assumed conductive heat transfer. *Louden and Forsyth* [1976] constructed two-dimensional time dependent models of thermal conduction across an idealized fracture zone and used the resulting temperature structure to calculate free-air gravity anomalies. *Behn et al.* [2007] constructed three-dimensional models of the thermal structure beneath transforms. These models used a rheology that incorporated brittle weakening of the lithosphere, resulting in elevated temperatures along the transform, and produced better agreement with observed seismicity. *Roland et al.* [2010] expanded these models to include shear heating and hydrothermal circulation and inferred that hydrothermal cooling has significant effect on the thermal structure of transform faults.

The thermal models of *Behn et al.* [2007] and *Roland et al.* [2010] focused on the large scale thermal regime at transform-ridge intersections. The thermal model of *Louden and Forsyth* [1976], which is more applicable to fracture zones, has not been tested by heat flow data. Relative to heat flow data obtained as a function of age along the flanks of mid-ocean ridges, there has been little attention paid to the details of heat flow and the thermal regime locally around transforms and their fracture zone extensions. Hence, there is essentially no information on heat flow patterns, fluid flow rates, extent of circulation, and subsurface fluid temperatures on a local scale in fracture zone settings.

In this paper, we report 18 conductive heat flow measurements collected across a sediment pond in the Ecuador Fracture Zone south of the Ecuador Rift during the cruises JC113 and JC114 of the OSCAR experiment in the Panama Basin. The data were collected along an east-west transect at a latitude of ~1° 14.0280' N coincident with a multichannel seismic line. We analyze the data using the well-mixed aquifer model.

2.2. Geologic Setting

The Ecuador Fracture Zone (EFZ) consists of the active ridge-transform-ridge offset, that joins the Costa Rica Rift (CRR) in the center of the Panama Basin, the Ecuador Rift (ER) to the south-west of the CRR, and the inactive fracture zones extending to the north of the CRR and south of ER (Figure 2.1). Swath bathymetry (Figure 2.2) collected during the cruises shows the active and inactive parts of the fracture zone; the region of the heat flow survey, which is located in the inactive part of the EFZ, is depicted by the blue rectangular box. The bathymetry indicates that the EFZ is approximately 20 km wide and is characterized by two linear highs extending for several kilometers along strike. The two linear highs form ridges that may have resulted from diaperic uplift of serpentinized-peridotite caused by the intrusion of seawater into the upper mantle via the faults [*Kastens et al.,* 1986; *Dziak et al.,* 2000]. In such fracture zones, complex processes shape the hydrogeologic and thermal regime. The sediment pond, where the heat flow measurements were conducted, extends for about 9.3 km in the east-west direction with its center at ~1° 14.0280' N, 84° 35.6460' W. The crustal ages to the east and west of the sediment pond are ≈ 6 and ≈ 1.5 Ma, respectively, based on spreading rate estimates for the Costa Rica Ridge [*Hey et al.,* 1977; *Tuckwell et al.,* 1996] and distance from ridge axis. Co-locating the heat flow data with seismic reflection data allows us to analyze the heat flow data in the context of sediment thickness and underlying basement structure.

2.3. Results

2.3.1 Seismic Reflection Measurements

A high-resolution seismic profile imaging the sediment structure and top of oceanic crust was acquired using a high-frequency (20-200 Hz) GI airgun source recorded on a 4500 m long hydrophone array with 360 groups spaced at 12.5 m. After merging with the field geometry, the seismic data were high-pass filtered to suppress low-frequency surface wave and ship-tow noise. Figures 2.3 and 2.4a were migrated to give a well-resolved image of the internal structure of the sediments and the sediment-basement interface. The sediment thickness generally increases from west to east across the sediment pond with a mean thickness of approximately 260 m (Figure 2.4a). This image also shows distinct episodes of sediment flux into the basin which may relate to the geological history of the basin as it progressed from the active to passive transform fault system.

2.3.2 Heat Flow Data

The conductive heat flow measurements were collected along a 6 km profile in the sediment pond using a multi-penetration heat flow probe (MPHF) consisting of a 3.5 m thermistor string containing 11 thermistors. The violin bow configuration allows repeated measurements during a single transit through the water making it an efficient tool. An ultra-short baseline (USBL) sensor is attached 50 m above the probe to yield precise navigation. Each measurement

consisted of both a 7 minute measurement period allowing the calculation of sediment equilibrium temperatures and a second 7 minute period following a calibrated heat pulse, generated with a heating wire along the thermistor string, so that thermal conductivity could be estimated.

Heat flow was calculated based on the processing algorithm of *Villinger and Davis* [1987] that allows iterative determination of both the local thermal gradient and values of sediment thermal conductivity [e.g., *Stein and Fisher*, 2001]. Thermal gradients, thermal conductivities and heat flow determinations are displayed in Table 2.1. Uncertainties are small and based on a Monte Carlo analysis as described in *Stein and Fisher* [2001]. Observed values of heat flow, q_{obs}, increase from approximately 140 to 190 mW m^{-2} toward the east, with a mean value of 160 mW m^{-2} (Figure 2.4b). Using the measured thermal conductivity of the sediments and assuming a linear thermal gradient, the temperatures at the sediment-basement interface are calculated from the heat flow observations. These data are also plotted in Figure 2.4b.

2.4. Analysis

For crustal ages less than about 70 Ma, basal heat flow can be predicted using a half space cooling model [*Stein and Stein*, 1994],

$$q_b = 510t^{-1/2}, \tag{2.1}$$

where the age t is in Ma and q_b is the basal heat flow expressed in mWm^{-2}. Table 2.2 lists the symbols used along with their units and values as appropriate. This model predicts basal heat flow for 1.5 and 6 Ma crust to be ≈ 400 and ≈ 200 mWm^{-2}, respectively. One could apply the conductive model of *Louden and Forsyth* [1976] to obtain an estimate of the effect of lateral conductive transfer across the fracture zone, but because of the complex tectonics within the transform and fracture zone, we calculate the expected heat flow and its uncertainty based on the mean value determined for the young and old plates from equation (2.1). This calculation gives a mean basal heat flow of ≈ 300 ± 100 mWm^{-2}. In contrast, the data yield a mean heat flow through sediment pond of 160 mWm^{-2} (Table 2.1). These values correspond to a mean fractional heat flow deficit ($1 - q_{obs}/q_b$) of ≈ 0.5. Moreover, the trend of heat flow values (Figure 2.4) is opposite to that expected from lateral conductive heat transfer from the younger to the older plate [*Louden and Forsyth*, 1976].

The heat flow deficit and trend of observed values could result from rapid sedimentation and/or from lateral advective heat loss due to fluid flow. Rapid sedimentation tends to lower the observed heat flow [e.g., *Louden* and *Forsyth*, 1976; *Hutchinson*, 1985; *Hutnak and Fisher*, 2007]. Sediment is usually assumed to be deposited at bottom water temperature and rapid sedimentation can transiently depress heat flow until the sediment warms to equilibrium values [*Hutchinson*, 1985]. The potential effect of sedimentation on heat flow can be assessed using scale analysis. If the sediment load in the pond were emplaced instantaneously, the time scale τ for conduction through the sediment pile is,

$$t_{?} \sim \frac{l^2}{a}, \tag{2.2}$$

where l is the sediment thickness, and a is the thermal diffusivity of the sediment-water composite medium given by,

$$a = \frac{K_s}{\rho c_p} \quad . \tag{2.3}$$

Here K_s, thermal conductivity of the sediments, has a nearly constant value of 0.7 $Wm^{-1}K^{-1}$ (based on measurements in Table 2.1); and ρc_p is the heat capacity of sediment-water composite medium. That is

$$\rho c_p = \rho_s c_s (1 - \phi) + \rho_f c_f \phi, \tag{2.4}$$

where ρ_s and ρ_f are the densities of sediment and water respectively, c_s and c_f are the specific heat of sediment and water respectively, and ϕ is the porosity. Using the values as shown in Table 2.2 in equations (2.3) and (2.4), gives $a \approx 2 \times 10^{-7}$ m^2s^{-1}. Using this value in equation (2.2), with a mean sediment thickness of 260 m (Figure 2.4), yields $\tau \sim 10{,}000$ yrs. Because the seismic data suggests several episodes of sediment emplacement (Figure 2.4), heat flow through the sediment pile should have equilibrated with the basement rock. Hence, sedimentation likely has a negligible effect on the observed heat flow.

The low mean heat flow could also reflect advective loss due to hydrothermal circulation, which could redistribute basal heat flux by lateral fluid flow in the basement rocks. This process is commonly observed in young oceanic crust where basement outcrops penetrate the sediment and allow seawater inflow and outflow [e.g., *Lister*, 1972; *Fisher et al.*, 1990; *Hutnak et al.*, 2008; *Anderson et al.*, 2012]. The eastward increase in heat flow across the sediment pond, from younger to older crust, is consistent with fluid flow from west to east. Given the bathymetry of the fracture zone bounding the sediment pond (Figures 2.2, 2.3 and 2.4), recharge could occur through exposed basement relief along the western margin of the sediment pond. The discharge in the east likely occurs at the poorly sedimented basement exposure where a possible normal fault intersects the seafloor (Figure 2.4). The distance between the interpreted recharge and discharge areas is ~ 9300 m. The small outcrop on the west is chosen as the recharge zone, but the recharge region could be somewhat broader. Note there is another, smaller sediment pond to the east (Figure 2.3) for which we have no heat flow data. Given its topography and sediment cover, there could also be advective heat transfer within it.

To determine the redistribution of heat by lateral flow through the basement, we apply the well-mixed aquifer model first derived by *Langseth* and *Herman* [1981] and subsequently used by *Fisher and Becker* [2000], *Rosenberg et al.* [2000] and *Anderson et al.* [2012] to describe outcrop-to-outcrop hydrothermal circulation. In this model, water absorbs the heat transferred from the lithosphere below and as it flows laterally in the highly-porous, igneous basement it simultaneously loses heat by conduction to the overlying sediment layer (Figure 2.5). Assuming advection of heat is much greater than lateral conduction in the aquifer, the steady state thermal balance can be expressed as [*Langseth and Herman*, 1981],

$$\rho_f c_f u h_a \frac{dT(x)}{dx} = q_b - K_s \frac{T(x)}{l} \quad . \tag{2.5}$$

Solving equation (5) with boundary condition, $T = T_0$ at $x = x_0$, yields,

$$\frac{q(x)}{q_b} = 1 + \left(\frac{q(x_0)}{q_b} - 1\right)\left[e^{\frac{a^*}{uh_a l}(x_0 - x)}\right], \quad (2.6)$$

where $a^* = Ks/\rho_f c_f$; $q(x)$ is heat flow at distance of x from x_0; $q(x_0)$ is the heat flow at distance x_0; x_0 is the distance of the first heat flow measurement from the recharge outcrop (see in Table 2.1). To determine the volumetric flow rate, uh_a, per unit length perpendicular to the heat flow profile, we note that the heat flow data follow a nearly linear trend from west to east along the profile. We therefore assume the exponential term in equation (2.6) is small and expand the exponential in a Taylor expansion leading to a linear expression for $q(x)$,

$$q(x) = q(x_0) + \frac{a^*}{uh_a l}(q(x_0) - q_b)(x_0 - x). \quad (2.7)$$

By performing a Monte Carlo simulation (using MATLAB) for regression analysis, we obtain an estimate of 0.008±0.001 mWm^{-3} for the slope $(a^*/ uh_a l)(q(x_0)-q_b)$ that fits the data (Figure 2.6) to within the 95% confidence interval and yields an estimate for the volumetric flow rate per unit length, uh_a, of ~ 400 ± 250 m^2yr^{-1}.

We estimate the permeability, k, of the crustal aquifer by using the flow rate uh_a derived from equation (7) in Darcy's Law:

$$uh_a = -\frac{kh_a}{h}\nabla P, \quad (2.8)$$

where η is the dynamic viscosity of the fluid and ∇P is the pressure gradient driving the flow. We write Darcy's Law in this form because the aquifer thickness is unknown and only the product uh_a can be estimated directly from the heat flow data. Following *Fisher and Becker* [2000], we assume that the pressure gradient driving the flow uh_a results from the buoyancy difference between the cold seawater entering the aquifer and the warmer fluid exiting it. Neglecting flow resistance in the recharge and discharge outcrops, equation (8) can be written as,

$$uh_a = \frac{\alpha g k \Delta T h_a (h_a + l)}{\nu L}, \quad (2.9)$$

where α is thermal expansion coefficient of water; g is the acceleration due to gravity; ΔT is the temperature difference between recharge and discharge; L is length of the horizontal fluid flow path, and ν is the kinematic viscosity of the fluid. Because the aquifer thickness occurs independently in equation (2.9) through the term $h_a + l$, to determine k, one needs to estimate both h_a and ΔT in equation (2.9). To obtain a reasonable range of estimates for k, we consider h_a = 100 m and 1000 m. By assuming that fluid enters the aquifer at the seawater temperature, taken to be 0 °C, and exits at the temperature of the sediment-basement interface at the end of the flow path L, we obtain an upper estimate of ΔT. Extrapolating the linear fit for the observed heat flow data, from equation (2.7), to 9300 m as shown in Figure 2.4(b), we estimate heat flow at the discharge, $q_d \approx 210$ mWm^{-2}. Writing the one-dimensional conductive heat flow equation as,

$$q_d = K_s \frac{T_d}{l}, \quad (2.10)$$

yields $T_d \approx 80$ °C, which is then the value of ΔT. Substituting this value of ΔT in equation (2.9), along with a mean sediment thickness l = 260 m, other parameters from Table 2.2, and uh_a = 400 m^2yr^{-1}, we obtain permeabilities of $\sim 10^{-11}$ and 10^{-12} m^2 for aquifer thicknesses of 100 and 1000 m, respectively.

2.5. Discussion

2.5.1. Robustness of the model

The mean conductive heat flow obtained across a sediment basin in the inactive part of the EFZ reported in this paper ranges between ≈ 40% and ≈ 80% of the predicted heat flow. The heat flow increases nearly linearly from west to east, which is opposite to that expected based on the age of the oceanic crust on either side of the fracture zone. A seismic reflection profile along the heat flow profile shows that sediment thickness varies irregularly but tends to increase from west to east and that the basin is bounded by outcrops, potentially allowing for seawater to enter and exit the crust. To interpret the observed heat flow deficit and the west to east increase in heat flow through the sediment, we constructed a 1D well-mixed aquifer model, which indicates that homogeneous west to east lateral flow through the basement rocks at an average flow rate of ≈ 400 ± 250 m^2 yr^{-1} per unit length perpendicular to the heat flow profile can explain the data. Assuming flow is driven by convection resulting from a temperature difference of ~ 80°C between the recharge and discharge sites, the aquifer permeability is estimated to range from ~ 10^{-11} m^2 to 10^{-12} m^2 for aquifer thickness between 100 m and 1000 m, respectively.

Key assumptions in the analysis presented in the previous section are that: (1) the well-mixed aquifer model is appropriate and (2) the temperature difference driving the flow is maximum, corresponding to the difference between cold seawater and the basement temperature near the discharge site.

The well-mixed aquifer model assumes that the temperature and flow rate do not vary significantly with depth in the basement. To explore this assumption, we consider the possibility that fluid convection is occurring in the basement rocks. For a porous layer with a given heat flux at the base and a fixed temperature at the surface, thermal convection occurs when the Rayleigh number, *Ra*, exceeds a critical value, Ra_c. Assuming the sediment and the base of the basement aquifer are impermeable, *Nield* [1968] shows that

$$Ra = \frac{\alpha g k \Delta T h_a}{a_b^* \nu} > Ra_c = 27.1, \qquad (2.11)$$

where $\Delta T = q_b h_a / K_b$ ≈15 °C and ≈ 150 °C for h_a = 100 m and 1000 m, respectively, is the temperature difference across the conducting layer, effective thermal diffusivity of basement rocks, $a_b^* = K_b/\rho_f c_f \approx 5 \times 10^{-7}$ m^2s^{-1} and K_b is the thermal conductivity of the basement rocks. From equation (2.11), the derived permeabilities of the aquifer, for Ra_c = 27.1, for ΔT = ≈ 15 °C and 150 °C are ~ 10^{-11} m^2 and 10^{-13} m^2, respectively. For a vigorous convection to occur in the aquifer, we assume *Ra* = 100 x Ra_c. Based on this *Ra*, for ΔT ≈ 15 °C and ≈ 150 °C permeabilitites of ~ 10^{-9} m^2 and ~ 10^{-11} m^2 are obtained. The permeability values for vigorous convection in the aquifer are somewhat higher than the values obtained from equation (2.9), but are not unrealistic. Moreover, the *k* values determined from equation (2.9) indicate that the aquifer beneath the sediment pond is likely to be convecting, which would tend to homogenize

the temperature distribution in the aquifer, except at boundary layers. Therefore the application of the well-mixed aquifer model is reasonable.

Another way to estimate the temperature difference driving the flow through the aquifer is to recognize that the mean heat flow deficit is ≈ 140 mWm^{-2}. Integrated along the west to east length of the basin, this corresponds to a total advective heat loss $H \approx 1.3 \times 10^6$ mWm^{-1}. Using the mean volumetric flow rate per unit length determined from equation (2.7), we can obtain a new estimate of ΔT. Writing,

$$H = \rho_f c_f u h_a \Delta T, \qquad (2.12)$$

Equation (2.12) gives ≈ 30°C. This estimate is considerably less than $\Delta T \approx 80$ °C used in equation (2.9) to determine the permeability. This smaller value of ΔT suggests that thermal conduction may have warmed the recharge fluid or cooled the discharge fluid. Using $\Delta T = 30$ °C in equation (2.9) yields an estimate of $k \sim 10^{-10}$ m^2 and 10^{-12} m^2 for $h_a = 100$ m and 1000 m respectively. These higher values of permeability further support the validity of the aquifer model. We also recognize that a maximum value of ΔT was used in calculating k in the analysis section when compared to the one used above. As can be seen in Figure 2.3, the length of the horizontal flow path, L, is a minimum. If recharge occurred through a larger part of the elevated topographic feature at the western boundary of the sediment pond, L would be somewhat longer than estimated, the buoyancy difference driving the flow would be smaller, and the corresponding permeability would be slightly larger. The uncertainty in the aquifer thickness, h_a, is much greater than the uncertainty in L, however, so small changes in L would not change the estimated basement permeability appreciably.

The estimates of crustal permeability derived in this paper for the Ecuador Fracture Zone are similar to estimates in ridge flank environments in other settings [*Fisher*, 1998], and similar to those obtained at Hole 504b [*Becker et al.*, 1983; *Carlson*, 2011]. Given our limited knowledge of the basement structure and its permeability, however, we cannot conclude whether a 100 m or a 1000 m thick aquifer is more appropriate for this region.

2.5.2. Implications of the results

In the analysis presented here, the ≈ 50% heat deficit in the observed heat flow implies that the mean advective heat flow q_{adv} = 140 mWm^{-2}. For a ~ 10 km long aquifer length and assuming a ~ 10 km length perpendicular to the heat flow profile, the total advective heat output from a 10 km^2 area is ≈ 0.15 MW. This heat output is small compared to the heat output of the ridge-crest hydrothermal systems, which is ~ 100 MW over a smaller area of $10^3 - 10^4$ m^2. Hence on a global scale it would not appear that hydrothermal heat loss from fracture zones is significant.

Roland et al. [2010] develop a numerical model of the thermal regime of the active transform region between two ridge segments. In their model, they parameterize the effect of hydrothermal circulation by an enhanced thermal conductivity that is a function of a depth-dependent Nusselt number. Their model does not consider the inactive fracture zone extension. Currently, the only model for heat transfer in the fracture zone extension involves lateral conductive heat transfer from the younger to the older plate [*Louden and Forsyth*, 1976]. This model has then been used to explain the geoid and topographic signatures of fracture zone extensions as they age [e.g., *Sandwell and Schubert*, 1982; *Sandwell*, 1984; *Pockalny et al.*, 1996]. The heat flow profile reported here for the Ecuador Fracture Zone shows that lateral heat advection via outcrop-to-

outcrop fluid flow may significantly increase the rate of heat transfer from the younger to the older plate and hence might affect the topographical evolution and geoid signatures of fracture zones. Additional heat flow studies are needed to confirm such effects.

2.6. Conclusions

Based on our analysis of a set of 18 conductive heat flow measurements in a sediment pond in the EFZ, we conclude the following:

1. The mean conductive heat flow is ~ 160 mWm^{-2} which is ≈ 50% of the mean basal heat flux yielded by a pure conduction model.
2. For rapid sedimentation to depress heat flow, the sediments should have been emplaced a relatively short time ago of ~ 10, 000 years to explain the heat flow deficit.
3. Lateral advective heat transfer by fluids flowing from a recharge outcrop in the west to the discharge fault in the east is consistent with the eastward increase in heat flow values and could explain the deficit in heat flow.
4. Applying a well-mixed aquifer model to determine the redistribution of heat flow through the basement, we estimate a mean volumetric flow rate of ≈ 400 m^2yr^{-1}.
5. Estimates of permeabilities in the basement, based on the mean volumetric flow rate, are ~ 10^{-11} and 10^{-12} m^2 for aquifer thicknesses of 100 and 1000 m, respectively.

Based on the Rayleigh number analysis for onset of fluid convection and vigorous convection in the basement rocks, the permeability estimates further support the application of the well-mixed aquifer model.

Therefore, the heat flow data in the EFZ shows that lateral heat advection is likely an important heat transfer mechanism in fracture zones. The analysis of the rate of heat transfer using a simple well mixed aquifer model suggests that crustal permeability of the fracture zones is similar to that of typical oceanic crust. Lateral advective heat transfer from the young to old plate significantly enhances the rate of lateral heat transfer obtained from conduction models. Outcrop-to-outcrop lateral heat transfer in fracture zones may affect the evolution of fracture zones as they age, but additional studies are needed to confirm the general importance of this process.

Given the lack of heat flow studies in transform and fracture zone settings, our model and results could be used to constrain models of fracture zone settings and also transform faults. Our study demonstrates that our understanding of these pervasive geological features is incomplete. To address this issue, the acquisition of more heat flow data along with other geological and geophysical data would make a significant contribution to our understanding of the role of fluid flow and advective heat transport in oceanic fracture zones.

Acknowledgments. We thank the two anonymous reviewers for their insightful comments. This research was supported in part by NSF Grants OCE 1353114 and 1558797 to RPL and Grants NSF OCE 1353003 and 1558824, to RNH. The NERC OSCAR project grant NE/I027010/1 (Hobbs & Peirce 2015) underpinned this work. The authors would like to thank the officers, crew, technicians and science party on board the RRS James Cook during cruises JC112, JC113 and JC114. The MCS data were processed using Globe Claritas by Ahmed Alhamad as his undergraduate dissertation project at Durham. The swath bathymetry was cleaned and processed

using QPS Fledermaus by Gavin Haughton from the National Oceanographic Centre. Yang Li, Durham University, UK, provided the Monte Carlo Matlab code for calculation of uncertainties.

2.7. References

Anderson, B.W., L.A. Coogan, and K.M. Gillis (2012), The role of outcrop-to-outcrop fluid flow in off-axis oceanic hydrothermal systems under abyssal sedimentation conditions, *J. Geophys. Res.*, 117, B05103, doi:10.1029/2011JB009052.

Behn, M.D., M.S. Boettcher, and Hirth, G. (2007), Thermal structure of oceanic transform faults, *Geology*, 35(4), 307-310.

Becker, K., M.G. Langseth, R.P. Von Herzen, and R.N. Anderson (1983), Deep crustal geothermal measurements, hole 504B, Costa Rica Rift, *Journal of Geophysical Research: Solid Earth*, 88(B4), 3447-3457.

Carlson, R. L. (2011), The effect of hydrothermal alteration on the seismic structure of the upper oceanic crust: Evidence from Holes 504B and 1256D, *Geochemistry, Geophysics, Geosystems*, 12(9).

Dziak, R.P., C.G. Fox, R.W. Embley, J.L. Nabelek, J. Braunmiller, and R.A, Koski (2000), Recent tectonics of the Blanco Ridge, eastern Blanco transform fault zone, *Marine Geophysical Researches*, 21(5), 423-450.

Fisher, A.T. (1998), Permeability within basaltic oceanic crust, *Rev. Geophys.*, 36, 143-182.

Fisher, A.T., K. Becker, T.N. Narisimhan, M.G. Langseth, and M.J. Mottl (1990), Passive, off-axis convection near the southern flank of the Costa Rica Rift, *J. Geophys. Res.*, 95, 9343-9370.

Fisher, A.T. and K. Becker (2000), Channelized fluid flow in oceanic crust reconciles heat-flow and permeability data, *Nature,* 403, 71-74.

Hey, R., G.L. Johnson, and A. Lowrie (1977), Recent plate motions in the Galapagos area, *Geological Society of America Bulletin*, 88(10), 1385-1403.

Hutchison, I. (1985), The effects of sedimentation and compaction on oceanic heat flow, *Geophysical Journal International,* 82(3), 439-459.

Hutnak, M., and A.T. Fisher (2007), Influence of sedimentation, local and regional hydrothermal circulation, and thermal rebound on measurements of seafloor heat flux, *Journal of Geophysical Research: Solid Earth*, 112(B12).

Hutnak, M., A.T. Fisher, R. Harris, C. Stein, K. Wang, G. Spinelli, M. Schindler, H. Villinger, and E. Silver (2008), Large heat and fluid fluxes driven through mid-plate outcrops on ocean crust, *Nature Geosci., 1*, 611-614.

Kastens, K. A., K.C. Macdonald, S.P. Miller, and P.J. Fox (1986), Deep tow studies of the Vema Fracture Zone: 2. Evidence for tectonism and bottom currents in the sediments of the transform valley floor, *Journal of Geophysical Research: Solid Earth*, 91(B3), 3355-3367.

Langseth, M.G., X. Le Pichon, and M. Ewing (1966), Crustal structure of the mid-ocean ridges: 5. Heat flow through the Atlantic Ocean floor and convection currents, *Journal of Geophysical Research*, 71(22), 5321-5355.

Langseth, M.G., and M.A. Hobart (1976), Interpretation of heat flow measurements in the Vema fracture zone, *Geophysical Research Letters*,3(5), 241-244.

Langseth, M.G. and B.M. Herman (1981), Heat transfer in the oceanic crust of the Brazil Basin, *J. Geophys. Res.*, 86, 10805-10819.

Lister, C.R.B. (1972), On the thermal balance of a mid-ocean ridge, *Geophysical Journal International*, 26(5), 515-535.

Louden, K.E., and D.W. Forsyth (1976), Thermal conduction across fracture zones and the gravitational edge effect, *Journal of Geophysical Research,* 81(26), 4869-4874.

Menard, H.W., and T. Atwater (1969), Origin of fracture zone topography, *Nature,* 222, 1037-1040.

Nield, D.A. (1968), The Rayleigh—Jeffreys problem with boundary slab of finite conductivity, *Journal of Fluid Mechanics,* 32(02), 393-398.

Pockalny, R.A., P. Gente, and R. Buck (1996), Oceanic transverse ridges: A flexural response to fracture-zone–normal extension, *Geology,* 24(1), 71-74.

Roland, E., M.D. Behn, and G. Hirth (2010), Thermal-mechanical behavior of oceanic transform faults: Implications for the spatial distribution of seismicity, *Geochemistry, Geophysics, Geosystems,* 11(7).

Rosenberg, N.D., A.T. Fisher, and J.S. Stein (2000), Large-scale lateral heat and fluid transport in the seafloor: revisiting the well-mixed aquifer model, *Earth and Planetary Science Letters*, 182(1), 93-101.

Sandwell, D.T., and G. Schubert (1982), Geoid height-age relation from SEASAT altimeter profiles across the Mendocino Fracture Zone, *Journal of Geophysical Research: Solid Earth,* 87(B5), 3949-3958.

Sandwell, D.T. (1984), Thermomechanical evolution of oceanic fracture zones, *Journal of Geophysical Research*, 89(B13), 11401-11413.

Stein, C.A. and S. Stein (1994), Constraints on hydrothermal heat flux through the oceanic lithosphere from global heat flow, *J. Geophys. Res.*, 99, 3081-3095.

Stein, J.S., and A.T. Fisher (2001), Multiple scales of hydrothermal circulation in Middle Valley, northern Juan de Fuca Ridge: Physical constraints and geologic models, *Journal of Geophysical Research: Solid Earth,* 106(B5), 8563-8580.

Tuckwell, G.W., J.M. Bull and D.J. Sanderson (1996), Models of fracture orientation at oblique spreading centres, *Journal of the Geological Society*, 153(2), 185-189.

Vacquier, V., R.P. Von Herzen (1964), Evidence for connection between heat flow and the mid-atlantic ridge magnetic anomaly, *Journal of Geophysical Research,* 69(6), 1093-1101.

Villinger, H., and E.E. Davis (1987), A new reduction algorithm for marine heat flow measurements, *Journal of Geophysical Research: Solid Earth*, 92(B12), 12846-12856.

Von Herzen, R., and G. Simmons (1972), Two heat flow profiles across the Atlantic Ocean, *Earth and Planetary Science Letters*, 15(1), 19-27.

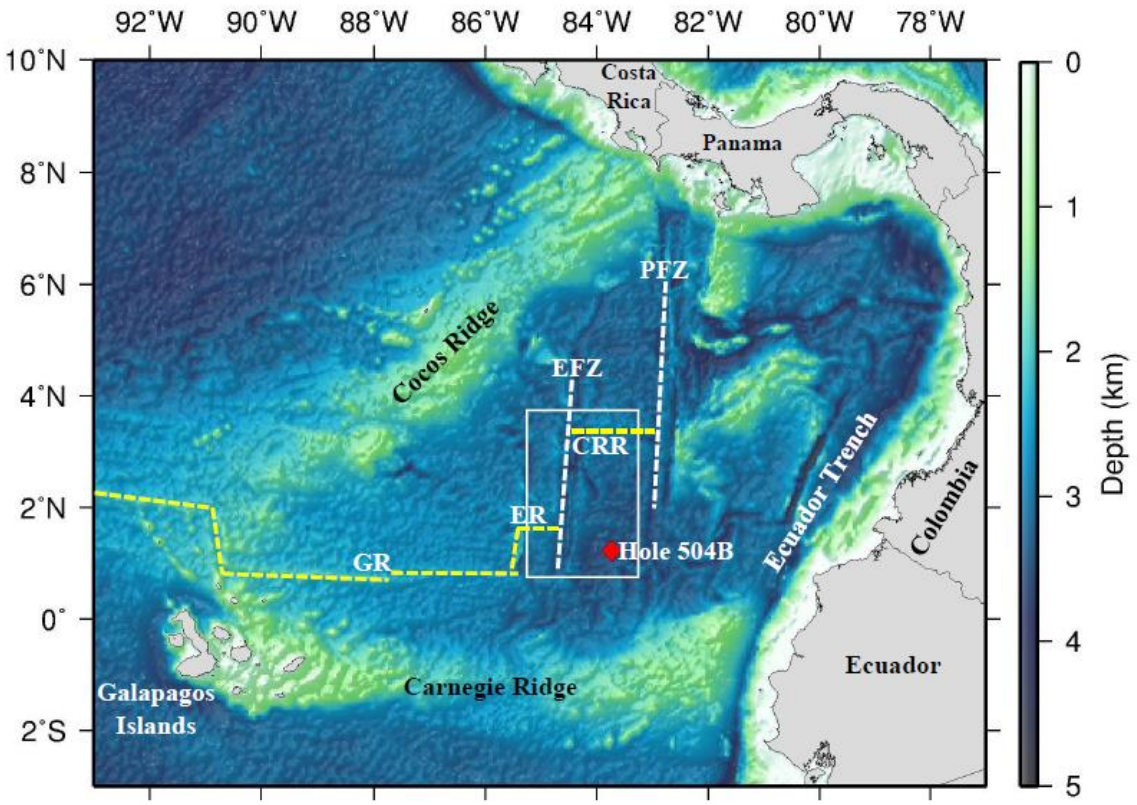

Figure 2.1. Map of the Panama Basin. The basin is bounded by the Cocos Ridge to the N and W, the Carnegie Ridge to the S, and the Ecuador Trench and Americas to the E. The dashed yellow lines show the spreading axis (CRR = Costa Rica Rift; ER = Ecuador Ridge; GR = Galapagos Spreading Center). The transforms bounding the CRR, EFZ = Ecuador Fracture Zone; PFZ = Panama Fracture Zone, are labeled and shown in white dashed lines. Red diamond shows the location of the ODP Hole 504B. The white box encloses the area where geophysical measurements were made during cruises JC112, JC113 and Sonne 0238.

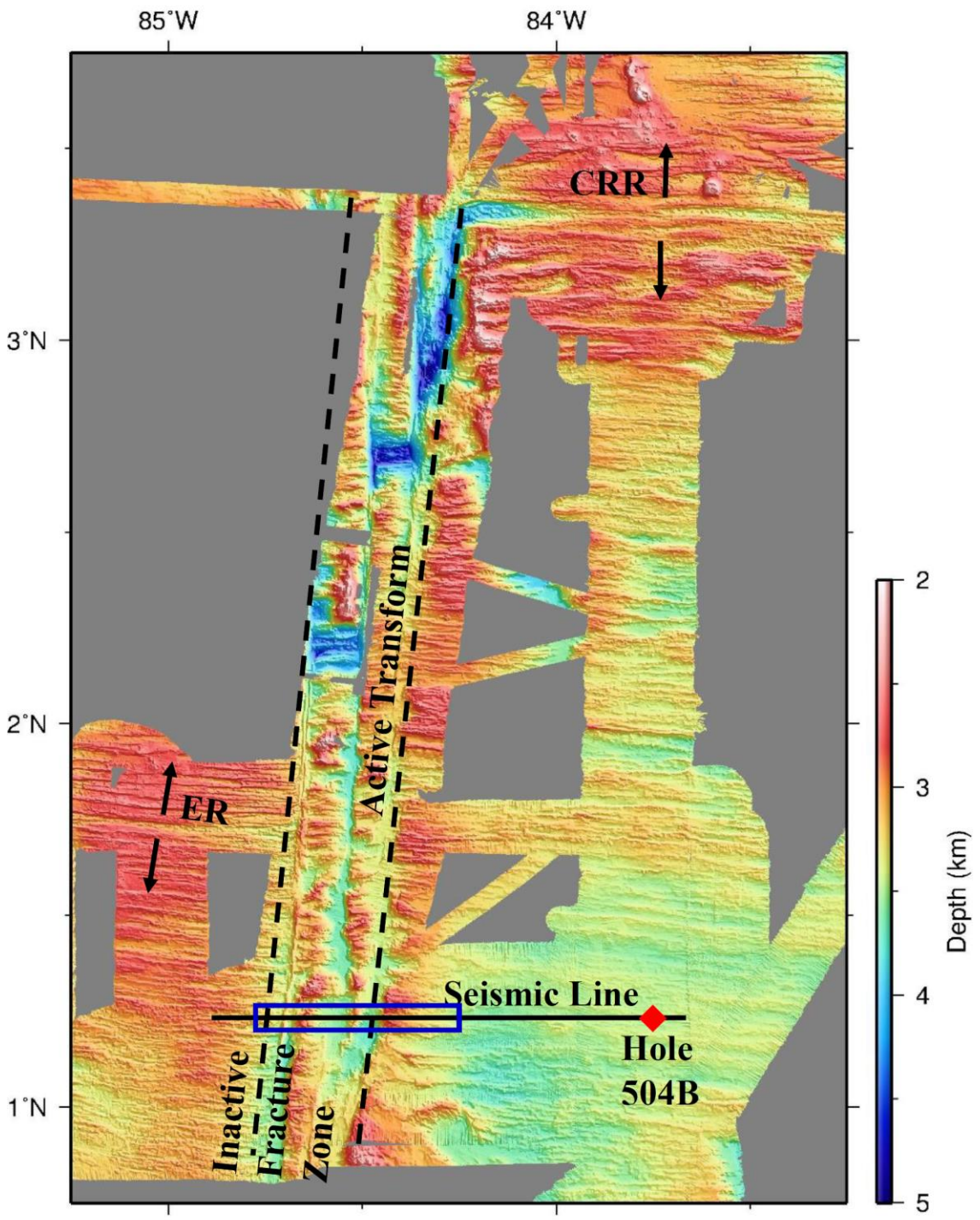

Figure 2.2. Bathymetry data showing the EFZ (region bound by black dashed lines). CRR = Costa Rica Rift; ER = Ecuador Ridge. The seismic profile, reproduced in Figure 3, extends to Hole 504B in the east. The blue box highlights the seismic profile shown in Figure 2.3 which contains the sediment pond where heat flow measurements were taken. The heat flow measurements are collocated with the seismic reflection line.

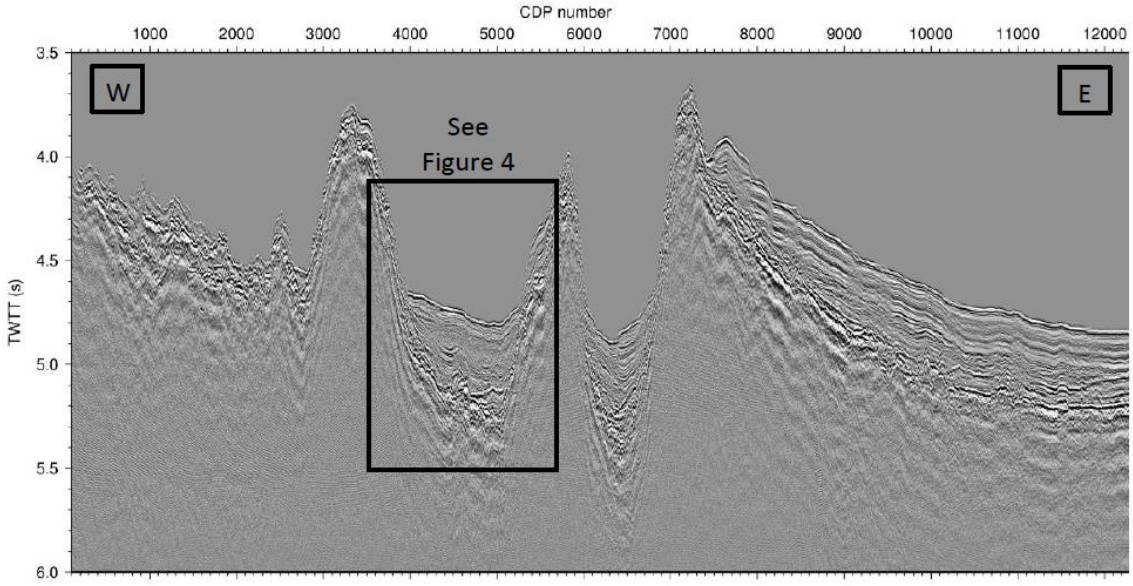

Figure 2.3. The post-stack migrated seismic image over the EFZ from west (W) to east (E) along a section of the seismic profile line shown in Figure 2.2. The box shows the sediment pond where the heat flow measurements were made. The age of the crust on the west side is 1.5 Ma with predicted basal heat flow $q_b \approx 400$ mWm^{-2} and the age on the east is 6 Ma with $q_b \approx 200$ mWm^{-2}.

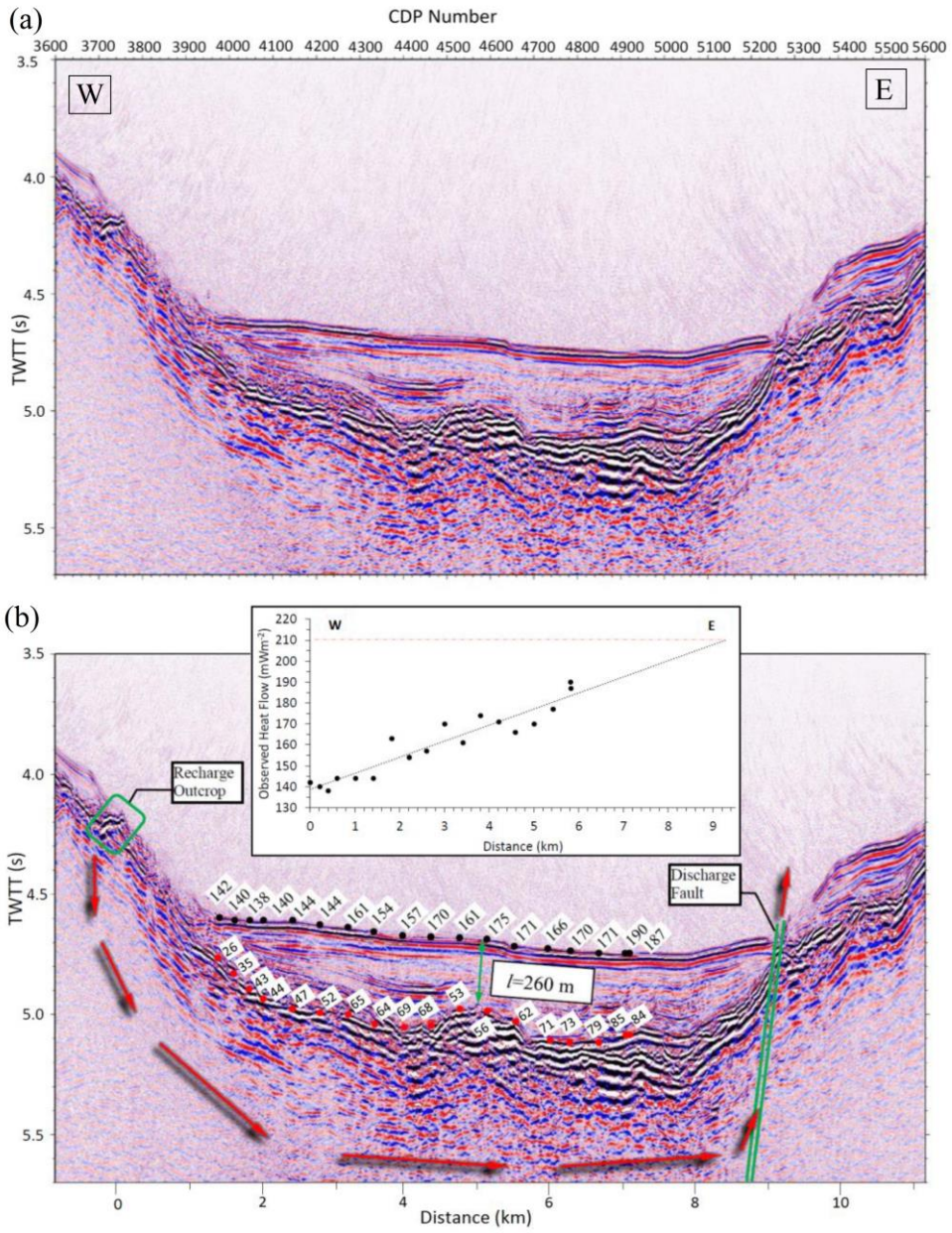

Figure 2.4. (a) The pre-stack time migrated seismic image over the sediment pond. The vertical axis is two-way travel time (TWTT). (b) Heat flow data and schematic model of fluid flow. The red arrows indicate the direction of fluid flow. The black circles show the location and value of heat flow measurements in mWm^{-2} (Table 2.1). Red circles are temperatures at sediment-basement interface in °C (Table 2.1). The inset displays heat flow as a function of distance and shows the general increase in the observed heat flow from W to E. The black dotted line is the linear trend line determined from Monte Carlo analysis shown in Figure 2.6 and red dashed line is the extrapolation of heat flow to 9300 m (discharge fault). *l* is average sediment thickness.

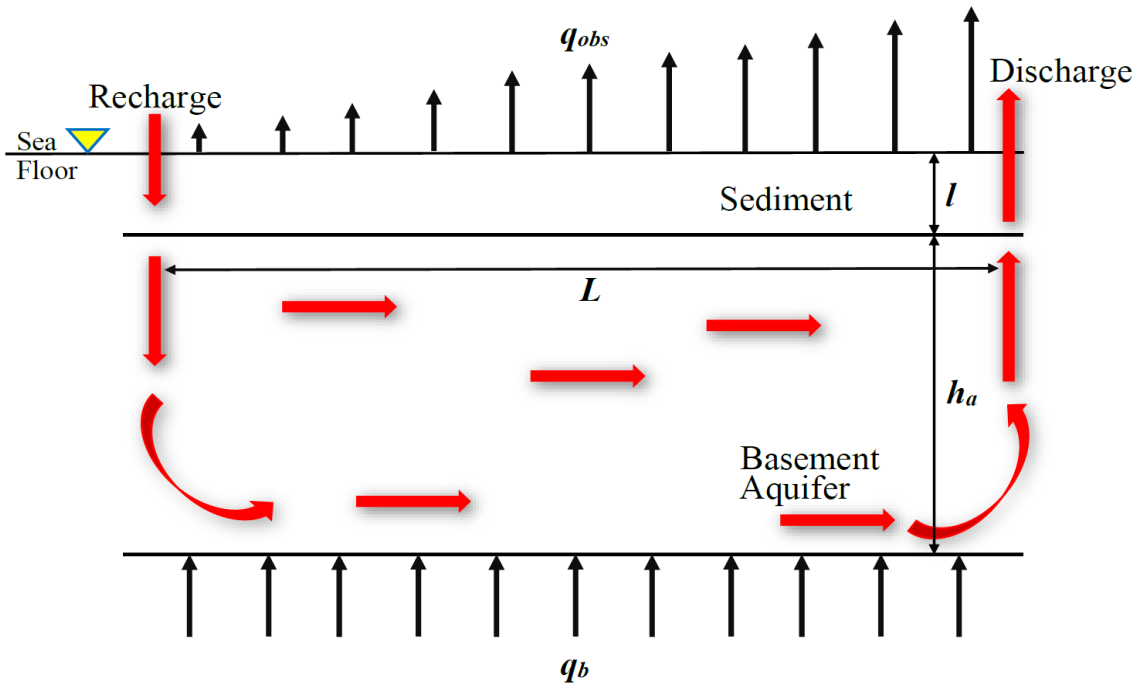

Figure 2.5. A well-mixed aquifer flow model modified from *Langseth and Herman*, 1981; *Fisher and Becker*, 2000. Refer to Table 2.2 for parameters shown in this figure.

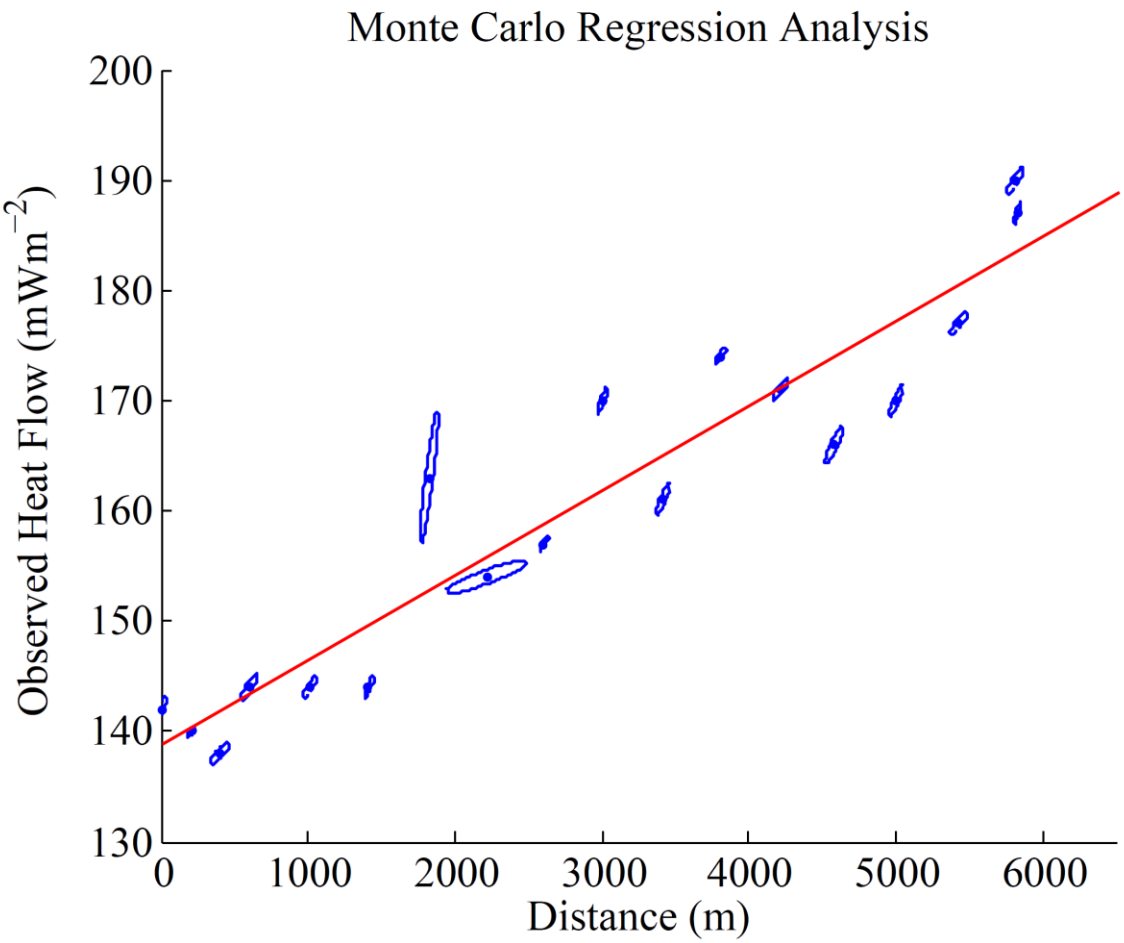

Figure 2.6. Regression analysis of the conductive heat flow measurements based on Monte Carlo simulation. 18 heat flow determinations and their measurement and distance uncertainties as a function of distance. Slope = 0.008±0.001 mWm^{-3} and Intercept = 139±5 mWm^{-2} are used in equation (2.7) to determine the volumetric flow rate through the basement aquifer.

Table 2.1. Conductive Heat Flow data from a sediment pond in the Ecuador Fracture Zone

Datum	Latitude	Longitude	Distance from recharge outcrop*	Thermal Gradient	Temperature at sediment-basement interface	Thermal Conductivity	Heat Flow
	(°N)	(°W)	(m)	(°C km^{-1})	(°C)	(W m^{-1} K^{-1})	(mW m^{-2})
PB01-01	1.2334	-84.6175	1411±12	193	26	0.7	142±0.5
PB01-02	1.2334	-84.6156	1622±12	193	35	0.7	140±0.2
PB01-03	1.2335	-84.6139	1811±17	196	43	0.7	138±0.4
PB01-04	1.2336	-84.6121	2011±23	191	44	0.8	144±0.4
PB01-05	1.2336	-84.6084	2422±17	188	47	0.8	144±0.4
PB01-06	1.2338	-84.6048	2822±12	196	52	0.7	144±0.4
PB01-07	1.2338	-84.6011	3233±12	231	65	0.7	163±2.4
PB01-08	1.2338	-84.5976	3621±100	214	64	0.7	154±0.6
PB01-09	1.2338	-84.5941	4010±12	217	69	0.7	157±0.3
PB01-10	1.2338	-84.5905	4410±12	224	68	0.8	170±0.5
PB01-11	1.2338	-84.5868	4821±12	226	53	0.7	161±0.6
PB01-12	1.2338	-84.5833	5210±17	253	56	0.7	174±0.3
PB01-13	1.2340	-84.5796	5622±23	247	62	0.7	171±0.4
PB01-14	1.2340	-84.5763	5988±23	235	71	0.7	166±0.7
PB01-15	1.2341	-84.5725	6411±17	242	73	0.7	170±0.6
PB01-16	1.2341	-84.5687	6833±23	244	79	0.7	177±0.4
PB01-17	1.2342	-84.5652	7222±23	274	85	0.7	190±0.5
PB01-18	1.2342	-84.5651	7233±12	211	84	0.9	187±0.4
							Mean Heat Flow =160±0.5

* Recharge outcrop is considered to be at 0 m.

Table 2.2. Parameters and Values

Symbol	Definition	Value	Units
a	Thermal diffusivity of sediment-water composite medium	2×10^{-7}	$m^2\ s^{-1}$
a^*	Effective thermal diffusivity	2×10^{-7}	$m^2\ s^{-1}$
a_b^*	Effective thermal diffusivity of basement rocks	5×10^{-7}	$m^2\ s^{-1}$
c_f	Specific heat of water	4200	$J\ kg^{-1}\ K^{-1}$
c_s	Specific heat of sediments	1000	$J\ kg^{-1}\ K^{-1}$
g	Acceleration due to gravity	9.81	$m\ s^{-2}$
h_a	Aquifer thickness	100-1000	m
H	Total advective heat loss		mWm^{-1}
k	Permeability of crustal aquifer		m^2
K_b	Thermal conductivity of the basement rocks	2.0	$Wm^{-1}K^{-1}$
K_s	Thermal conductivity of the sediments	0.7	$Wm^{-1}K^{-1}$
l	Mean sediment thickness	260	m
L	Horizontal fluid flow path length	9300	m
q_{adv}	Mean advective heat flow	140	mWm^{-2}
q_b	Basal heat flux	≈200-400	mWm^{-2}
q_d	Heat flow at the discharge		mWm^{-2}
q_{obs}	Mean observed heat flow	160	mWm^{-2}
Ra, Ra_c	Rayleigh number, and critical value		
t	Age of oceanic crust		Ma
T_d	Temperature at discharge		°C
u	Darcian velocity of fluid		$m\ yr^{-1}$
α	Thermal expansion coefficient of seawater	10^{-4}	$°C^{-1}$
η	Dynamic viscosity of fluid		$kg\ m^{-1}\ s^{-1}$
ϕ	Porosity of sediments	0.5	
ν	Kinematic viscosity of the fluid	10^{-6}	$m^2\ s^{-1}$
ρ_f	Density of water	1000	$kg\ m^{-3}$
ρ_s	Density of sediments	2300	$kg\ m^{-3}$
τ	Time scale for heat conduction through sediment pile		yrs

Chapter 3

Evolution of Heat Flow, Hydrothermal Circulation and Permeability on the Young Southern Flank of the Costa Rica Rift

Kannikha Parameswari Kolandaivelu[1], Robert N. Harris[2], Robert P. Lowell[1], Adam H. Robinson[3], Dean J. Wilson[3], and Richard W. Hobbs[3]

[1]Department of Geosciences, Virginia Polytechnic Institute and State University, Blacksburg, VA 24061
[2]College of Earth, Ocean, and Atmospheric Sciences, Oregon State University, Corvallis, OR 97331
[3]Department of Earth Sciences, Durham University, Durham DH1, United Kingdom

In revision based on reviews received on October 24th, 2018, Geophysical Journal International.

Abstract

We analyze 67 new conductive heat flow measurements at five sites ranging in age between approximately 1.6 and 5.7 Ma from the southern flank of the Costa Rica Rift (CRR). The heat flow data are co-located with a high-resolution multi-channel seismic line that extends between the ridge axis and ODP hole 504B. For the five heat flow sites, the mean observed conductive heat flow, q_{obs}, is ~ 80 mWm^{-2}. This value is approximately 30% of the mean lithospheric heat flux expected from a half-space conductive cooling model, indicating that hydrothermal processes account for about 70% of the heat loss. The advective heat loss fraction varies from site to site and is driven by a combination of supercritical convection in layer 2A, outcrop to outcrop circulation, discharge through faults, and flow through thinly-sedimented basement highs. Advective heat loss diminishes rapidly between ~4.5 and~5.7 Ma, which contrasts with plate cooling reference models that predict a significant deficit in conductive heat flow up to ages ~ 60-70 Ma. At ~ 5.7 Ma the CRR topography is buried under about 250 m of sediment, and hydrothermal circulation in the basement becomes subcritical or perhaps marginally critical. The absence of advective heat loss at ~ 5.7 Ma at the CRR is thus a function of both burial of basement exposure under the sediment load and a reduction in basement permeability that

possibly occurs as result of mineral precipitation and original permeability at the time of formation. However at the location of ODP 504B (6.9 Ma crust) the permeability of the shallow crust appears to be much greater than at 5.7 Ma, indicating that crustal permeability does not decline monotonically as a function of lithospheric age.

3.1. Introduction

The temporal and spatial evolution of oceanic crust and lithosphere are largely controlled by thermally mediated processes. Parsons & Sclater (1977), Stein & Stein (1994), Hasterok (2013) and Qiuming (2016) have arrived at somewhat different plate cooling models based on global heat flow determinations and have fitted them with various functions based on oceanic crustal age. The widely used Stein & Stein (1992) model was derived from a global analysis of heat flow and bathymetry data and suggests that predicted conductive heat flow from cooling lithosphere follows the expressions:

$$q_b = 510\ \tau^{-1/2} \quad \text{for } 1\text{ Ma} \leq \tau \leq 55\text{ Ma} \tag{3.1}$$

where q_b is the heat flow in mWm^{-2} and τ is the lithospheric age in Ma.

Measurements of conductive heat flow, particularly in young crust, typically lie well below conductive cooling curves (Baker *et al.* 1991; Langseth *et al.* 1992; Fisher *et al.* 2003; Hutnak *et al.* 2008). This discrepancy has long been attributed to heat loss by hydrothermal circulation (e.g., Elder, 1965; Langseth & Von Herzen, 1970; Lister, 1972) and on a global scale, the difference between observed and predicted conductive heat loss indicates that hydrothermal circulation accounts for about 30% of the global oceanic heat flux (e.g., Williams & Von Herzen, 1974; Sclater *et al.* 1980; Elderfield & Schultz, 1996; Davies & Davies, 2010; Hasterok, 2013). Of this, approximately 20% to 30% occurs between 0 and 1 Ma, with the remainder occurring off axis (Stein & Stein, 1994; Elderfield & Schultz, 1996). Figure 3.1a shows the predicted cooling curve from equation (3.1) along with globally observed values with their standard deviation averaged in 2 Ma bins.

The character of hydrothermal circulation and heat transfer changes as the crust and lithosphere age from "active" high-temperature magma-driven hydrothermal circulation at ages <0.1 Ma (Macdonald, 1982) to "passive" lower temperature circulation on the ridge flanks (Lister, 1982). The style of ridge flank hydrothermal circulation also evolves with lithospheric age. Passive circulation may initially extend to a depth of 6 km into the young crust (Cherkaoui *et al.* 2003; Craft & Lowell, 2009; Theissen-Krah *et al.* 2011; Hasenclever *et al.* 2014). Depending on the spreading rate and depth of circulation, this deep crustal cooling may affect thermal regime of the ridge flank to an age of ~ 5 Ma; for a spreading rate of 3-4 cm/a and a circulation depth of 2 km, however, the effect of deep crustal cooling is likely to be small for lithosphere greater than 1 Ma (Spinelli & Harris, 2011). As the lithosphere ages the circulation tends to be restricted to the highly permeable layer 2A extrusives (Fisher, 1998; Becker & Davis, 2004); and as sediment thickness increases, recharge and discharge becomes restricted to exposed basement and faults (Wheat *et al.* 2004; Hutnak *et al.* 2006; 2008; Fisher & Harris, 2010; Anderson *et al.* 2012).

As the thickness of low permeability sediments increases and oceanic basement topography becomes fully covered, fluid discharge declines. Moreover, mineral precipitation and alteration may reduce crustal permeability, and reduced buoyancy forces may also impact the vigor of hydrothermal circulation (e.g., Jarrard *et al.* 2003). The conductive heat flow gradually

approaches the predicted lithospheric cooling curve due to these processes that decrease and increase the driving and impeding forces of flow, respectively.

When the conductive heat flow and the cooling curve coincide, the crust is termed "sealed" (e.g., Anderson & Hobart, 1976; Stein & Stein, 1994), implying that hydrothermal circulation no longer affects the surface heat flow significantly. A statistical analysis of the global heat flow data set indicates that on average the sealing age corresponds to a basement age of 65±10 Ma (Figure 1a) (Stein & Stein, 1994). This condition does not mean that hydrothermal circulation is absent. Rather it indicates that if hydrothermal circulation is present it is simply redistributing heat within the crust and does not transfer heat by advection from the crust to the ocean (e.g., Embley *et al.* 1983; Von Herzen, 2004; Fisher & Von Herzen, 2005).

The dominant mechanism leading to the cessation of advective heat loss through the seafloor is not clear. Based on their analysis of the global data set, Stein & Stein (1994) argue that the sealing age indicates that hydrothermal flow decreases as a result of decreased porosity and permeability in the crustal extrusives (layer 2A) rather than from burial by sediment. This argument runs counter to results from heavily sedimented ridges. Detailed heat flow studies on the thickly sedimented eastern flank of the Juan de Fuca Ridge (JDFR) (Davis *et al.* 1997; 1999; Fisher *et al.* 2003; Spinelli & Fisher, 2004) show that mean observed heat flow reaches the predicted curve at ~ 1.5 Ma. At the Costa Rica Rift (CRR) flank near ODP Hole 504B the mean heat flow approaches the predicted cooling curve at ~ 6.9 Ma (Hobart *et al.* 1985; Langseth *et al.* 1983, 1988, Davis *et al.* 2004). These studies suggest that the accumulation of relatively impermeable and laterally continuous sediment is the likely cause of a sealed system at these locations. Further, global compilations of permeability measurements and seismic velocity indicates that the greatest change in the physical properties of the basement occurs in the first 10 Ma (Fisher & Becker, 2000), leaving the role of permeability in the sealing age an open question.

Heat flow studies on the flanks of young heavily sedimented oceanic crust such as JDFR and CRR provide opportunities to better understand the evolution of hydrothermal circulation and mechanisms of advective heat transport within a limited age and distance from the spreading center. In addition, such studies provide insight into crustal alteration (e.g., Alt, 1995), seismic velocity structure (e.g., Carlson, 2011, 2014) and microbial processes (e.g., Huber *et al.* 2003) that are linked to the thermal regime of the crust.

In this paper, we analyze 67 new conductive heat flow measurements from the southern flank of the CRR at sites ranging in age between ~1.6 and ~ 5.7 Ma. In this analysis we also include previously collected heat flow data (Anderson & Hobart, 1976; Langseth *et al.* 1983, 1988; Hobart *et al.* 1985; Davis *et al.* 2003, 2004). The new sites are labeled PB02 to PB06 (Figure 3.1b) and are co-located along a seismic reflection and multibeam bathymetry profiles which enable an integrated analysis that elucidates the influence of basement topography and sediment thickness on fluid flow, advective heat transport, and changes in the hydrothermal regime as the crust evolves with age. Although the heat flow profile presents a 2D view of the thermal structure of the ridge flank, the bathymetry shown in Figure 3.2 suggests relatively little variation perpendicular to the seismic line and heat flow profile.

3.2. Geologic Setting

The Panama Basin, located in the equatorial Pacific, is bounded by the Cocos Ridge to the north and west, Carnegie Ridge to the south, and Ecuador Trench and Americas to the east. Three spreading centers are located in the basin: Costa Rica Rift (CRR), Ecuador Rift (ER), and

the Galapagos Rift (GR) (Figure 3.2). The southern flank of the CRR, the focus of our study, has an average half-spreading rate of approximately 3.3 cm yr^{-1} based on the distance from the CRR axis to the ODP Hole 504B of age 6.9 Ma (Wilson & Hey, 1995; Wilson *et al.* 2003). The green box (Figure 3.2) shows the region where complementary geophysical measurements were made. The seismic reflection profiles, the locations of heatflow and other geophysical data, including swath bathymetry are shown in Figure 3.2.

3.3. Data

3.3.1 Seismic Reflection Measurements

A 270 km high-resolution seismic reflection profile (RS-A), along which heat flow measurements were co-located, was collected with a GI airgun array with a source frequency ranging between 20 and 200 Hz recorded on a 4500 m multichannel hydrophone streamer with a 12.5 m group length. The resulting imaging of the sediment and upper oceanic crust provides a geologic framework for interpreting the heat flow data. The complete seismic section (Figure 3.3) shows that sediment thickness varies considerably with thin sediment accumulations at basement highs, and thicker sediment accumulations at basement lows; the mean sediment thickness increases from approximately 40 m at 1.6 Ma crust to 250 m at 5.7 Ma and older crust. The seismic profile also shows exposed basement, through going faults, and rough basement topography. However for crust older than 5.7 Ma, the basement topography is more subdued and becomes completely covered with sediment.

3.3.2 Heat Flow Data

Conductive heat flow measurements were acquired in sediments between 50 m to 250 m thick by means of a "violin-bow" type multi-penetration heat flow probe. It consists of a 3.5 m sensor tube that houses 11 thermistors and heater wire that is offset from a lance. The configuration allows the probe to be gravity-driven into the sediments and provides the sensitivity to make precise and accurate heat flow measurements while also being robust so that many measurements can be made by 'pogo-ing' the probe along the bottom. A weight stand containing the data logger and telemetry system sits above the thermistor tube. In addition to logging the temperature time series, the data logger also records tilt, pressure, time, and the bottom water temperature. An ultra-short baseline sensor attached 50 m above the probe provides precise navigation. The probe thus allows in-situ measurements of both the shallow thermal gradients and thermal conductivity in sediments on the seafloor to yield the heat flow. The analysis of heat flow measurements is based on the scheme presented by Villinger & Davis (1987) by which in-situ thermal conductivity, thermal gradient and heat flow are determined. Heat flow values were calculated using SlugHeat (Stein & Fisher, 2001). The in-situ thermal gradient is based on a temperature-time series collected for seven minutes, which is long enough to achieve partial equilibrium with the sediments. Equilibrium temperatures are then estimated through an extrapolation based on a line source model of radial heat conduction (Villinger & Davis, 1987). A calibrated heat pulse is then applied through the heater wire for ten seconds and a seven minute temperature decay provides data for determining thermal conductivity. The heat flow, thermal conductivities, thermal gradient values and sediment thicknesses for all sites are given in Table 3.1. Heat flow measurements were closely spaced to avoid aliasing the hydrothermal circulation signal and co-located with the swath bathymetry and seismic reflection data to better understand the measuring environment (e.g., Fisher & Harris, 2010).

3.4. Analysis

Figure 3.1b shows the 67 new measured heat flow values along with the previously published data (Anderson & Hobart, 1976; Langseth *et al.* 1983, 1988; Hobart *et al.* 1985; Davis *et al.* 2003, 2004) and predicted heat flow based on half-space cooling curve from equation 3.1a. Figure 3.1b shows heat flow transitioning from values of about 40 mWm^{-2} at 1.6 Ma to a mean value of 235 mWm^{-2} at 5.7 Ma, which lies near the predicted cooling curve. Previously published heat flow data indicated by open circles in Figure 3.1b also show that heat transfer transitions from advectively to conductively dominated values between ~ 4.4 and ~6.0 Ma.

The average measured heat flow of the new 67 measurements (Table 3.1) is ~ 85 mWm^{-2}. This value is considerably less than the average expected basal heat flow of ~ 280 mWm^{-2}, obtained by integrating equation (3.1) between 1.6 Ma and 5.7 Ma. The heat flow fraction (q_{obs}/q_b) is ~ 0.3 indicating that ~ 70% (~ 200 mWm^{-2}) of q_b is advected.

In order to quantify the mechanisms responsible for this advective heat loss, we construct a one-dimensional thermal conduction model of the sediment and basement as a function of age between 1.6 and 6.9 Ma at ODP Hole 504B. This model allows us to compare the expected temperature at the sediment-basement interface (termed "basement temperature") with the basement temperature derived from the observed heat flow measurements. The mathematical formulation is given in Appendix 3.A. The results given by equation (3.A.2) show that the conduction-derived basement temperature, expressed as the difference ΔT_s between seafloor and base of the sediment can be written as

$$\Delta T_s(h_s) = \frac{q_b h_s}{\lambda_s} = \frac{510x10^{-3} v_s \tau^{1/2}}{\lambda_s} \qquad (3.2)$$

where h_s is the sediment thickness, λ_s is the thermal conductivity of the sediment, and v_s is the sedimentation rate, which is assumed to be constant. Definitions and values of symbols are given in Table 3.2. Figure 3.4 shows the expected basement temperature versus age along with the average basement temperature for the 5 heat flow sites and the existing data. We use λ_s = 0.92 $Wm^{-1}K^{-1}$ (Davis *et. al.*, 2004), and v_s = 40 m/Ma. The observed basement temperature at each heat flow point is determined from the relation $q_{obs}=\lambda_s \Delta T_s/h_s$. The average basement temperature at each site is significantly less than predicted by conduction until approximately 5.7 Ma (Figure 3.4)

Assuming that these lower basement temperatures are caused by hydrothermal circulation, we combine the advective heat flow $q_{adv} \approx 200$ mW/m^2 from the CRR flank between 1.6 and 5.7 Ma and the mean basement temperature $<\Delta T_s>$ (Table 3.1), to estimate the mean advective mass flux $\rho_f u$ over this age interval is,

$$q_{adv} = \rho_f c_f u <\Delta T_s> \qquad (3.3)$$

where c_f is the specific heat and u is the vertical Darcian velocity. We find $<\Delta T_s> \approx 9$ °C over the five heat flow sites, which gives $\rho_f u = 5 \times 10^{-6}$ $kgm^{-2}s^{-1}$.

In addition, assuming the sediments are effectively impermeable (Spinelli *et al.* 2004), the conductive thermal gradient in the basaltic basement given by equation (3.A.2) can be used to estimate Rayleigh number, *Ra*, within the basement, which provides insight into whether the convection is supercritical. For a basement layer of thickness h_b, with a given basal heat flux, q_b,

from below, impermeable top and bottom boundaries and a fixed temperature at the top, buoyancy driven convection will occur provided *Ra* exceeds a critical value Ra_c (Nield, 1968).

$$Ra = \frac{\alpha g k q_b h_b^2}{\lambda_b a^* \nu} \geq Ra_c = 27.1 \tag{3.4}$$

Assuming other parameters are constant, equation (3.4) shows that *Ra* decreases as $\tau^{-1/2}$ as the crust ages. Using parameter values in Table 3.2, Figure 3.5 displays the crustal permeability needed to exceed Ra_c for h_b = 150 m and h_b = 550 m as a function of age. These values of h_b are chosen based on logging data from ODP hole 504B that indicates the upper 100-200 m of the crust is significantly more permeable than then underlying extrusive section, which extends to approximately 550 m beneath the sediments (Becker *et al.* 1989). The curves in Figure 3.5 show that supercritical convection at 1.6 Ma requires that *k* must exceed a threshold value $k_{th} = 3 \times 10^{-12}$ m^2 and 2×10^{-13} m^2, for h_b = 150 and 550 m, respectively; whereas k_{th} must exceed 7×10^{-12} m^2 and 5×10^{-13} m^2 at 6.9 Ma for the same values of h_b.

When $Ra >> Ra_c$ in a permeable layer with a given basal heat flux, vigorous convection tends to cool the layer. Scale analysis indicates that the ratio of the mean temperature difference across the convecting layer ΔT to the value $\Delta T_0 = q_b h_b / \lambda_b$ that would result from conduction is proportional to $Ra^{-1/2}$ (e.g., Lowell & Germanovich, 2004). Hence, to investigate the degree of cooling that may result from supercritical convection, we write

$$\frac{\Delta T}{\Delta T_0} \approx \left(\frac{Ra}{Ra_c} \right)^{-1/2} \tag{3.5}$$

where Ra_c is adopted as an approximate scaling factor. For example, Equation (3.5) shows that if $Ra = 100 Ra_c$, which corresponds to a bulk permeability $k = 100 k_{th}$, then $\Delta T \approx 0.1 \Delta T_0$. Assuming the sediment is impermeable, and ignoring the temperature differences associated with ascending and descending plumes, such vigorous convection would tend to homogenize the temperature distribution within the most of convecting layer, and the heat flux q_b would occur through a thin thermal boundary layer of thickness δ. That is, instead of $q_b = \lambda \Delta T_0 / h_b$, vigorous convection would yield $q_b = \lambda \Delta T / \delta$

$$q \gg h_b (Ra / Ra_c)^{-1/2} \tag{3.6}$$

Hence, the high *Ra* supercritical convection regime would not by itself result in a reduction in conductive heat flow across the sediment layer unless advection can occur through the sediment layer or some other process, such as outcrop to outcrop circulation or fluid discharge through faults also takes place. The main effect of supercritical convection is to lower and homogenize the temperature distribution within the basement.

In the following subsections, we present a detailed analysis of the heat flow data as a function of age from the five heat flow sites labeled PB02 through PB06. This analysis provides estimates of crustal permeability that can be compared with the Rayleigh criterion shown in Figure 3.5. The goal is to determine whether there appear to be significant changes in crustal permeability as a function of age that affects the advective heat transfer. In addition, we calculate the advective mass flux at each site to determine how it changes with crustal age. The values of permeability and mass flux are given in Table 3.3. We will show that the sealing age of ~ 5.7 Ma at the CRR is a function of both increasing sediment thickness and burial of basement exposure as well as changes in crustal permeability that limit supercritical Rayleigh number convection. In

performing these analyses, we neglect the effects of heat flow refraction, fluid flow through the sediments, and the effect of sedimentation on reducing the observed heat flow (e.g., Hutchinson, 1985; Hutnak & Fisher, 2007).

3.4.1 Heat Flow Site PB02

Site PB02, the closest heat flow station to the CRR, is located on ~ 1.6 Ma old oceanic basement where the mean sediment thickness is about 40 m. These 19 heat flow measurements (Table 3.1) have a mean of 41 mWm^{-2} whereas $q_b \approx 400$ mWm^{-2}. These values yield a mean heat flow deficit, $(1 - q_{obs}/q_b)$, of ≈ 0.9 thereby giving an advective heat flow $q_{adv} \approx 360$ mWm^{-2}. Using an average basement temperature of 2°C, the resulting mass flux $\rho_f u$ from equation (3.3) is ~ 4 x 10^{-5} $kgm^{-2}s^{-1}$.

Heat flow values observed at PB02 can be grouped broadly into two sets, A and B (Figure 3.6a). Set A shows uniformly low heat flow, whereas the set B has a southward increasing trend in heat flow suggesting lateral transport of heat by fluid advection (Figure 3.6a). The possible discharge could be at a sparsely sedimented basement exposure to the south. Recharge could be anywhere in the north as Figure 3.6b shows continuous thinly-sedimented basement. To estimate the lateral mass flow through the basement, we apply the well-mixed aquifer model of Langseth & Herman (1981) as outlined in the Appendix 3.B. Equation (3.B.4) enables us to estimate the quantity kh_b; and for h_b = 150 and 550 m, we obtain permeabilities of ~ 6 x 10^{-10} and 5 x 10^{-11} m^2, respectively. These values are similar to those in Figure 3.5 for $Ra \approx 100 Ra_c$.

For basement thicknesses of 150 and 550 m, ΔT_0 would be ≈ 30 °C and 110 °C, respectively. Using scale analysis from equation (3.5) and (3.6) ΔT would be ≈ 3 °C and 11 °C and δ would be ≈ 15 m and ≈ 55 m thick. Hence vigorous supercritical convection would cool the basement and outcrop to outcrop circulation would transport low temperature fluid laterally and advect heat to the seafloor.

3.4.2 Heat Flow Site PB03

This site, at a crustal age of 2.6 Ma, consists of 11 measurements (Table 3.1). The mean sediment thickness is ≈ 70m and mean observed heat flow is 58 mWm^{-2}. The conductive prediction, from equation (3.1a), is 310 mWm^{-2} yielding a mean heat flow deficit of about 0.82, and an advected heat flow $q_{adv} \approx 260$ mWm^{-2}. From equation (3.3), and average basement temperature of 5°C deduced from the heat flow data (Table 3.1) gives the mass flux, $\rho_f u \sim 1$ x10^{-5} $kgm^{-2}s^{-1}$.

All measurements at PB03, except one, exhibit a uniformly low heat flow. The highest heat flow value of 217 mWm^{-2} appears to occur close to a fault (Figure 3.7) that possibly serves as a discharge zone. Assuming isothermal upflow through the fault at a temperature T_{sp}, equation 3.C.2 shows that conductive heat flow is expected to decay as $1/x$, where x is the distance from the fault plane. From equation (3.C.2), with q_b = 217 mWm^{-2} and x = 100 m, we calculate the temperature of the upflow, T_{sp}, in the range of 20 to 35 °C, depending whether we assume the basalt or sediment thermal conductivity, respectively (Table 3.2). At site PB03, ΔT_0 = 23°C and 86°C for 150 m and 550 m thick basement. If $Ra = 10 Ra_c$, scale analysis gives $\Delta T \approx 7$°C or ≈ 27°C and corresponding values of $\delta \approx 50$ m and 175 m, respectively. The bulk permeability would then be $\approx 10 k_{th}$. From Figure 3.5, this implies $k \approx 4$ x 10^{-11} m^2 for h_b = 150 m or 2 x 10^{-12} m^2 for h_b = 550 m. The estimate of T_{sp} appears to be reasonably consistent with supercritical

convection throughout layer 2A and a bulk permeability of ≈ 2 x 10^{-12} m^2. Given the low estimate of basement temperature, these results suggest that the discharge fault transports most of the advective heat to the seafloor at this site.

3.4.3 Heat Flow Site PB04

Site PB04 consists of 15 measurements (Table 3.1) located on 3.5 Ma crust. The region is covered with sediments with thicknesses ranging from 20 m to 290 m. The measurements are distributed over three sediment ponds with an average heat flow of 42 mWm^{-2}. Equation (3.1a) yields predicted heat flow of 272 mWm^{-2}, indicating a deficit of about 0.85, or $q_{adv} \approx 230$ mWm^{-2}. Incorporating this value of q_{adv} with $<\Delta T_s> \approx 5°C$, equation (3.3) gives $\rho_f u, \approx 1 \times 10^{-5}$ $kgm^{-2}s^{-1}$.

The measurements at PB04 can be broadly grouped into two sets, C and D (Figure 3.8a). Set C consists of nine measurements in a sediment pond located between two large topographic highs. Heat flow values in set C have a mean value of 16 mWm^{-2} and display a slightly increasing trend to the south. We interpret these data to reflect outcrop to outcrop lateral heat transfer where recharge occurs at poorly sedimented basement high areas to the north of the pond and discharges through a thinly sedimented basement high to the south. Applying the well-mixed aquifer model as outlined in Appendix 3.B, the volumetric flow rate per unit length ≈ 115 m^2yr^{-1}. The estimated permeability is ~ 2 x 10^{-10} and 2 x 10^{-11} m^2 for h_b = 150 m and 550 m, respectively. These values are similar to those for $Ra \approx 100 Ra_c$ (Figure 3.5). Given $\Delta T_0 = 20°C$ and 75 °C, $\Delta T \approx 2°C$ and 7.5°C for 150 m and 550 m layer thickness, respectively. These results suggest that supercritical buoyancy-driven convection significantly homogenizes the temperature distribution and cools the basement. We note that there are two local high heat flow values of 50 mWm^{-2} and 31 mWm^{-2} between the presumed recharge and discharge outcrops. These locally higher values may result from heat redistribution due to subcritical convection driven by the local basement topography.

In set D, three measurements are of uniformly low heat flow and one which exhibits the highest heat flow of 322 mWm^{-2} at this site. This high heat flow appears to occur close to a fault (Figure 3.8b) which could serve as a discharge zone. We can use Appendix 3.C and the fault model methodology outlined in PB03. From equation (3.C.2), with q_b = 322 mWm^{-2}, we calculate T_{sp} to be in the range of 25 to 50 °C accounting for thermal conductivity changes between sediment and basement.

3.4.4 Heat Flow Site PB05

The 7 heat flow measurements at this site (Table 3.1) have a mean of 14 mWm^{-2}. The crustal age of 4.5 Ma corresponds to a predicted heat flow (equation (3.1a)) q_b = 241 mWm^{-2}, indicating a deficit of about 0.94. Thus q_{adv} ~ 230 mWm^{-2}. The average sediment thickness ≈ 120 m except above the very large basement mound (Figure 3.9b), where h_s ~ 9 to 70 m. Based on q_{adv} ~ 230 mWm^{-2} and average observed basement temperature of 2°C, equation (3.3) yields $\rho_f u$, ~ 3 x 10^{-5} $kgm^{-2}s^{-1}$.

Heat flow increases slightly toward the large thinly sedimented topographic high in the center (Figure 3.9), but the data are too sparse to use the aquifer model to estimate the heat flow and through the mound. The increase in measured heat flow values toward the basement high likely reflects fluid upflow within the basement high, but it is unclear whether heat is ultimately transported by conduction or advection through the thin sediment layer. Assuming $Ra = 100\ R_{ac}$ with ΔT_0 = 18 and 66 °C, for 150 and 550 m thick basement, ΔT = 1.8°C and 6.6°C, respectively.

The low basement temperature of 2°C is thus consistent with supercritical convection homogenizing the temperature distribution and cooling the basement at site PB05. From Figure 3.5, $k = 5 \times 10^{-10}$ m^2 and 3×10^{-11} m^2 for h_b = 150 m and 550 m, respectively.

3.4.5 Heat Flow Site PB06

As shown in Table 3.1, site PB06 consists of 15 measurements in 5.7 Ma crust, where the predicted heat flow is 214 mWm^{-2}. The mean observed heat flow is 235 mWm^{-2}, which is slightly greater than the predicted value. The sediment thickness averages 145 m, burying the entire basement. Figure 3.10 shows high heat flow values of 899 and 301 mWm^{-2}, and 276, 305 and 411 mWm^{-2} located above local basement highs and relatively low values at basement lows. The mean basement temperature, $<\Delta T_s> \approx 33$ °C, which is near the mean expected for that age crust and sediment thickness (Figure 3.4). The basement temperature is highly variable, suggesting that hydrothermal circulation in the basement has not significantly homogenized the basement temperature. This indicates that convection is subcritical or only slightly supercritical. To quantify this process, we consider upward and downward fluid flows to account for the differences in conductive heat flux from the expected value (Appendix 3.D). The results from equation (3.D.1) show, for example, that the highest heat flow value of 899 mWm^{-2} corresponds to an upflow velocity, u_{z^*}, of ~ 7.5×10^{-9} ms^{-1} for ΔT_s = 22 °C, whereas the lowest heat flow value of 90 mWm^{-2} indicates a downflow velocity, u_z, of 1×10^{-9} ms^{-1} for ΔT_s = 33 °C. Assuming that the upflow is driven by a lateral temperature difference ΔT^*, and using scale analysis, we estimate the permeability of the basement,

$$u_{z^*} \sim \frac{\alpha g k \Delta T^*}{\nu} \tag{3.7}$$

where, ΔT^* = 3°C is approximated by the difference between ΔT_s at the basement high and the basement low. Equation (3.7) gives $k \sim 3 \times 10^{-12}$ m^2; and upon substituting this value into equation (3.4), we obtain $Ra \sim 14$ and 100 for h_b = 150 and 550 m, respectively, indicating that the convection ranges from subcritical to $< 5Ra_c$.

The heat flow distribution at PB06 is similar to that around ODP Hole 504B, in that heat flow is correlated with basement topography. In contrast, however, basement temperatures near Hole 504B and Holes 677 and 678, which are separated by approximately 2 km, are nearly constant despite nearly 150 m difference in sediment thickness (Fisher *et al.* 1994; Davis *et al.* 2004). This suggests that relatively vigorous convection has homogenized the temperature regime in the upper crust at 6.9 Ma, and Davis *et al.* (2004) argue that the permeability of the upper 100 m of basaltic basement is ~ 10^{-9} m^2. The implications of the contrasting hydrothermal regimes at 5.7 and 6.9 Ma are discussed below.

3.5. Discussion and Conclusions

The 67 new conductive heat flow measurements collected on the southern flank of the CRR crust between 1.6 and ≈ 5.7 Ma, together with legacy data, provide important insights into types and patterns of hydrothermal circulation and advective heat loss from young crust. Comparison between the observed heat flow and the predicted half-space lithospheric cooling model yields a mean heat flow deficit of ≈ 70% that is attributed primarily to advective heat transport. Detailed analysis of each site, however, suggests that the magnitude of advective heat transfer (Table 3.3) is not a simple function of crustal age. These results provide new insights into hydrothermal

circulation mechanisms as conductive heat flow approaches the predicted heat flow curve as a function of age (Figure 3.1).

Our analysis indicates that between sites PB02 and PB05 super-critical Rayleigh convection tends to homogenize the basement temperature distribution and cool the basement; but outcrop-to-outcrop circulation (PB02 and PB04) and fluid flow through faults (PB03 and PB04), which are superimposed on the Rayleigh convection regime, act to advect heat to the ocean (Figure 3.3). At PB06, however, there is little evidence of advective discharge, and thermal convection in the basement is likely sub-critical, driven by differences in basement topography (Figure 3.3 and 3.10).

At each site, we used the mean calculated temperature at the sediment-basement interface together with the estimated advective heat loss to determine the mean mass flux to the ocean (Table 3.3). We also constructed relatively simple mathematical models and/or used scale analysis for each site to estimate the permeability of the upper crust. Table 3.3 lists the permeability and mass flux values for each site, along with estimated permeability for 6.9 Ma crust at ODP hole 504B. The mass fluxes fall in a narrow range between 9×10^{-6} and 3×10^{-5} $kgm^{-2}s^{-1}$. The results of mathematical modeling and scale analysis points to an order magnitude difference in permeability between the upper 150 m of layer 2A and that of the entire layer 2A, estimated to be 550 m thick (Table 3.3). Moreover, the results show that permeability does not decrease monotonically with age, as might be expected from water-rock reactions that tend to fill fracture and pore spaces.

It is noteworthy that the estimates of basement permeability are not a monotonic function of age. The permeability at site PB03 appears to be less than at adjacent sites that are both older and younger. In addition the permeability between 4.5 and 5.7 Ma decreases significantly. In addition, at Hole 504B at 6.9 Ma crust, packer measurements yield permeabilities in the range of 10^{-13} to 10^{-14} m^2 (Anderson & Zoback, 1982; Fisher *et al.* 1990). However, the near uniformity of basement temperature between Hole 504B and Holes 677, 678, despite large differences in sediment thickness, suggest vigorous convection in the upper crustal layer. Davis *et al.* (2004) suggest a regional scale permeability of ~ 10^{-9} m^2 in the upper 100 m. This transition from high to decreased permeabilites, between 4.5 to 5.7 Ma and a likely increase in permeability in the shallow crust at 6.9 Ma suggests that the evolution of crustal permeability may not be simply correlated with crustal age.

The variability in estimated crustal permeabilities is similar to the variability seen in tomographic models of seismic p-wave velocity in layer 2 of the ocean crust (Wilson *et al.* 2018). The upper oceanic crust older than about 5.7 Ma consistently shows a higher velocity that is interpreted to be a result of porosity reduction (Gregory *et al.* submitted. 2018). The crust younger than 5.7 Ma can be segmented into a number of zones characterized by a combination of basement roughness, seismic velocity of layer 2 and ages determined from reinterpretation of magnetic anomaly data (Wilson *et al.* 2018). The evidence shows that the magma supply has waxed and waned with time. Heat flow measurements PB02, PB03 fall into a zone which from the velocity tomography model shows an ocean crust with low velocity layer 2A which is arguably thinning with increasing age and a layer 2B that has a velocity ~0.8 km/s faster than at the current spreading ridge (Figure 3.3). *Wilson et al.* (2018) interpret this feature as crust generated magmatically which has subsequently aged and shows the expected increase in velocity due to alteration by reaction with hydrothermal fluids. This interpretation is consistent with the decreased estimates in permeability for these heat flow sites. Sites PB04 and PB05 are located in a zone where the p-wave velocities in layer 2B are comparable to the velocity seen in

crust at the present-day spreading axis. This zone is interpreted as formed at a magma starved spreading ridge with extension dominated by tectonic faulting. Again this interpretation is consistent with the increased permeabilities estimated at these heat-flow sites. Site PB06 sits within the transition to significantly faster layer 2A and 2B velocities which are interpreted as an earlier phase of magma-rich spreading as sampled by ODP 504B.

The models used to analyze the heat flow data along the seismic line from crustal ages of ≈1.6 to ≈ 5.7 Ma are simplified. In addition, the models all assume 2D flow parallel to the spreading direction, whereas enhanced permeability may be aligned parallel to the ridge (Fisher *et al.* 2008) outcrop to outcrop flow may be 3D (Winslow & Fisher, 2015; Winslow *et. al.*, 2016) and fault controlled flow may be both along and perpendicular to the plane of the fault (e.g., Johnson *et. al.*, 1993; Lowell, 2017). In addition the permeability values estimated for the various sites represent bulk averages. The estimated values obtained are large, indicating that the permeability is fracture controlled, and the actual flow paths may be both anisotropic and defined by a few major fractures rather than by Darcy flow as used here.

Figure 3.1b shows that heat flow at sites PB02 thru PB05 lie well below the predicted cooling curve but begins to climb towards the cooling curve at ≈ 4.5 Ma and essentially reaches the curve at 5.7 Ma. This result is in contrast with the global data set (Figure 3.1a) where a heat flow deficit is observed until ~ 65 ± 10 Ma. Stein & Stein (1994) argue that the coincidence of conductive heat flow with the predicted cooling curve suggests that hydrothermal circulation is weak as a result of decreasing crustal permeability rather than a result of increasing sediment thickness burying basement rock. Our study, where heat flow reaches the cooling curve at a much younger crustal age of ≈ 5.7 Ma, however, indicates that the alignment of heat flow with the predicted curve may be a function of original permeability at the time of formation or reduction of permeability, which may result from mineral precipitation as well as mode of crustal generation, as well as sediment accumulation. The permeabilities at PB03 and PB06 are similar; however, which indicates that sediment blanketing is more effective than changes in permeability in limiting advective discharge. The data at PB06 indicates that a decline in crustal permeability results in subcritical or weakly supercritical convection, driven largely by basement topography, and that the relatively thick, low permeability sediment cover over crust older than about 6.0 Ma inhibits advective heat transfer to the ocean. Near ODP Hole 504B, where upper crustal permeability appears to be high, the thick sediment cover still prevents hydrothermal fluid discharge (Figure 3.3). This is similar to the JDFR flank where thick sediment cover also inhibits advective heat loss from young crust (Davis *et al.* 1997; Davis *et. al.*, 1999; Spinelli & Fisher, 2004; Hutnak *et. al.*, 2006).

The results of studies at young crust thus suggest that permeability, sediment thickness, topographical structure and variations in tectonic and magmatic activities with age all affect hydrothermal circulation in the oceanic crust in a complex interconnected fashion that is more site specific than that can be constrained by global datasets and models simply as a function of age. Increased understanding of crustal evolution and hydrothermal circulation will come as individual spreading systems are analyzed that includes details of crustal creation, tectonic evolution, water rock reactions, sedimentation, and age.

Acknowledgments. This research was supported in part by NSF Grants OCE 1353114 and 1558797 to RPL and Grants NSF OCE 1353003 and 1558824, to RNH. The NERC OSCAR project grant NE/I027010/1 (Hobbs & Peirce 2015) underpinned this work. The authors would

like to thank the officers, crew, technicians and science party on board the RRS James Cook during cruises JC112, JC113 and JC114. The MCS data were processed using GNS Globe Claritas at Durham University. The swath bathymetry was cleaned and processed using QPS Fledermaus by Gavin Haughton from the National Oceanographic Centre and Emma Gregory from Durham University. Yang Li, Durham University, UK, provided the Monte Carlo Matlab code for calculation of uncertainties. The heat flow data have been placed on the IEDA data portal, doi: http://dx.doi.org/10.1594/IEDA/324068, seismic data are available on request through the British Oceanographic Data Center or author RWH.

3.6. References

Alt, J. C., 1995. Sulfur isotopic profile through the oceanic crust: Sulfur mobility and seawater-crustal sulfur exchange during hydrothermal alteration, *Geology*, **23**(7), 585-588.

Anderson, R. N., & Hobart, M. A., 1976. The relation between heat flow, sediment thickness, and age in the eastern Pacific, *J. Geophys. Res.*, **81**(17), 2968-2989.

Anderson, R. N., & Zoback, M. D., 1982. Permeability, underpressures, and convection in the oceanic crust near the Costa Rica Rift, eastern equatorial Pacific, *J. Geophys. Res.*, **87**(B4), 2860-2868.

Anderson, B. W., Coogan, L. A., & Gillis, K. M., 2012. The role of outcrop-to-outcrop fluid flow in off-axis oceanic hydrothermal systems under abyssal sedimentation conditions, *J. Geophys. Res.*, **117**(B5).

Baker, P. A., Stout, P. M., Kastner, M., & Elderfield, H., 1991. Large-scale lateral advection of seawater through oceanic crust in the central equatorial Pacific, *Earth Planet. Sci. Letters*, **105**(4), 522-533.

Becker, K., Sakai, H., Adamson, A. C., Alexandrovich, J., Alt, J. C., Anderson, R. N., ... & Ishizuka, H., 1989. Drilling deep into young oceanic crust, Hole 504B, Costa Rica Rift, *Rev. Geophy.*, **27**(1), 79-102.

Becker, K., & Davis, E. E., 2004. In situ determinations of the permeability of the igneous oceanic crust, *Hydrogeo. Oceanic Lithosphere*, 189-224. Edited by E. E. Davis and H. Elderfield, Cambridge Univ. Press, New York.

Carslaw, H. S., & Jaeger, J. C., 1959. Conduction of heat in solids, *Oxford: Clarendon Press*, 2nd ed.

Carlson, R. L., 2011. The effect of hydrothermal alteration on the seismic structure of the upper oceanic crust: Evidence from Holes 504B and 1256D, *Geochem. Geophy. Geosys.*, **12**(9).

Carlson, R. L., 2014. The effects of alteration and porosity on seismic velocities in oceanic basalts and diabases, *Geochem. Geophy. Geosys.*, **15**(12), 4589-4598.

Cherkaoui, A. S., Wilcock, W. S., Dunn, R. A., & Toomey, D. R., 2003. A numerical model of hydrothermal cooling and crustal accretion at a fast spreading mid-ocean ridge, *Geochem. Geophy. Geosys.*, **4**(9).

Craft, K. L., & Lowell, R. P., 2009. A boundary layer model for submarine hydrothermal heat flows at on-axis and near-axis regions, *Geochem. Geophy. Geosys.*, **10**(12).

Davies, J. H., & Davies, D. R., 2010. Earth's surface heat flux, *Solid Earth*, **1**(1), 5.

Davis, E. E., Fisher, A. T., Firth, J. V., Staff Scientist, L., Fox, P. J., Allan, J., ... & Home, O. D. P., 1997. Hydrothermal circulation in the oceanic crust: Eastern flank of the Juan de Fuca Ridge, In *Proc. ODP Initial Reports*, **168**, 1-470.

Davis, E. E., Chapman, D. S., Wang, K., Villinger, H., Fisher, A. T., Robinson, S. W., ... & Becker, K., 1999. Regional heat flow variations across the sedimented Juan de Fuca Ridge

eastern flank: Constraints on lithospheric cooling and lateral hydrothermal heat transport, *J. Geophys. Res.*, **104**(B8), 17675-17688.

Davis, E. E., Wang, K., Becker, K., Thomson, R. E., & Yashayaev, I., 2003. Deep-ocean temperature variations and implications for errors in seafloor heat flow determinations, *J. Geophys. Res.*, **108**(B1).

Davis, E. E., Becker, K., & He, J., 2004. Costa Rica Rift revisited: constraints on shallow and deep hydrothermal circulation in young oceanic crust, *Earth Planet. Sci. Letters*, **222**(3-4), 863-879.

Elder, J. W. (1965). Physical processes in geothermal areas, *Terrestrial heat flow, Geophysical Monograph Series*, 8, edited by W.H.K. Lee, p. 211-239, AGU, Washington, D.C.

Elderfield, H., & Schultz, A., 1996. Mid-ocean ridge hydrothermal fluxes and the chemical composition of the ocean, *Ann. Rev. Earth Planet. Sci.*, **24**(1), 191-224.

Embley, R. W., Hobart, M. A., Anderson, R. N., & Abbott, D., 1983. Anomalous heat flow in the northwest Atlantic: A case for continued hydrothermal circulation in 80-MY crust, *J. Geophys. Res.*, **88**(B2), 1067-1074.

Emile-Geay, J., & Madec, G., 2009. Geothermal heating, diapycnal mixing and the abyssal circulation, *Ocean Science*, **5**(2), 203-217.

Fisher, A. T., Becker, K., Narasimhan, I. T. N., Langseth, M. G., & Mottl, M. J., 1990. Passive, off-axis convection through the southern flank of the Costa Rica Rift, *J. Geophys. Res.*, **95**(B6), 9343-9370.

Fisher, A. T., Becker, K., & Narasimhan, T. N., 1994. Off-axis hydrothermal circulation: Parametric tests of a refined model of processes at Deep Sea Drilling Project/Ocean Drilling Program site 504, *J. Geophys. Res.*, **99**(B2), 3097-3121.

Fisher, A. T., 1998. Permeability within basaltic oceanic crust, *Rev. Geophy.*, **36**(2), 143-182.

Fisher, A. T., & Becker, K., 2000. Channelized fluid flow in oceanic crust reconciles heat-flow and permeability data, *Nature*, **403**(6765), 71-74.

Fisher, A. T., Davis, E. E., Hutnak, M., Spiess, V., Zühlsdorff, L., Cherkaoui, A., ... & Mottl, M. J., 2003. Hydrothermal recharge and discharge across 50 km guided by seamounts on a young ridge flank, *Nature*, **421**(6923), 618-621.

Fisher, A. T., Davis, E. E., and Becker, K., 2008, Borehole-to-borehole hydrologic response across 2.4 km in the upper oceanic crust: Implications for crustal-scale properties, *J. Geophys. Res.*, **113**, B07106.

Fisher, A. T., & Harris, R. N., 2010. Using seafloor heat flow as a tracer to map subseafloor fluid flow in the ocean crust, *Geofluids*, **10**(1-2), 142-160.

Gregory, E. P. M., Hobbs, R. W., Peirce, C., & Wilson, D. J., 2018. 2B or not 2B? – a terminology-independentproxy for characterisingthe extrusive-intrusive transition in magmatic oceanic crust, *Geochem. Geophy. Geosys.(submitted).*

Hasenclever, J., Theissen-Krah, S., Rüpke, L. H., Morgan, J. P., Iyer, K., Petersen, S., & Devey, C. W., 2014. Hybrid shallow on-axis and deep off-axis hydrothermal circulation at fast-spreading ridges, *Nature*, **508**(7497), 508-512.

Hasterok, D., 2013. A heat flow based cooling model for tectonic plates, *Earth Planet. Sci. Letters*, **361**, 34-43.

Heberling, C., Lowell, R. P., Liu, L., & Fisk, M. R., 2010. Extent of the microbial biosphere in the oceanic crust, *Geochem. Geophy. Geosys.*, **11**(8), Q08003.

Hobart, M. A., Langseth, M. G., & Anderson, R. N., 1985. A geothermal and geophysical survey on the south flank of the Costa Rica Rift: sites 504 and 505, *Initial Reports of the Deep Sea Drilling Project*, **83**(APR), 379-404.

Huber, J. A., Butterfield, D. A., & Baross, J. A., 2003. Bacterial diversity in a subseafloor habitat following a deep-sea volcanic eruption, *FEMS Microbiology Ecology*, **43**(3), 393-409.

Hutchison, I., 1985. The effects of sedimentation and compaction on oceanic heat flow, *Geophys. Jour. Inter.*, **82**(3), 439-459.

Hutnak, M., Fisher, A. T., Zühlsdorff, L., Spiess, V., Stauffer, P. H., & Gable, C. W., 2006. Hydrothermal recharge and discharge guided by basement outcrops on 0.7–3.6 Ma seafloor east of the Juan de Fuca Ridge: Observations and numerical models, *Geochem. Geophy. Geosys.*, **7**(7). Q7002.

Hutnak, M., & Fisher, A. T., 2007. Influence of sedimentation, local and regional hydrothermal circulation, and thermal rebound on measurements of seafloor heat flux, *J. Geophys. Res.*, , **112** (B12).

Hutnak, M., Fisher, A. T., Harris, R., Stein, C., Wang, K., Spinelli, G., ... & Silver, E., 2008. Large heat and fluid fluxes driven through mid-plate outcrops on ocean crust, *Nature Geoscience*, **1**(9), 611-614.

Jarrard, R. D., Abrams, L. J., Pockalny, R., Larson, R. L., & Hirono, T., 2003. Physical properties of upper oceanic crust: Ocean Drilling Program Hole 801C and the waning of hydrothermal circulation, *J. Geophys. Res.*, **108**(B4).

Johnson, H. P., Becker, K., & Von Herzen, R., 1993. Near-axis heat flow measurements on the northern Juan de Fuca Ridge: Implications for fluid circulation in oceanic crust, *Geophy. Res. Lett.*, **20**(17), 1875-1878.

Kolandaivelu, K. P., Harris, R. N., Lowell, R. P., Alhamad, A., Gregory, E. P., & Hobbs, R. W., 2017. Analysis of a conductive heat flow profile in the Ecuador Fracture Zone, *Earth Planet. Sci. Letters*, **467**, 120-127.

Langseth, M. G., & Von Herzen, R. P., 1970. Heat flow through the floor of the world oceans, *The sea*, **4**(part 1), 299-352.

Langseth, M. G., & Herman, B. M., 1981. Heat transfer in the oceanic crust of the Brazil Basin, *J. Geophys. Res.*, , **86**(B11), 10805-10819. 05

Langseth, M. G., Cann, J. R., Natland, J. H., & Hobart, M., 1983. Geothermal phenomenon at the Costa Rica Rift: background and objectives for drilling at Deep Seas Drilling Project sites 501, 504, and 505, *Initial reports of the Deep Sea Drilling Project*, **69**(MAY), 5-30.

Langseth, M. G., Mottl, M. J., Hobart, M. A., & Fisher, A., 1988. The distribution of geothermal and geochemical gradients near Site 501/504: implications for hydrothermal circulation in the oceanic crust, In *Proc. Ocean Drill. Program Initial Rep*, **111**, 23-32.

Langseth, M. G., Becker, K., Von Herzen, R. P., & Schultheiss, P., 1992. Heat and fluid flux through sediment on the western flank of the Mid-Atlantic Ridge: A hydrogeological study of North Pond, *Geophy. Res. Lett.*, **19**(5), 517-520.

Lister, C. R. B., 1972. On the thermal balance of a mid-ocean ridge, *Geophys. Jour. Inter.*, **26**(5), 515-535.

Lister, C. R. B., 1982. "Active" and "passive" hydrothermal systems in the oceanic crust: predicted physical conditions, *The dynamic environment of the ocean floor*, 441-470. ed. By K. Fanning and F.T. Manheim, D.C. Hearth, Lexington, MA.

Lowell, R. P., 1975. Circulation in fractures, hot springs, and convective heat transport on mid-ocean ridge crests, *Geophys. Jour. Inter.*, **40**(3), 351-365.

Lowell, R. P., & Germanovich, L. N., 2004. Hydrothermal processes at mid-ocean ridges: Results from scale analysis and single-pass models, *Mid-Ocean Ridges: Hydrothermal Interactions Between the Lithosphere and Oceans, Geophysical Monographic Series,* **148**, 219-244. ed. by C.R. German, J. Lin, and L.M. Parson, AGU, Washington, D. C.

Lowell, R. P., 2017. A fault-driven circulation model for the Lost City Hydrothermal Field, *Geophy. Res. Lett.*, **44**(6), 2703-2709.

Macdonald, K. C., 1982. Mid-ocean ridges: Fine scale tectonic, volcanic and hydrothermal processes within the plate boundary zone, *Ann. Rev. Earth Planet. Sci.*, **10**(1), 155-190.

Nield, D. A., 1968. Onset of thermohaline convection in a porous medium, *Water Resources Research*, **4**(3), 553-560.

Qiuming, C., 2016. Fractal density and singularity analysis of heat flow over ocean ridges, *Scientific reports,* **6**, 19167.

Sclater, J., Jaupart, C., & Galson, D., 1980. The heat flow through oceanic and continental crust and the heat loss of the Earth, *Rev. Geophy.*, **18**(1), 269-311.

Spinelli, G. A., & Fisher, A. T., 2004. Hydrothermal circulation within topographically rough basaltic basement on the Juan de Fuca Ridge flank. *Geochem. Geophy. Geosys.*, **5**(2).

Spinelli, G. A., & Harris, R. N., 2011. Effects of the legacy of axial cooling on partitioning of hydrothermal heat extraction from oceanic lithosphere, *J. Geophys. Res.,* **116**(B9), B09102.

Stein, C. A., & Stein, S., 1992. A model for the global variation in oceanic depth and heat flow with lithospheric age, *Nature*, **359**(6391), 123-129.

Stein, C. A., & Stein, S., 1994. Constraints on hydrothermal heat flux through the oceanic lithosphere from global heat flow, *J. Geophys. Res.*, **99**(B2), 3081-3095.

Stein, J. S., & Fisher, A. T., 2001. Multiple scales of hydrothermal circulation in Middle Valley, northern Juan de Fuca Ridge: Physical constraints and geologic models, *J. Geophys. Res.*, **106**(B5), 8563-8580.

Theissen-Krah, S., Iyer, K., Rüpke, L. H., & Morgan, J. P., 2011. Coupled mechanical and hydrothermal modeling of crustal accretion at intermediate to fast spreading ridges, *Earth Planet. Sci. Letters*, **311**(3-4), 275-286.

Villinger, H., & Davis, E. E., 1987. A new reduction algorithm for marine heat flow measurements, *J. Geophys. Res.*, **92**(B12), 12846-12856.

Von Herzen, R. P., 2004. Geothermal evidence for continuing hydrothermal circulation in older (> 60 Ma) ocean crust, *Hydrogeology of the Oceanic Lithosphere*, 414-450.

Wheat, C. G., Mottl, M. J., Fisher, A. T., Kadko, D., Davis, E. E., & Baker, E., 2004. Heat flow through a basaltic outcrop on a sedimented young ridge flank, *Geochem. Geophy. Geosys.*, **5**(12).

Williams, D. L., & Von Herzen, R. P., 1974. Heat loss from the Earth: new estimate, *Geology*, **2**(7), 327-328.

Wilson, D. S., & Hey, R. N., 1995. History of rift propagation and magnetization intensity for the Cocos-Nazca sspreading Center, *J. Geophys. Res.*, **100**(B6), 10041-10056.

Wilson, D.S., D. A. H. Teagle, G. D. Acton, et al., 2003. *Proc. ODP, Init. Repts., 206:* College Station, TX (Ocean Drilling Program).

Wilson, Dean, Richard Hobbs, Christine Peirce, Emma Gregory, and Adam Robinson. "Intermediate oceanic crust is created by alternating periods of magma-rich and magma-poor spreading: evidence from a 7 Myr transect from the Costa Rica Ridge to ODP borehole 504B." In EGU General Assembly Conference Abstracts, vol. 20, p. 15604. 2018.

Winslow, D. M., & Fisher, A. T., 2015. Sustainability and dynamics of outcrop-to-outcrop hydrothermal circulation, *Nature communications*, **6**, 7567.

Winslow, D. M., Fisher, A. T., Stauffer, P. H., Gable, C. W., & Zyvoloski, G. A., 2016. Three-dimensional modeling of outcrop-to-outcrop hydrothermal circulation on the eastern flank of the Juan de Fuca Ridge, *J. Geophys. Res.,* **121**(3), 1365-1382.

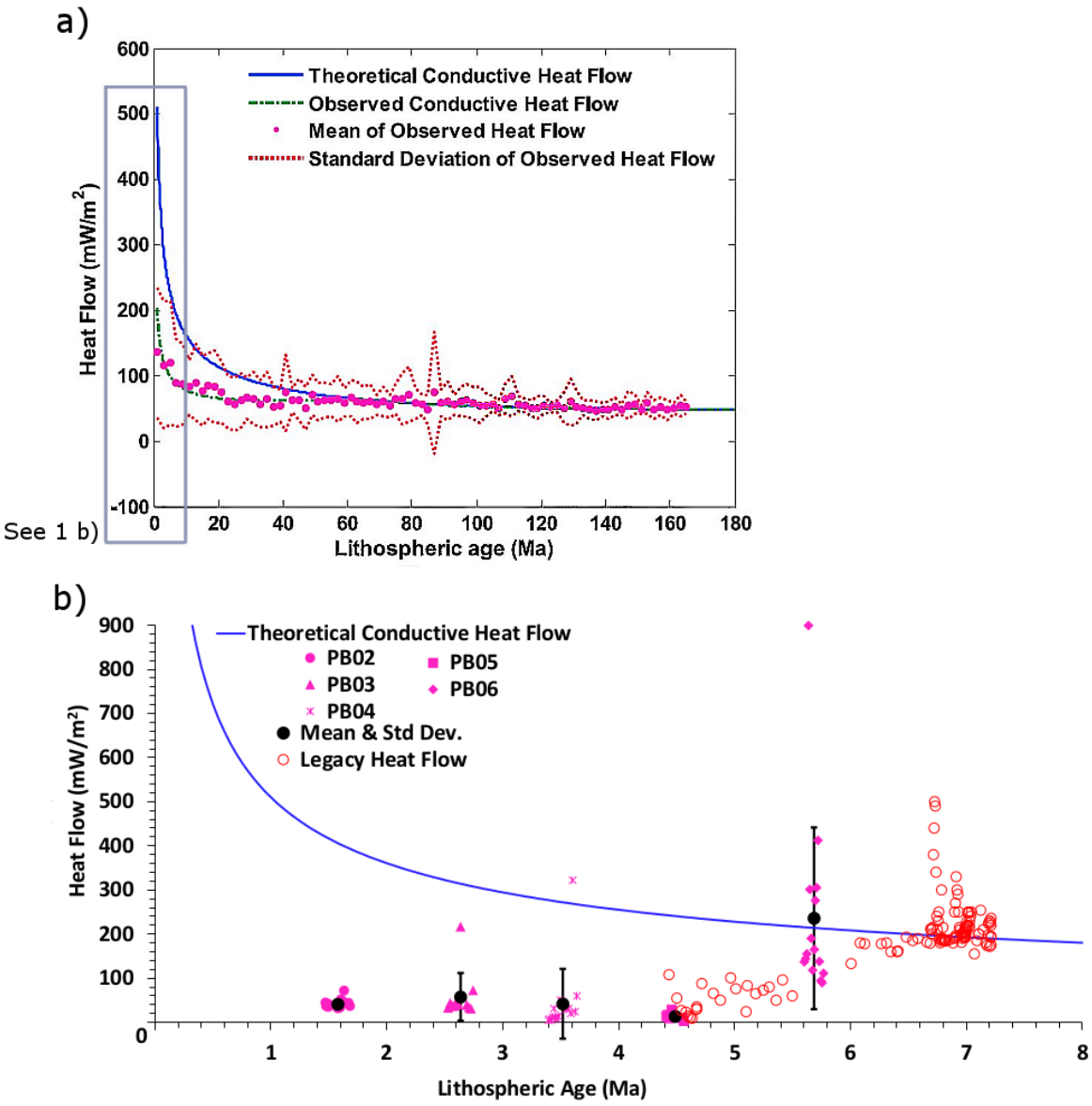

Figure 3.1. a) Conductive heat loss as a function of oceanic lithospheric age. Blue line shows predicted fit using equations 1a and 1b. The pink dots are observed data averaged in 2 Ma bins; red dotted lines show standard deviation; green dotted-dashed line show fit to the binned data (from *Heberling et al.* 2010). b) Heat flow on the south flank of the Costa Rica Rift as a function of lithospheric age. Blue line shows predicted fit/conductive cooling curve from equations 1a and 1b. . Solid pink shapes are are 67 new heat flow measurements divided into five sites in this study along with their mean and standard deviation in black. Red open circles show legacy heat flow data (*Anderson and Hobart*, 1976; *Langseth et al.* 1983, 1988; *Hobart et al.* 1985; *Davis et al.* 2003, 2004).

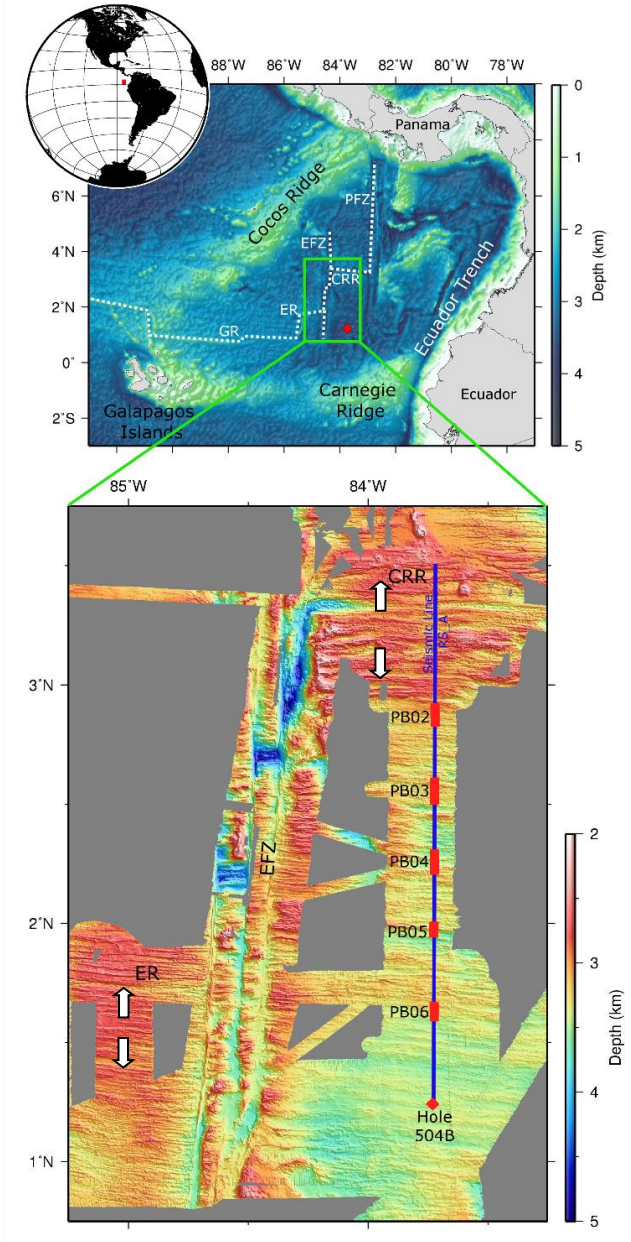

Figure 3.2. The globe points to the location of the Panama Basin. The top panel shows the map of the Panama Basin. The basin is bounded by the Cocos Ridge to the N and W, the Carnegie Ridge to the S, and the Ecuador Trench and Americas to the E. The dashed white lines show the spreading axis (CRR = Costa Rica Rift; ER = Ecuador Ridge; GR = Galapagos Spreading Center). The transforms bounding the CRR, EFZ = Ecuador Fracture Zone; PFZ = Panama Fracture Zone, are labeled. Red diamond shows the location of the ODP Hole 504B. The green box encloses the area where geophysical measurements were made during cruises JC112, JC113 and Sonne 0238.The bottom panel shows a zoom in of the green box with the spreading direction of the rifts shown in white arrows. RS_A seismic profile spanning from ODP Hole 504B to CRR is shown in the blue line. Stations PB02 to PB05 on RS_A is shown as red solid rectangles.

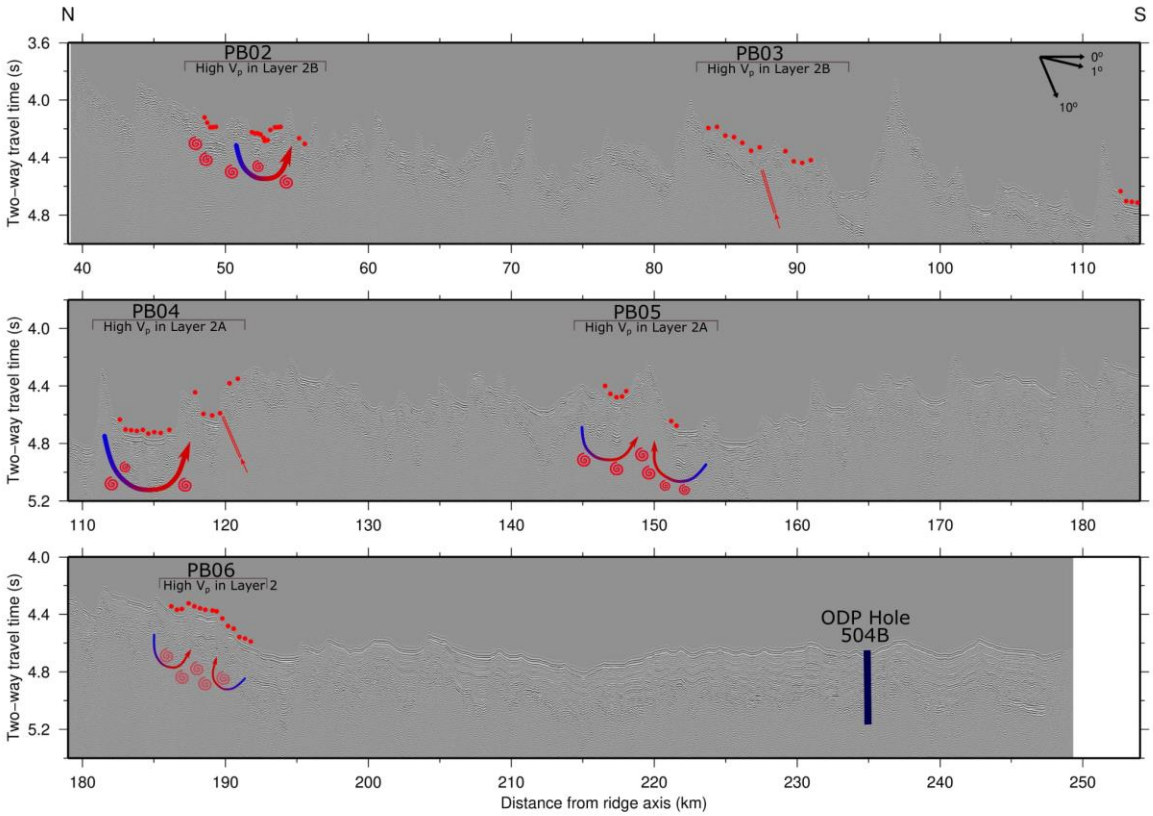

Figure 3.3. The pre-stack time migrated seismic image of PB02 with the vertical axis is two-way travel time and horizontal axis is the distance from the CRR in km. Heat flow stations PB02 thru PB06 and their various heat transport mechanisms are shown. The arrows indicate outcrop to outcrop type circulations except at PB06 where it indicates heat flow focused around buried basement highs. The red spirals from PB02 thru PB05 indicate supercritical convection cells that homogenize basement temperatures. The light red spirals in PB06 indicate sub to slightly super critical convection which redistributes heat. The red parallel lines and arrows in PB03 and PB04 indicate upflow of fluids through a fault. N=North and S=South.

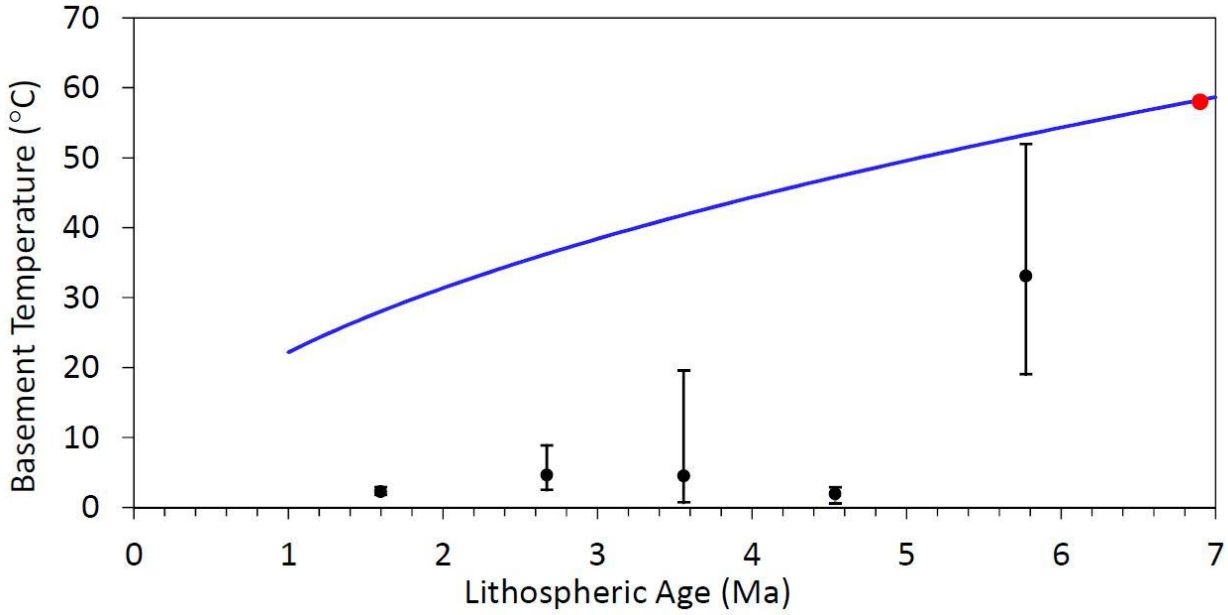

Figure 3.4. Plot showing basement temperature (°C) as a function of age (Ma). Expected basement temperature versus age is shown in the blue as obtained from Equation 3.2. The black dots show the average basement temperature (Table 3.1) relative to seawater from observed heat flow data for all five sites and the bars indicate their maximum and minimum range values. Observed basement temperature at 6.9 Ma crust in ODP Hole 504B (Becker et. al., 1983) is shown in the red dot.

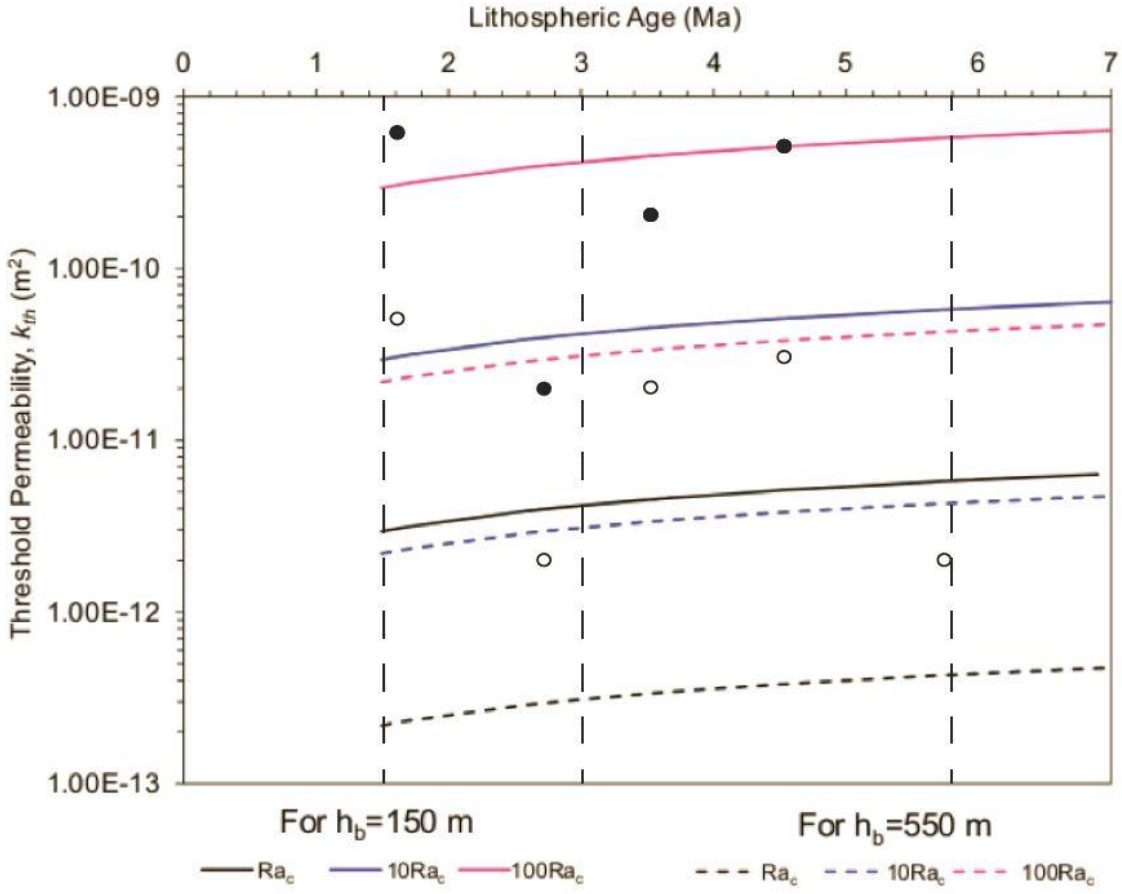

Figure 3.5. Plot showing estimated threshold permeability, k_{th}, of the crust (m^2) as a function of age (Ma) for Ra$_c$, 10 Ra$_c$, 100Ra$_c$ for h_b=150 m and 550 m. Solid circles are the estimated permeabilities at each site for h_b=150 m and open circles are for h_b=550 m. The permeability values calculated are given to one significant figure and have a likely uncertainty of a factor of 2.

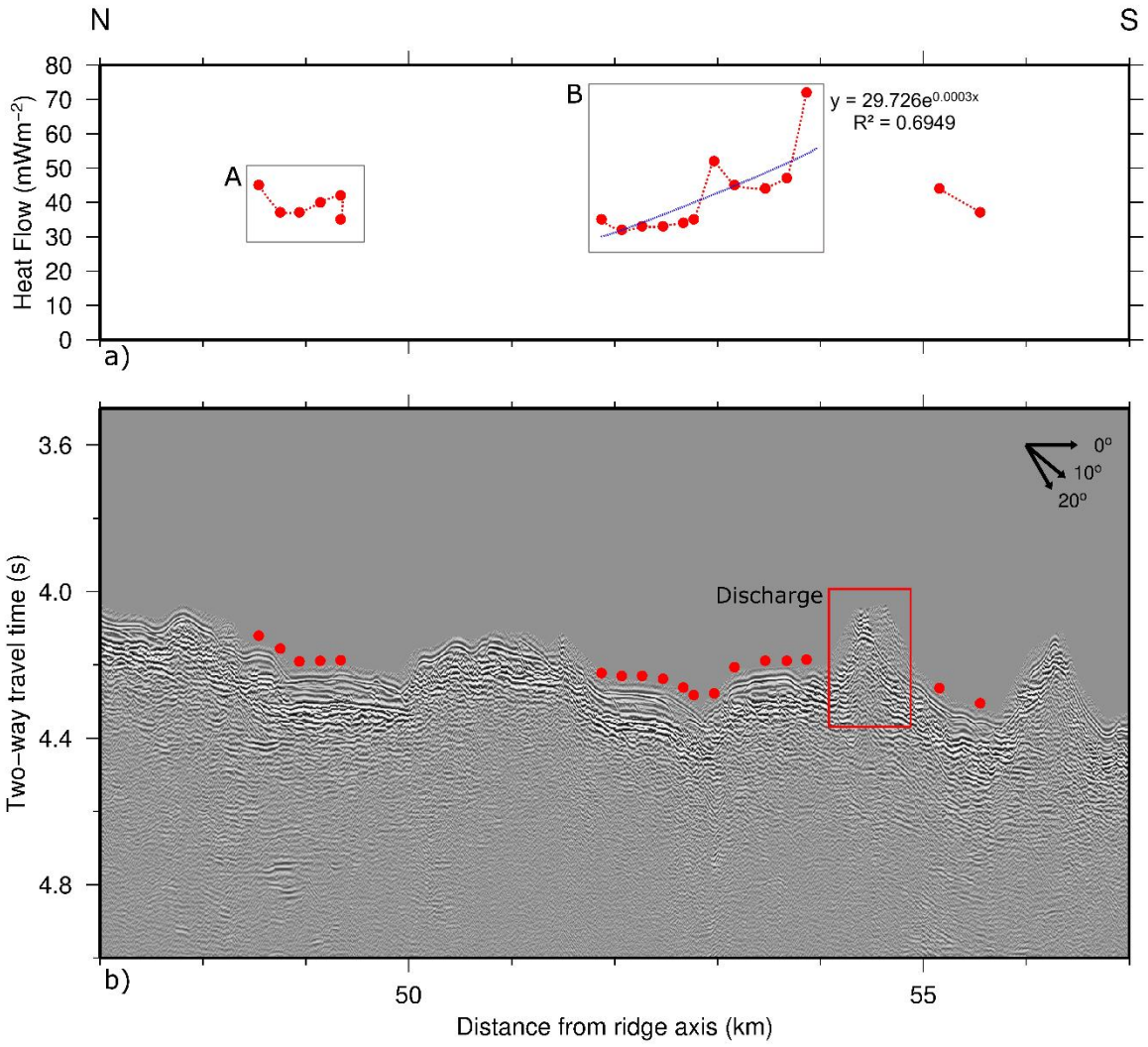

Figure 3.6. Site PB02 a) 19 heat flow measurements (red circles) as a function of distance from the Costa Rica Ridge axis. Grey boxes indicate heat flow sets A and B. Blue dashed line shows best fitting exponential function (refer equation B.2) which is the solution to equation B.1. R^2 shows the goodness of fit of the exponential equation. b) The pre-stack time migrated seismic image of PB02. The vertical axis is two-way travel time and horizontal axis is the distance from the CRR in km. Red box indicates possible discharge area. N=North and S=South.

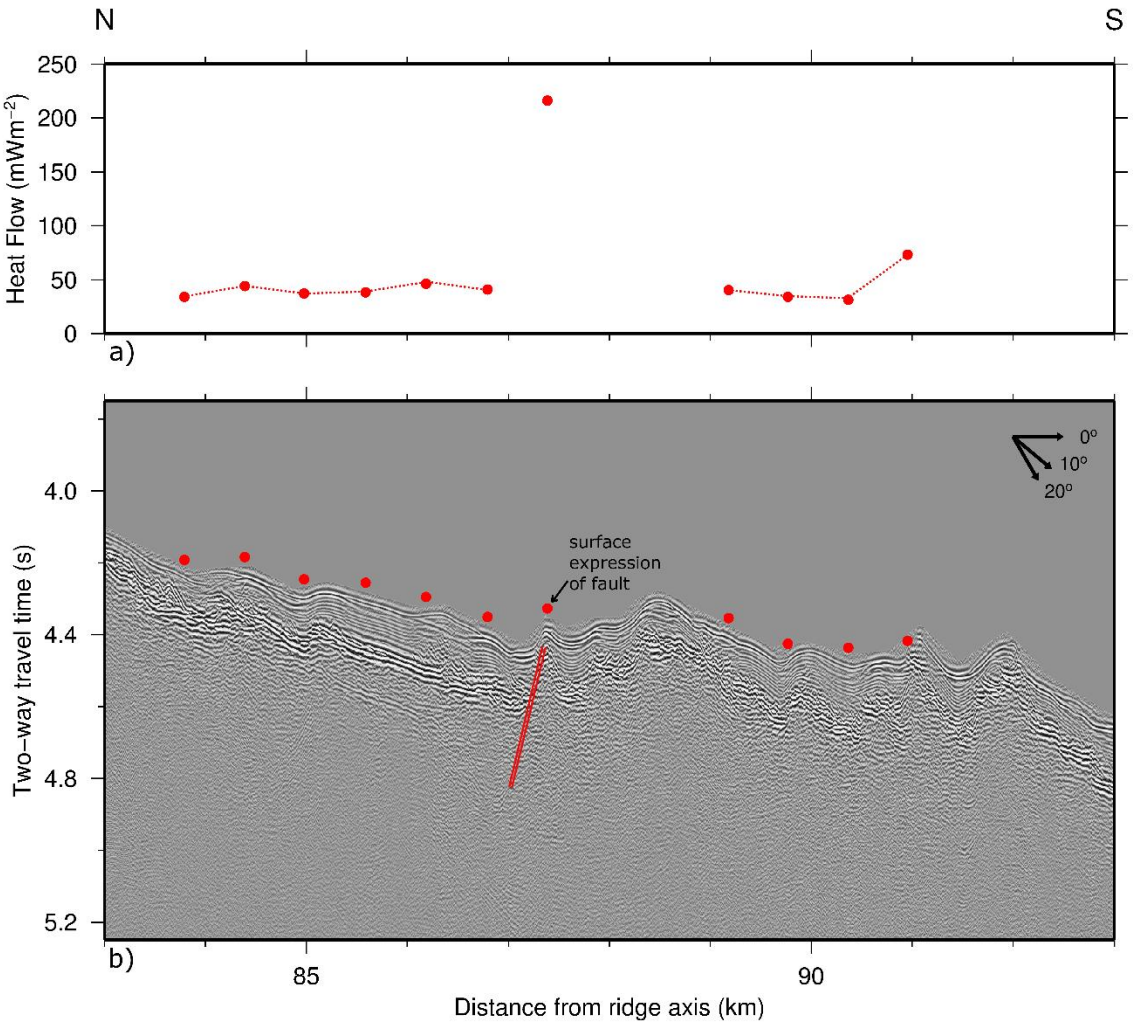

Figure 3.7. Site PB03 a) 11 heat flow measurements (red circles) as a function of distance from the Costa Rica Ridge axis. b) The pre-stack time migrated seismic image of PB03 where vertical axis is two-way travel time and horizontal axis is the distance from the CRR in km. Red parallel lines indicate possible fault location and black arrow points at surface expression of possible fault. N=North and S=South.

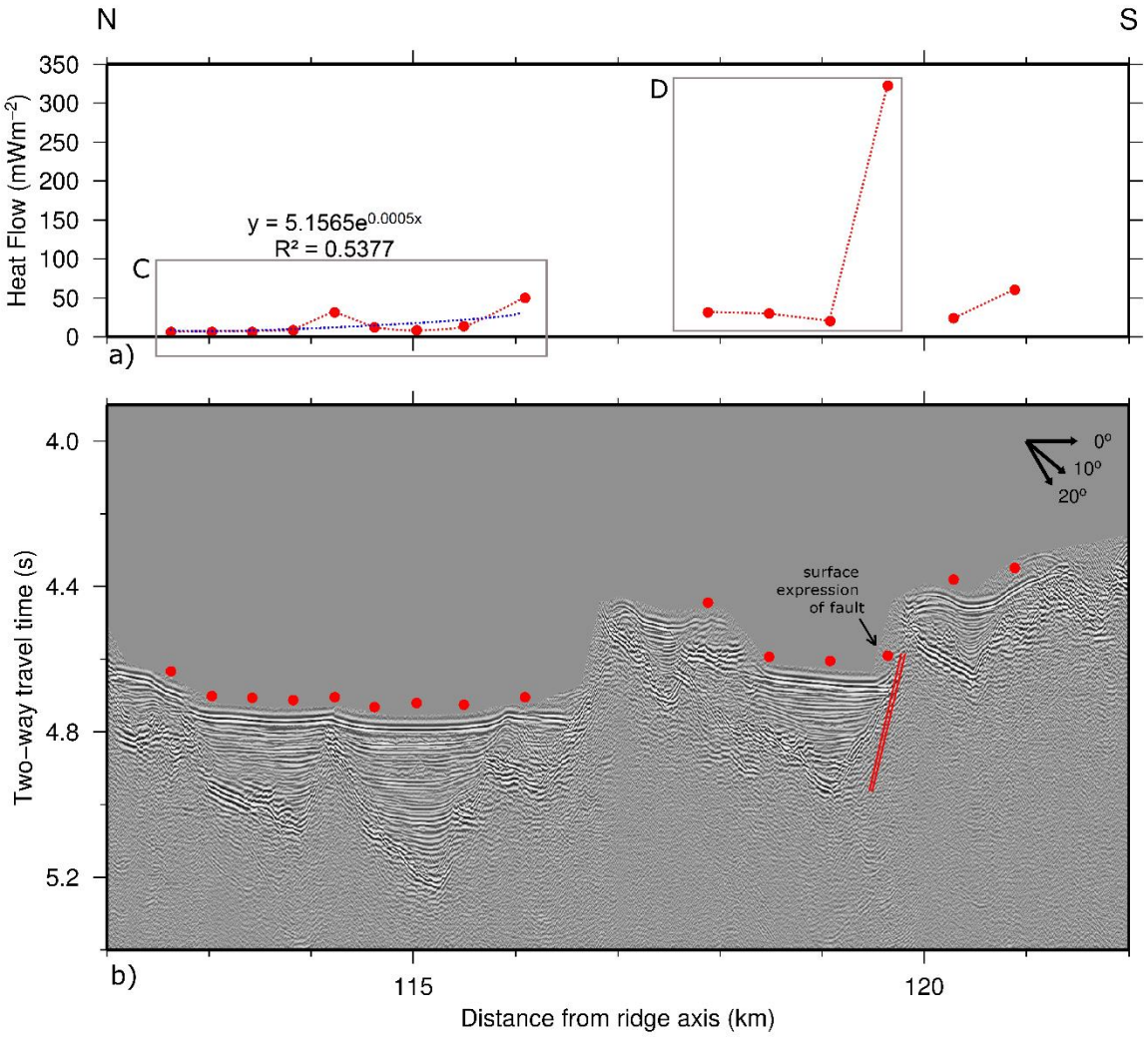

Figure 3.8. Site PB04 a) 15 heat flow measurements (red circles) as a function of distance from the Costa Rica Ridge axis. Grey boxes indicate sets C and D. Blue dashed line shows best fitting exponential function (refer equation 3.B.2) which is the solution to equation 3.B.1. R^2 shows the goodness of fit of the exponential equation. b) The pre-stack time migrated seismic image of PB04 where the vertical axis is two-way travel time and horizontal axis is the distance from the CRR in km. Red parallel lines indicate possible fault location and black arrow points at surface expression of possible fault. N=North and S=South.

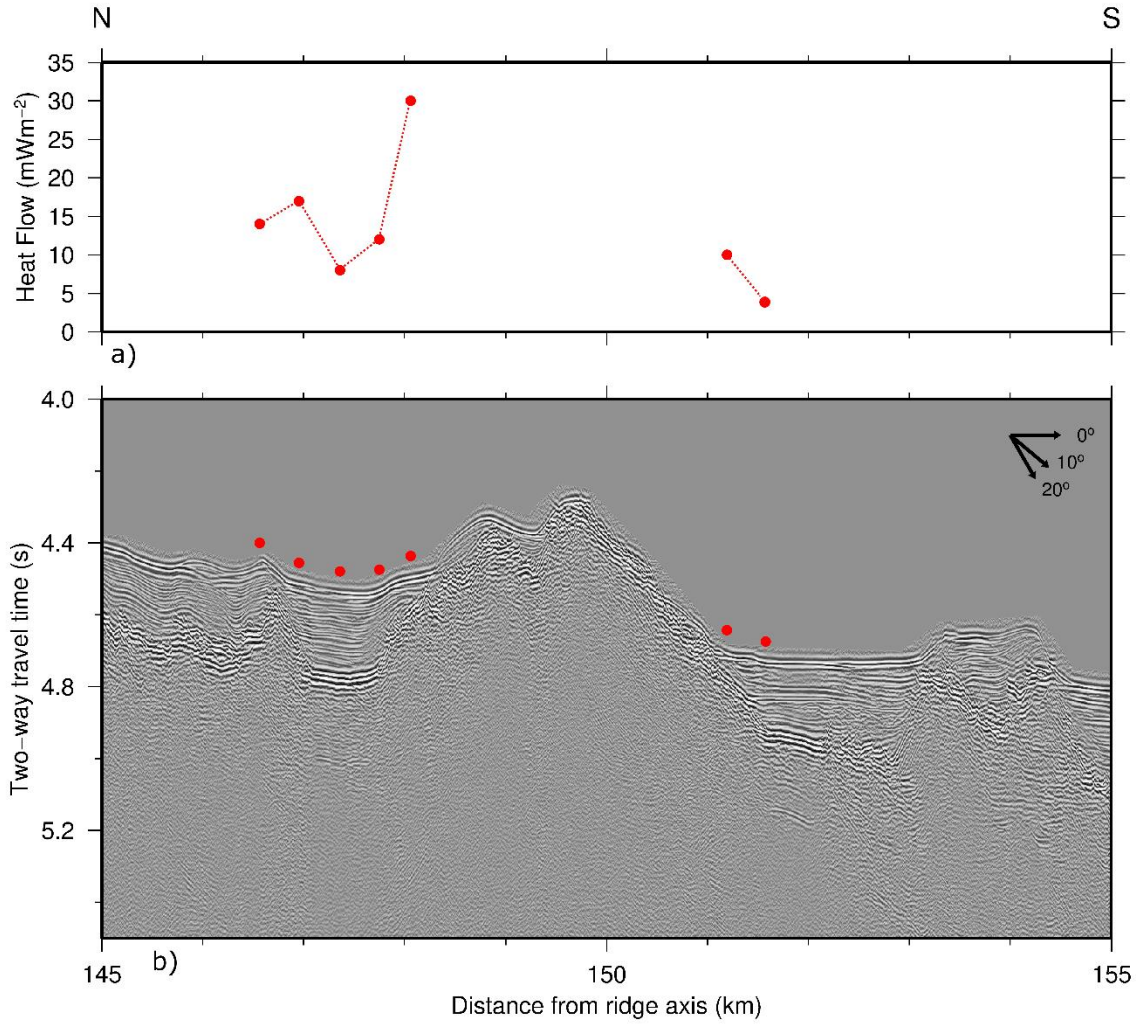

Figure 3.9. Site PB05 a) 7 heat flow measurements (red circles) as a function of distance from the Costa Rica Ridge axis. b) The pre-stack time migrated seismic image of PB05 wherethe vertical axis is two-way travel time and horizontal axis is the distance from the CRR in km. N=North and S=South.

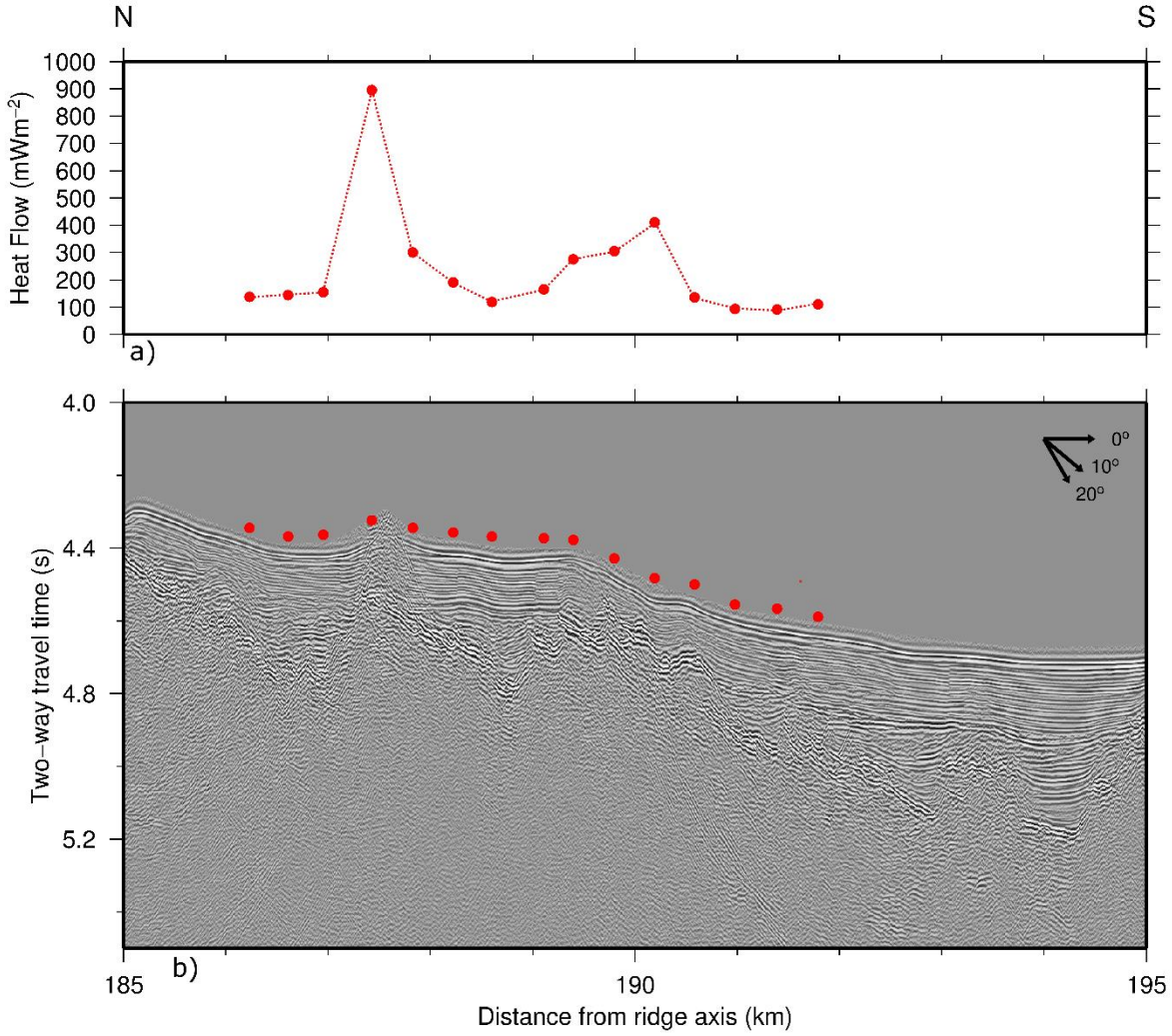

Figure 3.10. Site PB06 a) 15 heat flow measurements (red circles) as a function of distance from the Costa Rica Ridge axis. b) The pre-stack time migrated seismic image of PB06 where the vertical axis is two-way travel time and horizontal axis is the distance from the CRR in km. N=North and S=South.

Table 3.1. Conductive Heat Flow data from southern ridge flank of the Costa Rica Rift

Datum	Latitude	Longitude	Sediment Thickness	Thermal Gradient	Thermal Conductivity	Heat Flow	Basement Temperature
PB02 Age = 1.6 Ma	(°N)	(°W)	(m)	(°C km^{-1})	(W m^{-1} K^{-1})	(mWm^{-2})	(°C)
PB02-01	2.8897	-83.6991	41	62	0.7	45	2.53
PB02-02	2.8878	-83.6992	40	51	0.7	37	2.04
PB02-03	2.8861	-83.6993	49	52	0.7	37	2.59
PB02-04	2.8843	-83.6993	50	55	0.7	40	2.77
PB02-05	2.8825	-83.6993	50	59	0.7	42	2.93
PB02-06	2.8825	-83.6994	50	48	0.7	35	2.38
PB02-07	2.8596	-83.6998	45	48	0.7	35	2.15
PB02-08	2.8578	-83.6999	49	45	0.7	32	2.20
PB02-09	2.8560	-83.6999	51	45	0.7	33	2.30
PB02-10	2.8542	-83.6999	49	46	0.7	33	2.24
PB02-11	2.8524	-83.7000	49	47	0.7	34	2.29
PB02-12	2.8515	-83.7001	42	48	0.7	35	2.04
PB02-13	2.8497	-83.7001	27	73	0.7	52	1.99
PB02-14	2.8479	-83.7002	36	62	0.7	45	2.23
PB02-15	2.8452	-83.7003	44	60	0.7	44	2.64
PB02-16	2.8433	-83.7003	31	65	0.7	47	2.03
PB02-17	2.8416	-83.7004	21	97	0.7	72	2.02
PB02-18	2.8299	-83.7008	30	61	0.7	44	1.82
PB02-19	2.8263	-83.7008	42	52	0.7	37	2.16
PB03 Age = 2.6 Ma		Mean	42			41	2.28
PB03-01	2.5711	-83.7074	57	46	0.7	34	2.61
PB03-02	2.5657	-83.7075	66	61	0.7	44	4.00
PB03-03	2.5604	-83.7076	72	53	0.7	37	3.82
PB03-04	2.5549	-83.7078	86	53	0.7	38	4.58
PB03-05	2.5495	-83.7079	104	65	0.7	46	6.76
PB03-06	2.5440	-83.7080	87	58	0.7	41	5.06
PB03-07	2.5386	-83.7083	32	278	0.8	216	8.90
PB03-08	2.5224	-83.7087	46	55	0.7	40	2.55
PB03-09	2.5171	-83.7089	66	48	0.7	34	3.15
PB03-10	2.5117	-83.7090	108	44	0.7	31	4.75
PB03-11	2.5064	-83.7091	47	103	0.7	73	4.86
PB04 Age = 3.5 Ma		Mean	70			58	4.64
PB04-01	2.3105	-83.7124	93	9	0.7	6	0.74
PB04-02	2.3069	-83.7125	135	9	0.7	6	1.22
PB04-03	2.3033	-83.7126	159	8	0.8	6	1.27
PB04-04	2.2997	-83.7126	202	11	0.7	8	3.23
PB04-05	2.2960	-83.7126	34	44	0.7	31	1.51
PB04-06	2.2925	-83.7127	218	18	0.7	12	3.93
PB04-07	2.2888	-83.7127	318	12	0.7	8	3.82
PB04-08	2.2846	-83.7127	194	19	0.7	13	3.89
PB04-09	2.2792	-83.7126	113	71	0.7	50	8.01

PB04-10	2.2630	-83.7125	53	43	0.7	31	2.27
PB04-11	2.2576	-83.7124	110	44	0.7	30	4.86
PB04-12	2.2522	-83.7126	225	29	0.7	20	6.29
PB04-13	2.2471	-83.7126	45	437	0.7	322	19.58
PB04-14	2.2413	-83.7126	123	34	0.7	24	4.19
PB04-15	2.2359	-83.7126	33	83	0.7	60	2.72
PB05 Age = 4.5 Ma		Mean	137			42	4.50
PB05-01	2.0038	-83.7187	110	19	0.7	14	2.19
PB05-02	2.0003	-83.7188	126	23	0.7	17	2.89
PB05-03	1.9966	-83.7189	184	12	0.7	8	2.39
PB05-04	1.9931	-83.7191	163	17	0.7	12	2.61
PB05-05	1.9903	-83.7186	62	42	0.7	30	2.46
PB05-06	1.9620	-83.7194	45	14	0.7	10	0.63
PB05-07	1.9585	-83.7197	146	5	2.0	10	0.59
PB06 Age = 5.7 Ma		Mean	119			13	1.97
PB06-01	1.6453	-83.7409	140	188	0.7	137	26.18
PB06-02	1.6419	-83.7405	176	198	0.7	144	34.85
PB06-03	1.6388	-83.7404	135	210	0.7	155	28.39
PB06-04	1.6345	-83.7397	19	1157	0.8	896	22.21
PB06-05	1.6309	-83.7393	48	397	0.8	301	19.06
PB06-06	1.6273	-83.7391	146	259	0.7	190	37.92
PB06-07	1.6239	-83.7388	226	161	0.7	118	36.45
PB06-08	1.6193	-83.7388	168	229	0.7	165	38.47
PB06-09	1.6167	-83.7387	136	382	0.7	276	51.95
PB06-10	1.6131	-83.7381	82	418	0.7	305	34.44
PB06-11	1.6095	-83.7377	89	570	0.7	411	50.62
PB06-12	1.6060	-83.7373	104	190	0.7	135	20.18
PB06-13	1.6024	-83.7368	203	130	0.7	94	26.42
PB06-14	1.5987	-83.7365	261	125	0.7	90	32.60
PB06-15	1.5951	-83.7361	235	156	0.7	111	36.69
		Mean	145			235	33.09
					Average	≈85	≈9

Table 3.2. Parameters and Values

Symbol	Definition	Value	Units
a^*	Thermal diffusivity of fluid		$m^2\ s^{-1}$
c_f	Specific heat of water	4200	$J\ kg^{-1}\ K^{-1}$
g	Acceleration due to gravity	9.81	$m\ s^{-2}$
h_b	Basement thickness		m
h_s	Sediment thickness		m
k	Crustal permeability		m^2
k_{th}	Threshold crustal permeability		m^2
L	Horizontal fluid flow path length		m
q_{adv}	Advective heat flow		mWm^{-2}
q_b	Basal heat flux		mWm^{-2}
q_d	Heat flow at the discharge		mWm^{-2}
q_{obs}	Observed/Measured heat flow		mWm^{-2}
Ra	Rayleigh number		
Ra_c	Critical Rayleigh number		
T_b	Basement temperature		°C
T_d	Discharge temperature		°C
T_{sp}	Spring temperature; Temperature of the upwelling fluids from a fault		°C
T_{sw}	Seawater temperature	0	°C
u	Darcian velocity of fluid		$m\ yr^{-1}$
u_z	Downflow velocity of fluids		$m\ yr^{-1}$
u_{z^*}	Upflow velocity of fluids		$m\ yr^{-1}$
v_s	Sedimentation rate	40	mMa^{-1}
α	Thermal expansion coefficient of water	10^{-4}	$°C^{-1}$
δ	Thermal boundary layer thickness		m
λ_b	Thermal conductivity of the basement	2	$Wm^{-1}K^{-1}$
λ_s	Thermal conductivity of the sediments	0.92	$Wm^{-1}K^{-1}$
ν	Kinematic viscosity of the fluid	10^{-6}	$m^2\ s^{-1}$
ρ_f	Density of water	1000	$kg\ m^{-3}$
τ	Age of Oceanic crust		Ma

ΔT	Temperature difference in the convecting layer, under assumption that basement is homogenized, based on q_{obs}		°C
ΔT_{rd}	Temperature difference between recharge and discharge		°C
ΔT_s	Conduction-derived temperature at sediment-basement interface ("basement temperature")		°C
ΔT_0	Temperature difference that would result from conduction of q_b		°C
ΔT^*	Lateral temperature difference		°C

Table 3.3. Mass fluxes and permeabilities of sites PB02 thru 06 and ODP Hole 504B

Site	Age (Ma)	Fractional Heat Flow (q_{obs}/q_b)	Advective Heat Flux (mW m^{-2})	<ΔTs> (°C)	Mass Flux ($kgm^{-2}s^{-1}$)	Permeability (m^2)
PB02	1.6	0.10	360	3	4×10^{-5}	6×10^{-10} (upper 150 m) 5×10^{-11} (550 m)
PB03	2.7	0.18	260	7	10^{-5}	2×10^{-11} (upper 150 m) 2×10^{-12} (550 m)
PB04	3.5	0.15	230	6	10^{-5}	2×10^{-10} (upper 150 m) 2×10^{-11} (550 m)
PB05	4.5	0.06	230	1.6	3×10^{-5}	5×10^{-10} (upper 150 m) 3×10^{-11} (550m)
PB06	5.7	1.00	0	38	--	2×10^{-12} (550 m)
Hole 504B*	6.9					10^{-9} (upper 100m) 10^{-13} to 10^{-14} (lower part of layer 2A)

*(*Anderson & Zoback,* 1982; *Fisher et. al.,* 1990; *Davis et al.* 2004)

Appendix 3.A: 1-D Thermal Conduction Model

To estimate the expected temperature at the sediment-basement interface, we construct a 1-D steady state layered thermal conduction model consisting of a uniform layer of sediment overlying basaltic basement. We assume that thermal conductivity of each layer is constant, implying that,

$$\frac{d^2T}{dz^2} = 0 \quad . \tag{3.A.1}$$

where T is temperature and z is depth, subject to the conditions:

$$T_s(\mathrm{z}=0) = T_{sw}$$

$$\lambda_b \left.\frac{dT_b}{dz}\right|_{z=h_b} = q_b \quad . \tag{3.A.2}$$

Definitions and values of symbols are given in Table 3.2. Temperature and heat flux are continuous across the sediment –basement interface. Consequently, in the sediment layer,

$$T_s(\mathrm{z}) = T_{sw} + \frac{q_b}{\lambda_s}\mathrm{z};\ \ 0 \le z \le h_s \tag{3.A.3}$$

and the temperature at the sediment basement interface, relative to T_{sw} is

$$\Delta T_s(h_s) = \frac{q_b h_s}{\lambda_s} \tag{3.A.4}$$

Applying the half space cooling model in equation (3.1a) and assuming a constant sedimentation rate $h_s = v_s\tau$, we derive equation (3.2).

Similarly for the basement, the temperature distribution can be written

$$T_b(\mathrm{z}) = \Delta T_s + \frac{q_b z}{\lambda_b};\ \ h_s \le z \le h_b \tag{3.A.5}$$

Hence the temperature difference across the basement layer in the absence of convection is

$$\mathrm{D}T_0 = \frac{q_b h_b}{l_b} \tag{3.A.6}$$

This temperature difference is used in the Rayleigh number to determine whether buoyancy driven convection may occur in the basaltic basement. This temperature difference decreases as $\tau^{-1/2}$ as the crust ages, and hence the permeability needed for convection to occur increases as $\tau^{1/2}$.

Appendix 3.B: The Well-Mixed Aquifer Model

To estimate the lateral mass flow through the basement, we apply the well-mixed aquifer model of Langseth and Herman (1981) (Figure 3.B1), where lateral advection dominates heat transport by conduction. The steady state thermal balance is expressed as,

$$\rho_f c_f u h_b \frac{dT(\mathrm{x})}{dx} = q_b - \lambda_s \frac{T(x)}{h_s} \tag{3.B.1}$$

The exponential solution to this equation by applying boundary conditions $T = T_0$ at $x = x_0$ yields (Kolandaivelu et al. 2017),

$$\frac{q(x)}{q_b} = 1 + \left(\frac{q(x_0)}{q_b} - 1\right)\left[e^{\frac{a^*}{uh_a l}(x_0 - x)}\right] \tag{3.B.2}$$

For parameters shown in this appendix, refer to Table 3.2. Here $a^* = \lambda s/\rho_f c_f$; $q(x)$ is heat flow at distance of x from x_0; $q(x_0)$ is the heat flow at distance x_0; x_0 is the distance of the first heat flow measurement from the recharge outcrop (Table 3.1). An exponential fit based on the observed data and equating it to exponential in equation (3.B.2) provides the volumetric flow rate per unit length perpendicular to the flow direction, uh_b for a sediment thickness, h_s. Extrapolating the exponential fit to the data to the presumed discharge location from first measurement, heat flow at discharge, q_d, can be estimated and writing,

$$q_d = \lambda_s \frac{T_d}{h_s} \tag{3.B.3}$$

yields T_d and therefore is the ΔT_r as recharge is assumed to occur at 0 °C.

Darcy's law can be modified and expressed as,

$$uh_b = \frac{\alpha g k \Delta T_r h_b (h_b + h_s)}{\nu L} \tag{3.B.4}$$

This expression enables estimating formation permeability, kh_b. Substituting the calculated values from equations (3.B.2) and (3.B.3), we can arrive at permeabilities, k, for h_b = 150 m and 550 m.

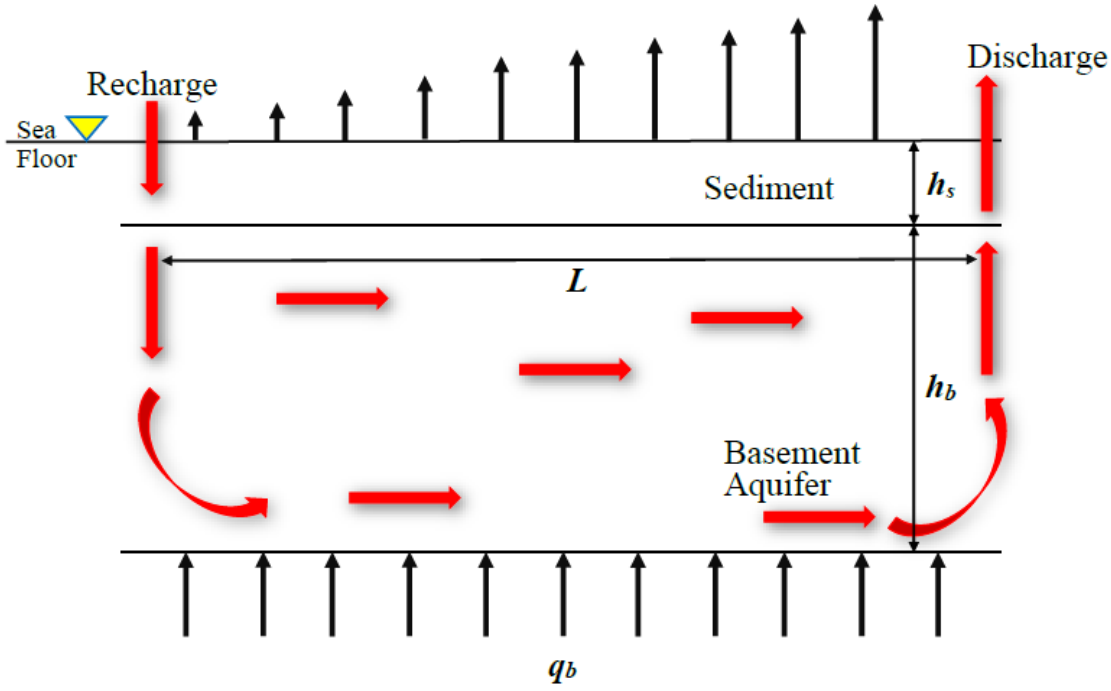

Figure 3.B1. A well-mixed aquifer flow model modified from Langseth and Herman, 1981. Refer to Table 3.2 for parameters shown in this figure.

Appendix 3.C: Heat flow near a fault

To consider how conductive heat flow changes near a fault, we follow the approach outlined in Lowell (1975) in which the fault was modeled as vertical plane of height h and a constant temperature T_{sp}, placed at $x = 0$. Then assuming the seafloor is a horizontal plane $z = 0$, maintained at temperature $T = 0$, the steady state temperature distribution in the rock adjacent to the fault can be found as outlined in Carslaw and Jaeger (1959). That is:

$$T(x,z) = \frac{T_{sp}}{\pi}\left[2\tan^{-1}\frac{z}{x} - \tan^{-1}\frac{z-h}{x} - \tan^{-1}\frac{z+h}{x}\right] \quad (3.C.1)$$

The conductive heat flux at the surface $z = 0$ is then:

$$q = \frac{2T_{sp}k_s}{\pi}\left[\frac{1}{x} - \frac{x}{x^2+h^2}\right] \quad (3.C.2)$$

If $x << h$, the second term in equation (3.C.2) may be neglected.

Appendix 3.D: Downflow and upflow of hydrothermal fluid in basement

Although all the heat transferred through the sediments at PB06 occurs by conduction, the significant differences between heat flow at basement lows and basement highs suggest that hydrothermal circulation redistributes heat within the basement rocks. At basement highs, conductive heat flow is much greater than the expected predicted value, while at basement lows, the heat flow is much less than that. We attribute these differences to downward fluid flow beneath the basement low, that reduces the conductive heat flow and upward flow beneath the basement high that increases the heat flow. For simplicity, we assume that downward flowing fluid and upward flowing fluid transports heat advectively at the estimated basement temperature ΔT_s. Thus to calculate the respective vertical flow rates u_z we write

$$q_b - q_{obs} = \rho_f c_f u_z \Delta T_s \quad (3.D.1)$$

where a negative value indicates upward flow and a positive value indicates downward flow.

Chapter 4

Analysis of Thermal Profiles of Two Boreholes Drilled into Brothers Volcano During IODP Expedition 376

Kannikha Parameswari Kolandaivelu[1], Cecile Massiot[2], Agnes Reyes[2], Robert Lowell[1]

[1]Department of Geosciences, Virginia Polytechnic Institute and State University, Blacksburg, VA 24061
[2]GNS Science, 1 Fairway Drive, Lower Hutt 5040, New Zealand

In preparation to be submitted in 2019

Abstract

Temperature measurements obtained from two boreholes drilled in the Brothers Volcano during the International Ocean Discovery Program's (IODP) Expedition 376 revealed both recharge and discharge regimes. The ~ 450 m deep Hole U1530A drilled in the area where high temperature black smoker vent fields are present in the northwest caldera wall showed a temperature profile suggestive of a recharge regime. The profile also suggests the exit of downwelling fluids through a permeable layer at the bottom of the hole that is at least 40 m thick. A borehole downflow model for this hole estimated a flow rate of 107.8 m/hr and yielded permeabilities between ~ 6 x 10^{-13} m^2 and 2 x 10^{-14} m^2 for a pressure differential of ~ 20 kPa to 800kPa. Hole U1528D is a ~ 360 m deep hole in a diffuse venting regime whose thermal profile is indicative of discharge. A flowrate of 14.4 m/hr is derived using a borehole upflow model. Assuming that the discharge profile reflects that of the formation itself, the profile shape reflects that of a large convective hydrothermal cell. Scale analysis yields a flow rate of ~1.2 x 10^{-8} m/s within the formation and a permeability of ~10^{-13} m^2.

4.1. Introduction

One-third of the Earth's submarine volcanism is manifested along the ~ 22,000 long intraoceanic arcs with 93% occurring in the Pacific Ocean (see Figure 4.1) [*de Ronde et. al.*, 2003]. The estimated number of hydrothermal sites per 70-100 km of arc indicates that the frequency of hydrothermal activity in these arcs exceeds that at mid-ocean ridges [*de Ronde et. al.*, 2002; 2017]. However, the characteristics of hydrothermal circulation at volcanic arcs has limited number of studies compared to those at mid-ocean ridges. Moreover, most studies are carried out in a two-dimensional fashion where physical and chemical measurements are made on the ocean floor. These measurements have then been used to infer processes occurring at depth. To directly sample or measure the hydrothermal processes occurring at depth (i.e. third dimension), deep sea drilling is necessary.

The Kermadec segment of the Kermadec-Tonga intraoceanic volcanic arc, located northeast of New Zealand, has about 33 large volcanoes of which 80% are hydrothermally active [*de Ronde et. al.*, 2002]. Brothers Volcano, part of the Kermadec Arc, hosts a group of vigorously active, complex hydrothermal systems that largely arise due to geologic variations, structural constraints, regional temperature variations, bathymetric changes etc., [*de Ronde et. al.*, 2005; 2011]. This volcano has been the site of numerous studies due to its unique geological setting, structural constraints, vent fluid chemistry, microbial communities and biological ecosystems [*Wright & Gamble*, 1999; *Delteil et. al.*, 2002; *de Ronde et. al.*, 2005; 2011; *Stott et. al.*, 2008; *Takai et. al.*, 2009; *Caratori Tontini et al.*, 2012]. Hence, Integrated Ocean Drilling Program's (IODP) expedition 376 to the Brothers Volcano focused on obtaining an integrated suite of measurements in the vertical dimension by drilling into Brothers Volcano. One of the objectives of this expedition, which is also the focus of this paper, is to enhance the understanding of the sub-seafloor thermal structure in this volcano and to determine fluid flow characteristics and permeability architecture in the upper crust.

4.2. Geologic Setting

Brothers Volcano is one of three caldera-containing volcanoes and it has some of the highest hydrothermal activity in the Kermadec Arc [*de Ronde et. al.*, 2002]. It is a predominantly silicic volcanic complex that is oval in shape and measures approximately 13 km long and 8 km wide. The continuous caldera rim sits at 1540 meters below sea level (mbsl) and the caldera floor sits at 1850 mbsl surrounded by 290-530 m high walls. A northeast-southwest elongated post-collapse 350 m high resurgent cone, known as Upper Cone, sits within the caldera with a smaller Lower Cone attached to its northeast flank (Figure 4.2).

Five sites were drilled as part of the IODP's expedition 376, two in the northwestern portions of the caldera rim and walls, one in the western portion of the caldera floor, one in the center of the upper cone and one in the center of the lower cone. In this paper, we will discuss the borehole temperature measurements obtained from the drill site U1530A in the northwest (NW) caldera wall and the drill site U1528D in upper cone (UC) as these were the only sites where downhole logging measurements were performed (Figure 4.2). These two sites represent the two main hydrothermal system types explored during the expedition. The first one is the seawater dominated system in the NW caldera wall and rim, where ~ 300 °C high temperature black smoker vent fields occur. The second one is the magmatic volatile dominated system in the UC where diffuse venting sites with temperatures of ~ 60 °C are observed. Drilling into these sites of

contrasting hydrothermal activities provide the field-observations for fluid flow rate and permeability modeling.

4.3. Operations

4.3.1. U1530A – NW Caldera

The 453.1 m deep Hole U1530A is located in the NW caldera wall at 34°51.6588'S, 179°3.4572'E in a water depth of 1594.9 mbsl. The drill string was kept at a logging depth of 67.1 meters below sea floor (mbsf) and the Triple Combination, known as Triple Combo, logging tool string was lowered into the open hole 7.6 hours after drilling had stopped and 4.7 hours after fluid circulation ceased (Figure 4.3a). Triple Combo measures natural gamma ray, porosity, density, magnetic susceptibility, resistivity, caliper, and logging head temperature. Four passes at a logging speed of 9.1 m/min were made in total (two downhole and two uphole) with this Triple Combo suite. The first downhole pass was terminated at 447 mbsf due to infill at the bottom of the hole. The uphole pass ("Repeat pass") was acquired to 273 mbsf, and was followed by a second downhole log to record temperature. The second uphole pass was measured to seafloor (so is termed the "Main pass"). For this study, the first downhole pass and the main pass are utilized. The first logging run with the Triple Combo logging took 4.7 hours in total. After this, the FMS-Sonic combo string that produces resistivity images, measures compressive, shear and Stoneley wave velocities, spectral gamma ray, and temperature was lowered to 417 mbsf into the open hole 14.9 hours after drilling had ceased and 12 hours since fluid circulation stopped. Four passes at a logging speed of 9.1 m/min were made in total (two downhole and two uphole) with the FMS-Sonic combo. The first uphole is named the "repeat" pass, and the longer second uphole is termed the "main" pass. The second downhole pass was run without recording any data. The first downhole pass and the main pass will be utilized in this study. This second logging operation took 5.76 hours.

4.3.2. U1528D – Upper Cone

The 359.3 m deep Hole U1528D is situated at 34°52.9219'S, 179°4.1164'E in the limited, flat central area of the pit crater, in a water depth of 1228.1 mbsl. The drill string was maintained at a logging depth of 50.3 mbsf and the High Temperature Triple Combo (HTTC) tool string was run in the open hole in wireline mode, with live surface readout, 64.7 hours after drilling had stopped and 3.8 hours after the last cold-water (seawater and freshwater) circulation (Figure 4.3b). The HTTC recorded bulk density and photoelectric factor, spectral and total count natural gamma ray, and fluid temperature. Three passes, one downhole and two uphole (first uphole termed as "repeat" pass, second uphole termed as "main" pass), were made in total at a logging speed of 10 m/min. All three passes were terminated at a depth of 332 mbsf due to a bridge in the hole at that depth. This study utilizes the first downhole pass and main pass. The logging operation took 4.55 hours in total.

4.4. Temperature Data, Analysis and Interpretation

4.4.1. U1530A – NW Caldera

The temperature logs obtained from the first Triple Combo logging run measured 5 °C at the seafloor and increased steadily downhole to about 94 °C at 447 mbsf after ~ 5 hours of stopping circulation (Figure 4.4). 2.65 hours after the first run, the second FMS Sonic logging run was carried out and measured temperatures of 5-6 °C at the seafloor which increased steadily downhole to 40.9 °C at 447 mbsf during the first downhole pass. After 1.28 hours, the temperature at 447 mbsf had cooled down from 40.9 to 37.6 °C during the main pass (Figure 4.4). Overall the temperatures at 447 mbsf cooled down from 94 °C to 37.6 °C in 8.75 hours indicating the rate of cooling as 6.45 °C/hour. The temperature profiles demonstrating a gradual increase in temperature with depth also displayed a 'concave up' shape suggestive of recharge into the borehole [*Taniguchi et. al.*, 1999; *Fisher et. al.*, 2003; *Anderson*, 2005]. The profiles also show several small positive and negative thermal anomalies (see inset of Figure 4.4) [as described by e.g. *Drury & Jessop*, 1982]. Such anomalies are often interpreted to be related to fluids flowing into and out of the borehole and aid in the identification of possible fluid flow zones, and more permeable lithologies [*Serra*, 1984; *Ziagos & Blackwell*, 1986; *Anderson*, 2005; *Baujard et. al.*, 2017]. For example one such anomaly is observed between 255 and 295 mbsf (see inset of Figure 4.4), especially in the very first (i.e., least disturbances in borehole fluids) Triple Combo downhole temperature profile indicating a permeable flow zone. However, given that these temperature anomalies are only of ~1 °C in magnitude, the flow rates in this zone are considered small [*Drury*, 1984; *Ge*, 1998].

The shape of the temperature profile as a whole indicates the recharge nature of the borehole and the temperature profile can be used to estimate the flow rate down the borehole. The infiltration of seawater in this borehole cools the borehole from a maximum of 94 °C to 37.6 °C in 8.75 hours. Downflow of water via a newly drilled borehole serves as an indication of underpressured crust with respect to the hydrostatic [*Becker et. al.*, 1983]. The thermal profile shows no obvious indication of distinct high permeability fluid flow zones/reservoirs in the upper 400 m of the borehole and portrays a steady "concave up" profile. An isothermal profile from 400 to 440 mbsf, however, could signify a region of downflowing fluid loss from the borehole having a minimum thickness of 40 m. Assuming that the main pass from second logging run reflects a steady state formation thermal profile, a steady-state, simple heat-exchange model for downflowing fluids [*Jaeger*, 1942; 1961; *Becker et. al.*, 1983] through the borehole can be employed to estimate flow rates and determine formation permeability. The model uses a simple heat balance wherein the loss of heat due to recharge is balanced by radial heat conduction from the surrounding formation into the open borehole walls. The heat balance is expressed as [following *Jaeger*, 1961; *Becker et. al.*, 1983],

$$\pi a^2 \nu (\rho c)_{sw} \frac{dT(z,a)}{dz} + 2\pi a f(z,a) = 0 \qquad (4.1)$$

where a is borehole radius, ν is fluid velocity , $(\rho c)_{sw}$ is the density and specific heat of seawater, $\frac{dT(z,a)}{dz}$ is the vertical temperature gradient within the borehole, and $f(z,a)$ is a radial heat flow function [*Jaeger*, 1961]. *Jaeger* [1961] also provides the radial heat flow through the borehole walls as,

$$f(z,a) = \frac{4K_e \Delta T(z)}{\pi^2 a} I(\tau) \quad (4.2)$$

Here K_e is thermal conductivity from shipboard measurements, $\Delta T(z) = T(z,\infty) - T(z,a)$ where $T(z,\infty)$ is the undisturbed temperature far from the borehole and $T(z,a)$ is the temperature of the water in the borehole. A few tens to hundreds meters away from this borehole, several ~ 300 °C high-temperature vent are observed [*deRonde et. al.*, 2011]. Hence, we assume that the undisturbed temperature far from the borehole is 300 °C. $I(\tau)$ is the integral $I(0, I; x)$ defined as $I(\tau) = \int_0^\infty \frac{e^{-\tau u^2} du}{u[J_0^2(u) + Y_0^2(u)]}$ from *Jaeger and Clarke* [1942] and dimensionless time, $\tau = \frac{\chi t}{a^2}$ where $\chi = \frac{K_e}{(\rho c)_{sw}}$ is thermal diffusivity. Substituting equation (4.2) in equation (4.1) for the values for different variables given in Table 4.1., a downflow fluid velocity of ~108 m/hr is obtained.

Using the estimate of fluid flow within the borehole, an estimate of bulk permeability can be obtained using a steady-state analysis. This permeability estimate is carried out under the assumptions that the aquifer is homogeneous, isotropic horizontally oriented porous medium; with Darcian, radial flow within the fractured formation and 100% well efficiency. Based on the fluid velocities from equation (4.1), and assuming that the downwelling fluid is lost through the 40-m thick zone from 400-440 mbsf, the total fluid flow [*Matthews and Russel*, 1967, *Becker et. al.*, 1983],

$$Q = \pi a^2 v = \frac{8kH\Delta P}{\pi\mu} I(\tau) \quad (4.3)$$

where k is bulk permeability, H is the 40 m permeable zone thickness, μ is the dynamic viscosity and ΔP is the difference between hydrostatic and initial formation pressure. Because there are no direct measurement of ΔP, it is assumed for a range from 20 kPa [*Fisher et. al.*, 1997; *Davis et. al.*, 1997] to 800 kPa [*Becker et.al.*, 1983]. Using the estimated downhole flow rates and values for different parameters from Table 4.1., equation (4.3) yields a bulk permeability value of ~ 6 x 10^{-13} m^2 to 2 x 10^{-14} m^2.

4.4.2. U1528D – Upper Cone

The temperature log from the downhole pass measured 12.5 °C at the seafloor (greater than ambient seafloor temperature) and 202.3 °C at 332 mbsf (bottom of hole). This was procured 4.35 hours after circulation ceased. The main pass measured 16.8 °C (greater than ambient seafloor temperature) at the seafloor and 231.3 °C at bottom of hole 6.5 hours after the circulation ceased. Both temperature profiles exhibit highly similar shapes but are separated due to the differences in temperatures and times in the two logs (Figure 4.5). Temperatures in the main pass are generally higher than the downhole pass indicating that the hole was still heating up in the 2.5 hours between passes. Three distinct isothermal segments separated by small positive and negative thermal anomalies are observed in the logs: 1) 11 - 93 mbsf 2) 105 – 145 mbsf 3) 168 - 235 mbsf. The near isothermal profiles indicate strong upflow in the borehole [*Becker et. al.*, 1984]. The three distinct isothermal zones above 235 mbsf exhibit a temperature profile typical for a flowing well during or after drilling [*Steingrimsson*, 2013] where there are three feed zones at the end of each isothermal segment feeding hot fluids into the borehole.

However, the magnitude of the anomalies are very small, and they may result from drilling disturbances that could very well disappear as the borehole reaches equilibrium. Below 235 mbsf, temperature decreases from 137 °C to 122.6 °C at 270 mbsf (downhole pass) and from 145 °C to 134 °C at 270 mbsf (main pass) creating a zone of low temperature anomaly. This anomaly could be due to the slow conductive rebound occurring as a cooling effect due to recent drilling [*Fisher et. al.*, 1997; *Steingrimsson*, 2013]. Since this anomaly occurs right after the third feed zone, warm fluids did not flow from greater depths. Below 270 mbsf, temperature increases rapidly to 202.3 °C (downhole) and 231.3 °C (main) at the bottom of hole suggesting a rapid rebound in temperatures to reflect that of the formation due to minimal drilling disturbances at this depth (Figure 4.5). In the upper 10 m of the borehole, the temperature profiles takes the shape of a thermal boundary layer, which in this case is caused by the influx of seawater into the hole and the resultant mixing and cooling of the upper layers of upwelling hot fluids. Two different end member interpretations can be made of the temperature profiles. The first one treats the thermal profile as that which was induced by the drilling of the borehole and reflects the borehole regime. The second one assumes that the thermal profile reflects that of the formation.

4.4.2.1. Thermal Profile due to Borehole Effect

The nearly isothermal temperature profile from 11 mbsf to 235 mbsf is indicative of advective heat transport up the borehole and hence the steady-state model for upwelling fluids in the borehole can be employed to estimate the flow rate of the upwelling fluids. A simple heat balance can be written wherein the advection of heat up the borehole is balanced by radial heat conduction through the open borehole walls into the surrounding formation and can be expressed as [following *Jaeger*, 1961; *Fisher et. al.*, 1997],

$$\pi a^2 \nu (\rho c)_{sw} \frac{dT(z,a)}{dz} - 2\pi a f(z,a) = 0 . \qquad (4.4)$$

Here a is borehole radius, ν is fluid velocity, $(\rho c)_{sw}$ is the density and specific heat of seawater, $\frac{dT(z,a)}{dz}$ is the vertical temperature gradient within the borehole, and $f(z,a)$ is a radial heat flow function [*Jaeger*, 1961] as given in equation (4.2). In equation (4.2) $T(z,\infty)$ is defined as the undisturbed temperature far from the borehole where the temperature increases linearly with depth. Hence $T(z,\infty) = gz$ where g is the geothermal gradient dT/dz. Using the depth to magma chamber as 2.5 km [*deRonde et. al.*, 2011] and temperature at the top of magma chamber as 1000 °C, g= (1000-60)°C/2500 m = 0.4 °C/m. The 60 °C is at the seafloor obtained from the downhole measurements and also from previous diffuse flow measurements at the Upper Cone [*deRonde et. al.*, 2011]. Substituting the radial heat flow function calculated from equation (4.2), and values for different variables given in Table 4.1., into equation (4.4), upflow fluid velocities of ~14.4 m/hr are arrived.

4.4.2.2. Formation Thermal Regime

Assuming that the main pass thermal profile in the borehole reflects that of the formation prior to drilling, its shape can be observed to have two distinct boundary layers at the top (10 m) and bottom (50 m) of the borehole connected by a nearly isothermal profile (250 m) in the middle which reflects that of a large convective fluid circulation cell. The heat flux at the bottom is given by,

$$q = K_e \frac{dT}{dz} \tag{4.5}$$

where *dT*= 230-130 °C over the bottom boundary layer of 50 m. This results in a heat flux of 5 W/m^2, which can be considered as a fixed heat flux at the bottom of the borehole. This heat flux is then equated with upward advective heat flux within the isothermal region of the borehole without any loss to the surroundings, wherein the isothermal region is treated as a homogeneous porous medium. Then advective heat flux, q_{adv} is given by,

$$q_{adv} = \rho_f c_f v \Delta T \tag{4.6}$$

and yields a fluid velocity of ~1.2 x 10^{-8} m/s. Permeability estimates can be obtained from scale analysis where the upflow is assumed to be driven by the temperature difference, *ΔT*, between the bottom of the borehole and the far field temperature at that depth. Upflow velocity is given by,

$$v = \frac{\alpha g k \Delta T}{\gamma} \tag{4.7}$$

where α is thermal expansion coefficient of water, *g* is acceleration due to gravity, *k* is formation permeability and γ is kinematic viscosity of fluid. Substituting the values for parameters given in Table 4.1., permeability of ~ 10^{-13} m^2 is arrived.

4.5. Discussion

4.5.1. U1530A – NW Caldera

A steady-state borehole downflow model was used to estimate fluid flow rates and formation permeabilities in Hole U1530A at the NW caldera as the thermal profile exhibited a "concave up" recharge type profile. A downhole flow rate was estimated as ~ 108 m/hr and the permeabilities ranged from ~ 6 x 10^{-13} m^2 to 2 x 10^{-14} m^2 for pressure differential of 20 kPa to 800 kPa between the underpressured basement fluids and hydrostatic. This downflow rate is higher than the 88 m/hr estimated in Hole 504B based on temperature logs obtained during DSDP leg 70 and is four times higher than 23 m/hr estimated from DSDP Leg 83 measurements. Leg 83 measurements were done 23 months after DSDP leg 70 measurements and hence reflects a true borehole equilibrium profile [*Becker et. al.*, 1983]. Given the observation that downflow into the borehole is rapidly cooling it, the calculated downflow rate is consistent with continued borehole cooling. Based on the flow rate obtained for Hole U1530A, and assuming that the downhole flow was not driven by thermal buoyancy but instead forced by the pressure difference between the hydrostatic and the underpressured basement pore fluids, permeabilities of ~ 6 x 10^{-13} m^2 to 2 x 10^{-14} m^2 for an assumed range of pressure differences were obtained. This estimated permeability is similar to the estimate of 10^{-14} m^2 from Hole 504B [*Becker et. al.*, 1983] and with 10^{-14} m^2 employed for numerical simulations of Brothers Volcano [*Gruen et. al.*, 2014]. Prior to drilling, heat in Hole U1530A could likely have been primarily transported conductively. The initial bottom of hole measurement of 94 °C at 447 mbsf cooled down to 37.6 °C in ten hours indicating that the rapid ingress of cold seawater was due to the underpressured reservoir. This is a clear indication that the downflow rate obtained from the steady state model is a transient value. Since the temperature profile shows a uniform concave upward shape with no isothermal sections until ~ 400 mbsf, the formation does not have distinct horizontal permeable reservoirs

for fluid flow. The 40 m thick permeable reservoir identified by isothermal thermal profile in that interval, does not represent the entire thickness of the flow zone. The flow zone could very well extend to greater depths. From equation (4.3), the flow rate is proportional to the product *kH* and hence the greater the permeable zone thickness, the smaller the estimate of *k*. Though the flow rates and permeabilities obtained from the steady state model gives a first order insight into the borehole regime, the transient nature of the borehole needs detailed assessment taking an approach that includes the transient heat flow in the borehole [*Becker et. al.*, 1983; *Fisher et. al.*, 1997].

The U1530A borehole is in close proximity to the high temperature vent fields in the north west caldera wall. The lowest temperature recorded at the bottom of the hole at ~ 450 mbsf was 37.6 °C and it is surrounded by 300 °C black smoker type vent fields at ~ 20 m to 250 m away [Figure 4.6]. This could be due to induced recharge close to hydrothermal vent sites [*Coumou et.al.*, 2008]. Formation of shells of mineral precipitates, particularly anhydrite, around the high temperature vents induced heat transfer due to convection in the formation wherein the recharge of cold seawater occurs in close proximity to vents [Kolandaivelu, 2015]. This vertical wall of anhydrite brings forth a quasi-uniform temperature around it redistributing the isotherms in a manner where the low temperature isotherm (recharge) is positioned in close proximity to a thin hot water zone [Figure 4.7] [Cheng & Minkowycz, 1977]. Further investigations based on Nusselt number approximations and transient variations in isotherm distributions are needed to quantify this phenomenon further.

4.5.2. U1528D – Upper Cone

Temperature profile at Hole U1528D in the Upper Cone of the Brothers Volcano could be indicative of a discharging borehole with three permeable feed zones along the walls of the borehole feeding warm fluids into the borehole. There could very well be other zones of permeable fluid pathways that contribute to the overall formation permeability. Based on the steady state borehole upflow model, flow rates of ~ 14.4 m/hr were deduced. Assuming that the thermal profile reflects that of the formation, permeability assessment based on boundary layer heat flow scale analysis yielded ~ 10^{-13} m^2. The permeability value based on the scale analysis is the same as the value of 10^{-13} m^2 considered while numerically modeling the cone site [*Gruen et. al.*, 2014]. The upwelling of fluids in the borehole could be induced by drilling because of the overpressure of heated pore fluids with respect to the hydrostatic and also presence of dynamic hydrothermal circulation systems within the basement [*Fisher et al.*, 1990; 1994; 1997; *Davis et al.*, 1997]. The isothermal nature of the logs followed by a low cold temperature anomaly suggests that slow conductive rebound was occurring right beneath the isothermal zones which is indicative of the warm upwelling borehole fluids not sourced from reservoirs at deeper depths. The flow rate and permeability estimates were based on a steady state scenario in the borehole. The steady state models might give an overestimate of the results and hence the values obtained from this model should be considered as upper bounds. Transient models estimate time averaged values and hence are closer to a true representation than a constant flow rate model.

The steady state borehole upflow model might not be appropriate as the small thermal anomalies could be the effects induced by the introduction of the borehole. Neglecting these minor effects, the thermal profile reflects that of the formation where a large scale convection cell is present. Hence the scale analysis model reflecting the formation thermal regime is considered appropriate for this borehole.

4.5.3. General Discussion

Further work on using transient models in both holes U1530A and U1528D should yield a realistic estimate of flow rates and permeabilities, which could be corroborated with estimates from ongoing studies that are using different scientific methods. The temperature profiles that resulted from the Expedition 376 is the first of its kind where the temperature regime with respect to depth has been measured in an active submarine arc volcanic setting. Preliminary analysis of the temperature profiles at Holes U1530A and U1528D demonstrate the complex nature of the distribution of hydrothermal circulation systems and their evolution in the Brothers Volcano. The profiles also portray the complexities in thermal regimes in such arc volcanoes and provide a brief insight into its dynamic nature.

4.6. Conclusion

The temperature data from the two boreholes discussed in this work suggest two different hydrothermal regimes in a seafloor volcanic environment: 1) Recharge regime at U1530A which is in the area where high temperature black smoker vent fields are present 2) Discharge regime at U1528D where diffuse venting is observed. Although these profiles are transient in nature, using a steady state analysis provides the values of flow rates and permeabilities which can set a first order approximation and can be compared to future estimates from detailed investigations by other scientific methods. Further studies on correlating the temperature profiles, its interpretations and preliminary analysis with other downhole logs, physical properties, structural geology, fluid inclusion studies and microbiology are underway. The integration of these multiple datasets will provide a window into the third dimension of arc volcanoes that may be applied to other volcano-hydrothermal systems on both land and on the seafloor.

Acknowledgments. The authors thank the crew, IODP technical team and science party of the IODP Expedition 376 for the enormous success of the expedition despite the unique challenges and setbacks faced everyday. The authors also thank the downhole logging team of engineers from Schlumberger for successfully logging the hole despite the hostile conditions at the Brothers Volcano. This work stemmed from the US Science Support Program's salary support to KPK to sail as a Petrophysics/Geothermal Borehole Logging Specialist in the IODP's Expedition 376 to the Brothers Volcano.

4.7. References

Baujard, C., Genter, A., Dalmais, E., Maurer, V., Hehn, R., Rosillette, R., ... & Schmittbuhl, J. (2017). Hydrothermal characterization of wells GRT-1 and GRT-2 in Rittershoffen, France: Implications on the understanding of natural flow systems in the rhine graben. Geothermics, 65, 255-268.

Beaulieu, S. E., Baker, E. T., German, C. R., & Maffei, A. (2013). An authoritative global database for active submarine hydrothermal vent fields. Geochemistry, Geophysics, Geosystems, 14(11), 4892-4905.

Becker, K., Langseth, M. G., Von Herzen, R. P., & Anderson, R. N. (1983). Deep crustal geothermal measurements, hole 504B, Costa Rica Rift. Journal of Geophysical Research: Solid Earth, 88(B4), 3447-3457.

Caratori Tontini, F., Davy, B., de Ronde, C.E.J., Embley, R.W., Leybourne, M., and Tivey, M.A., 2012a. Crustal magnetization of Brothers Volcano, New Zealand, measured by autonomous underwater vehicles: geophysical expression of a submarine hydrothermal system. Economic Geology, 107(8):1571–1581.

Cheng, P., & Minkowycz, W. J. (1977). Free convection about a vertical flat plate embedded in a porous medium with application to heat transfer from a dike. Journal of Geophysical Research, 82(14), 2040-2044.

Coumou, D., Driesner, T., & Heinrich, C. A. (2008). The structure and dynamics of mid-ocean ridge hydrothermal systems. Science, 321(5897), 1825-1828.

Davis, E.E., A.T. Fisher, J. Firth, et al., Proceedings of the Ocean Drilling Program, Init. Repts. 168, Ocean Drilling Program, College Station, TX, in press, 1997.

Delteil, J., Ruellan, E., Wright, I., and Matsumoto, T., 2002. Structure and structural development of the Havre Trough (SW Pacific). Journal of Geophysical Research: Solid Earth, 107(B7):1–17.

de Ronde, C.E.J., Massoth, G.J., Baker, E.T., and Lupton, J.E., 2003. Submarine hydrothermal venting related to volcanic arcs. In Simmons, S.F., and Graham, I.G. (Eds.), *Volcanic, Geothermal, and Ore-Forming Fluids: Rulers and Witnesses of Processes Within the Earth.* Society of Economic Geologists - Special Publication. 10:91–109.

de Ronde, C.E.J., Humphris, S.E., and Höfig, T.W., 2017. *Expedition 376 Scientific Prospectus: Brothers Arc Flux.* International Ocean Discovery Program.

de Ronde, C.E.J., Hannington, M.D., Stoffers, P., Wright, I.C., Ditchburn, R.G., Reyes, A.G., Baker, E.T., Massoth, G.J., Lupton, J.E., Walker, S.L., Greene, R.R., Soong, C.W.R., Ishibashi, J., Lebon, G.T., Bray, C.J., and Resing, J.A., 2005. Evolution of a submarine magmatic-hydrothermal system: BrothersVolcano, southern Kermadec arc, New Zealand. Ecoomic Geology, 100(6):1097–1133.

de Ronde, C.E.J., Massoth, G.J., Butterfield, D.A., Christenson, B.W., Ishibashi, J., Ditchburn, R.G., Hannington, M.D., Brathwaite, R.L., Lupton, J.E., Kamenetsky, V.S., Graham, I.J., Zellmer, G.F., Dziak, R.P., Embley, R.W., Dekov, V.M., Munnik, F., Lahr, J., Evans, L.J., and Takai, K., 2011. Submarine hydrothermal activity and gold-rich mineralization at Brothers Volcano, Kermadec arc, New Zealand. Mineralium Deposita, 46(5–6):541–584.

Drury, M. J., & Jessop, A. M. (1982). The effect of a fluid-filled fracture on the temperature profile in a borehole. Geothermics, 11(3), 145-152.

Drury, M. J. (1984). Borehole temperature logging for the detection of water flow. Geoexploration, 22(3-4), 231-243.

Fisher, A. T., Becker, K., & Davis, E. E. (1997). The permeability of young oceanic crust east of Juan de Fuca Ridge determined using borehole thermal measurements. Geophysical Research Letters, 24(11), 1311-1314.

Ge, S. (1998). Estimation of groundwater velocity in localized fracture zones from well temperature profiles. Journal of Volcanology and Geothermal Research, 84(1-2), 93-101.

Gruen, G., Weis, P., Driesner, T., Heinrich, C. A., & de Ronde, C. E. (2014). Hydrodynamic modeling of magmatic–hydrothermal activity at submarine arc volcanoes, with implications for ore formation. Earth and Planetary Science Letters, 404, 307-318.

Jaeger, J. C. (1961). The effect of the drilling fluid on temperatures measured in bore holes. Journal of Geophysical Research, 66(2), 563-569.

Kolandaivelu, K. P. (2015). Numerical Modeling of the Hydrothermal System at East Pacific Rise (EPR) 9 Degrees 50'N Including Anhydrite Precipitation (Doctoral dissertation, Virginia Tech).

Matthews, C. S., and Russell, D. G., 1967. Pressure build-up and flow tests in wells. Soc. Petrol. Eng. Monogr., 1.

Steingrimsson, B. (2013). Geothermal well logging: Temperature and pressure logs. Tutorial-Geothermal Training Programme.

Stott, M.B., Saito, J.A., Crowe, M.A., Dunfield, P.F., Hou, S., Nakasone, E., Daughney, C.J., Smirnova, A.V., Mountain, B.W., Takai, K., and Alam, M., 2008. Culture-independent characterization of a novel microbial community at a hydrothermal vent at Brothers Volcano, Kermadec arc, New Zealand. Journal of Geophysical Research: Solid Earth, 113(B8):B08S06.

Takai, K., Nunoura, T., Horikoshi, K., Shibuya, T., Nakamura, K., Suzuki, Y., Stott, M., Massoth, G.J., Christenson, B.W., de Ronde, C.E.J., Butterfield, D.A., Ishibashi, J., Lupton, J.E., and Evans, L.J., 2009. Variability in microbial communities in black smoker chimneys at the NW caldera vent field, Brothers Volcano, Kermadec arc. Geomicrobiology Journal, 26(8):552–569.

Wright, I.C., and Gamble, J.A., 1999. Southern Kermadec submarine caldera arc volcanoes (SW Pacific): caldera formation by effusive and pyroclastic eruption. Marine Geology, 161(2–4):207–227.

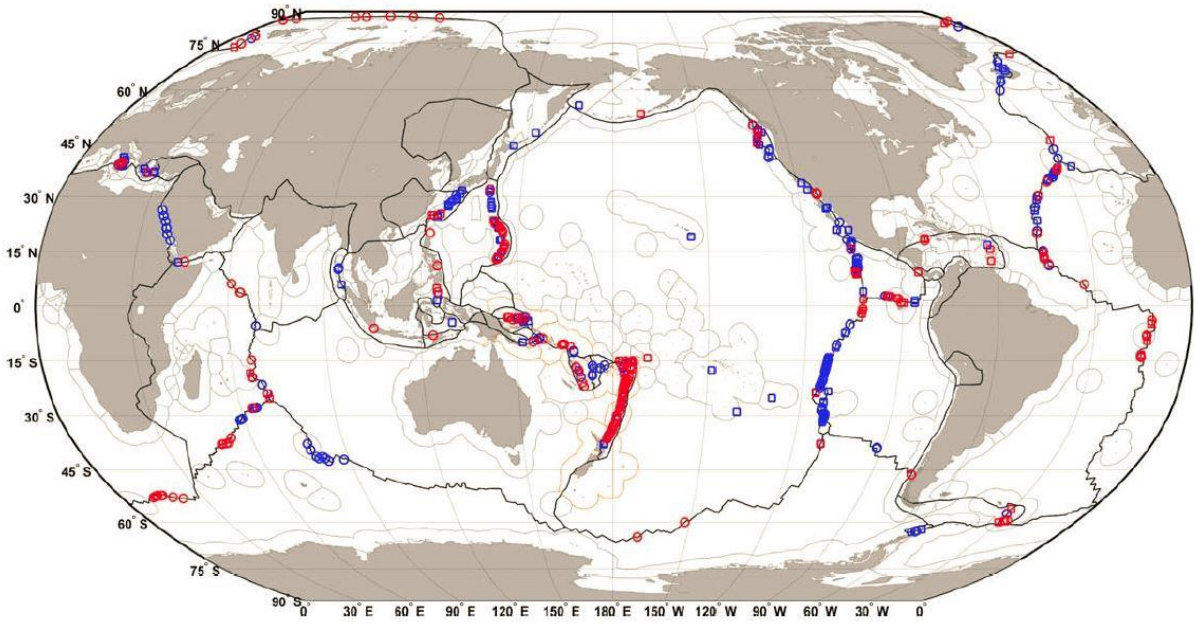

Figure 4.1. Active vent field locations: Confirmed (square); inferred (circle); discovered prior to 2000 (blue); discovered after 2000 (red). Plate boundaries are shown in black lines. [from *Beaulieu et. al.*, 2013].

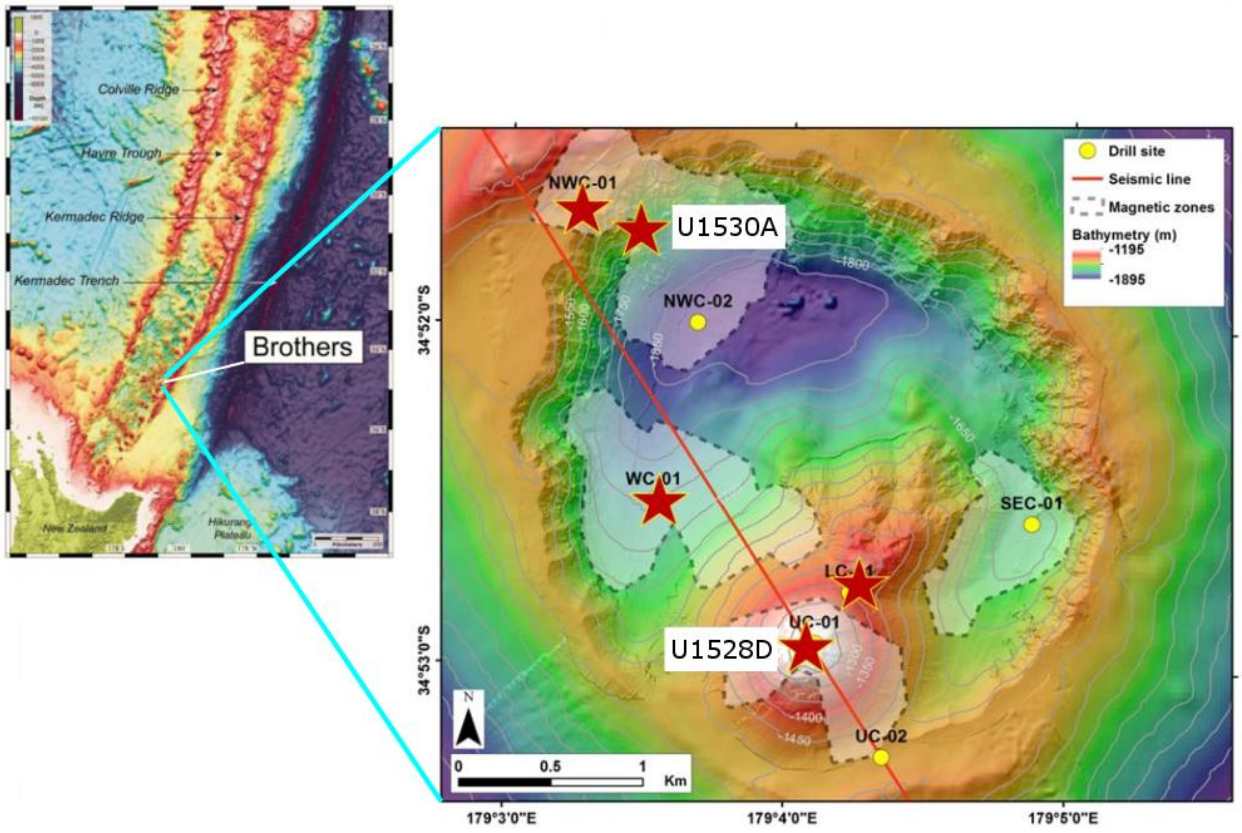

Figure 4.2. [modified from *deRonde et. al.*, 2017] Left figure: Bathymetric map of the Kermadec arc and trench. Brothers Volcano is labelled along with other tectonic elements in the arc [*deRonde et. al.,* 2017]. Right figure: Bathymetric map of the Brothers Volcano with five drilled sites marked by red stars and the two sites discusses in this paper are labelled. Transparent zones marked by dotted lines show the magnetic lows signifying hydrothermal upflow zones drawn after *Caratori Tontini et al.*, 2012.

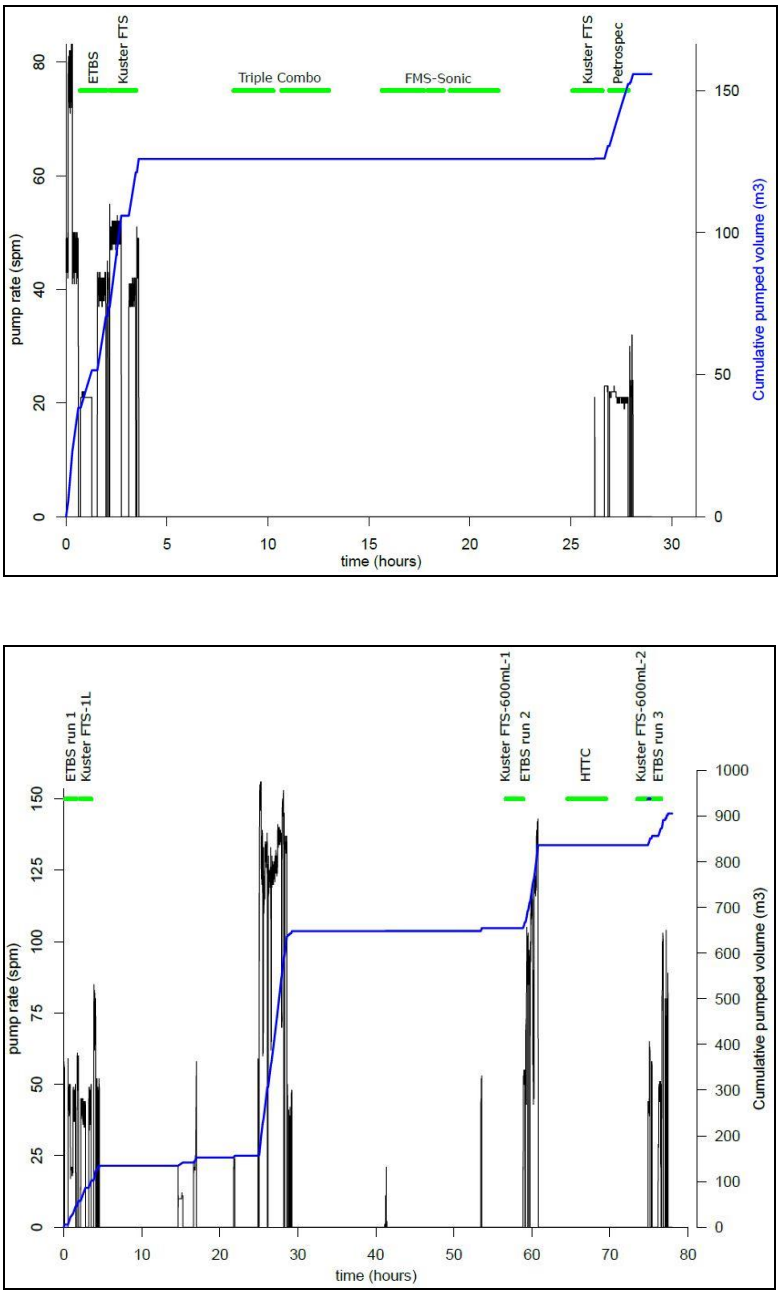

Figure 4.3. Pump rate (black line) in strokes per minute (spm) and Cumulative pumped volume (blue line) in cubic meters as a function of time after drilling in hours for a) Hole U1530A – North West Caldera b) Hole U1528D – Upper Cone.

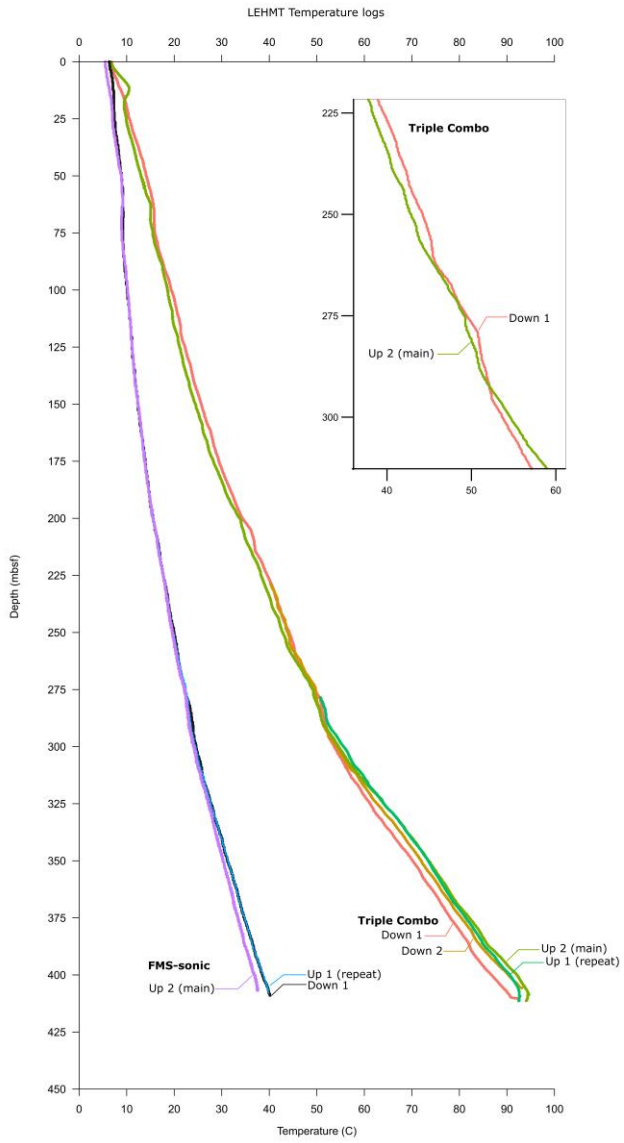

Figure 4.4. Temperature in °C with depth in meters below sea floor (mbsf) for Hole U1530A – North West caldera for two different runs – Triple Combo run and FMS Sonic run. Both the runs are spaced 8.75 hours apart. The inset figure shows the thermal anomalies present at the depth of 250-300 mbsf.

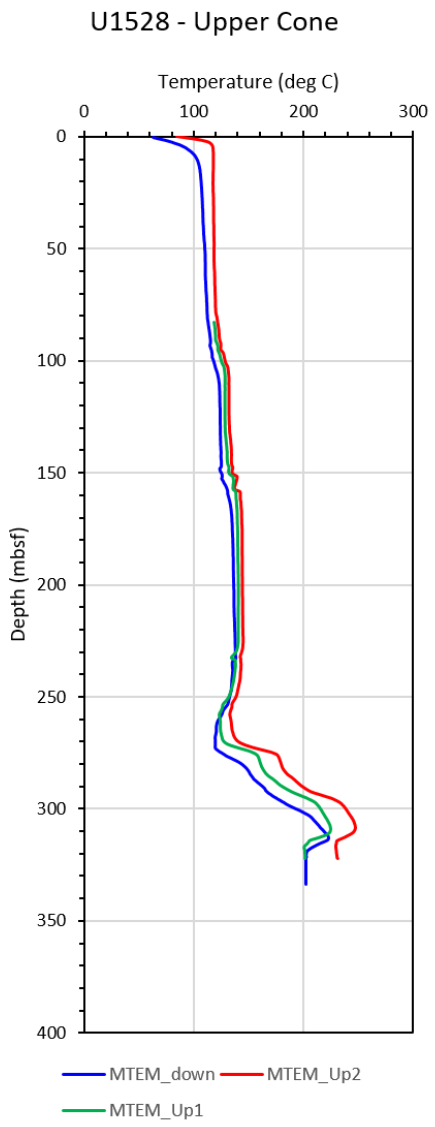

Figure 4.5. Temperature in °C with depth in meters below sea floor (mbsf) for Hole U1528D – Upper Cone for the HTTC run.

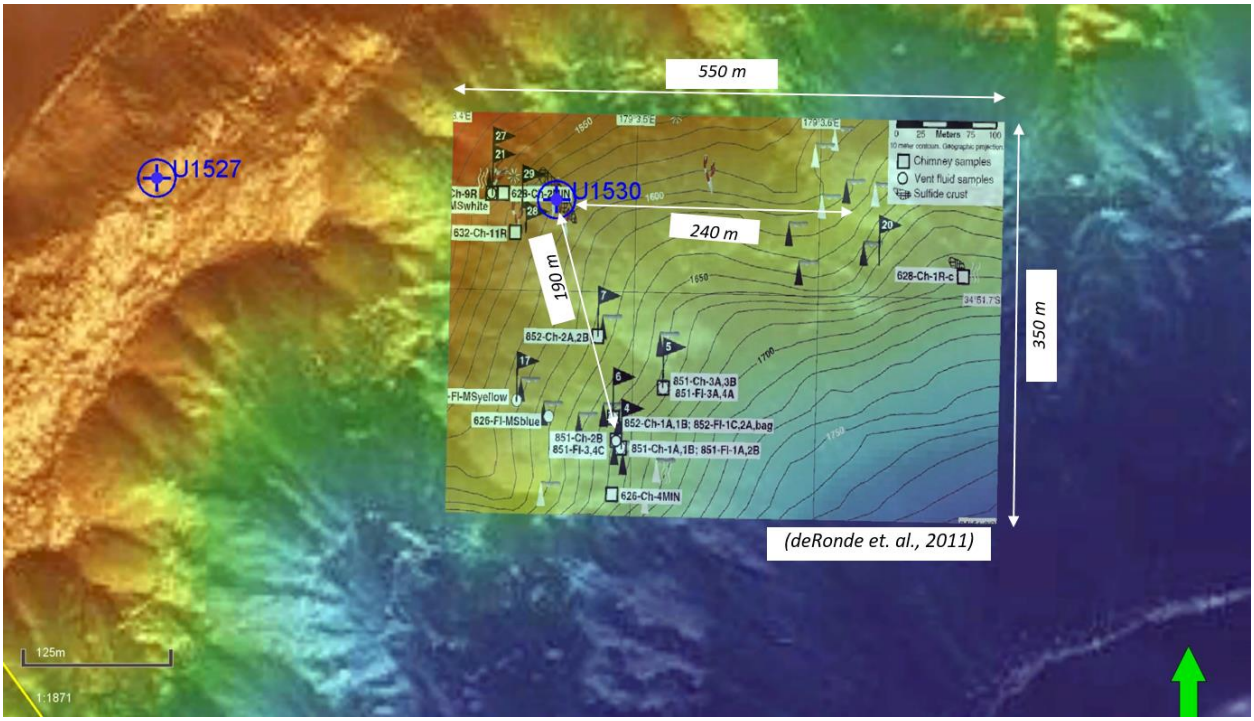

Figure 4.6. Bathymetry of the north west caldera wall near the drill holes U1527 and U1530A. The superimposed figure from *deRonde et al.*, 2011 shows the vent fields surrounding U1530A along with their distances from the borehole. The green arrow shows the North direction.

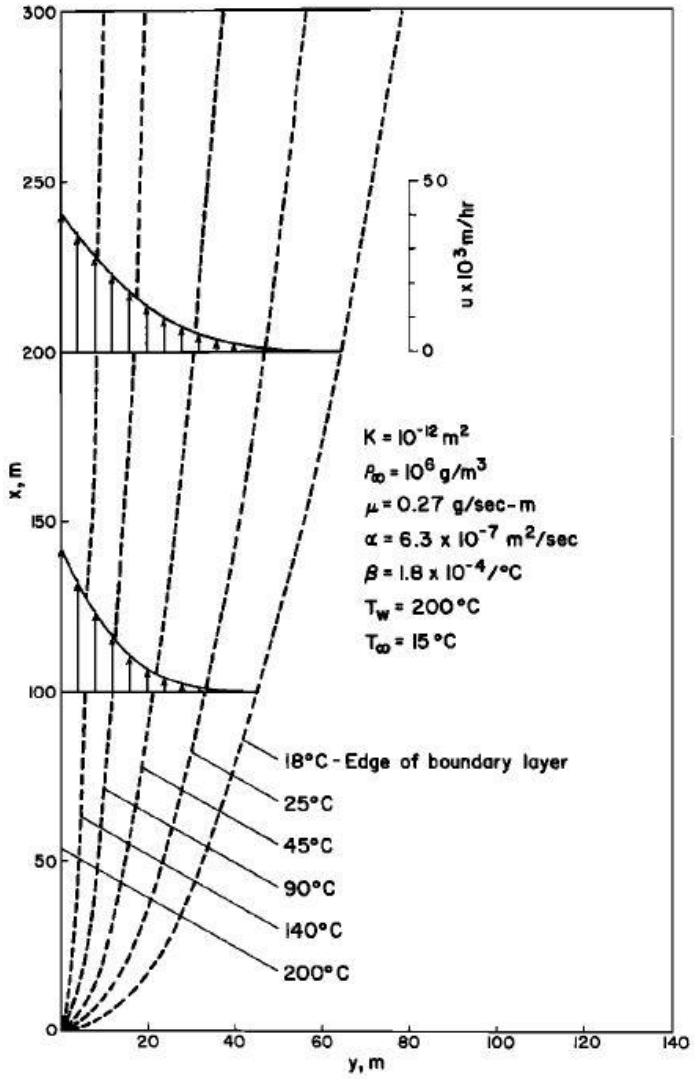

Figure 4.7. [from *Cheng & Minkowycz,* 1977] Distribution of isotherms (dotted lines) and velocity distribution (solid lines) for a dike with uniform wall temperature.

Table 4.1. Parameters and Values

Symbol	Definition	Value	Units
a	Borehole radius	0.4 (U1530A) 0.3 (U1528D)	m
c_{sw}	Specific heat of seawater	4200	J kg^{-1} K^{-1}
g	Acceleration due to gravity	9.81	m s^{-2}
k	Effective bulk permeability		m^2
q	Basal heat flux		Wm^{-2}
H	Thickness of the permeable zone		m
$I(\tau)$	Integral $I(0, I; x)$ [Jaeger & Clarke, 1942]	5.340 (U1530A) 3.3633 (U1528D)	$Wm^{-1}K^{-1}$
K_e	Thermal conductivity from shipboard measurements	3.5 (U1530A) 2.46 (U1528D)	$Wm^{-1}K^{-1}$
Q	Mass flux through the borehole wall		
α	Thermal expansion coefficient of water	10^{-4}	$°C^{-1}$
γ	Kinematic viscosity of the fluid	10^{-6}	m^2 s^{-1}
μ	Dynamic viscosity of the fluid	0.4 x 10^{-3}	kg m^{-1} s^{-1}
v	Fluid velocity		m/s or m/hr
ρ_{sw}	Density of seawater	1000	kg m^{-3}
τ	Dimensionless time	0.1405 (U1530A) 0.7 (U1528D)	m yr^{-1}
χ	Thermal diffusivity of fluid	5.87 x 10^{-7}	m^2 s^{-1}

Chapter 5

Future Work

The volumetric flow rates calculated in the first manuscript show that lateral heat advection may be important heat transfer mechanism in fracture zones. Surprisingly, heat is advected from the younger to older plate, Given that the permeability of the Ecuador Fracture Zone is similar to that of typical oceanic crust it may be that advective heat transfer may be an important process in fracture zone which has received little attention to date. Additional heat flow studies in inactive fracture zones are needed to assess the general importance of this mechanism. Acquisition of more heat flow data along collocated with other geological and geophysical data would make a significant contribution to the understanding of the role of fluid flow and advective heat transport in oceanic fracture zones.

The heat and fluid fluxes for different oceanic crustal ages obtained in the second manuscript will be incorporated in oceanographic models to infer the influence of geothermal heating on the abyssal ocean circulation in the Panama Basin. Currently, where represented in numerical models, geothermal heat flux into the ocean is treated as purely conductive. Incorporating the advective heat loss estimates into the oceanographic numerical models will increase the sensitivity of geothermally forced circulation and provide a closer to realistic scenario of deep ocean circulation in the Panama Basin. As geothermal heating has been shown to affect deep ocean circulation globally [refs], the inclusion of advective heat transfer and mass fluxes from lithosphere should be incorporated into future studies.

The borehole temperature logs discussed in the third manuscript, show that the thermal regime is not in steady state in the short times following drilling and fluid circulation. Hence, transient models of flow rate changes estimated from the temperature logs of the recharge and discharge borehole will be performed. A thermal model of large scale and regional scale heat distribution in and around Brothers Volcano will be constructed based on the temperature logs and previously collected heat flow data from the Brothers Volcano. This will enhance the understanding of fluid flow patterns and their pathways in intra oceanic volcano systems, and their resulting permeability distribution and the mechanisms that govern their evolution.